Particle-in-Cell Simulations of Perpendicular Supernova Shock Fronts

DISSERTATION

zur Erlangung des akademischen Grades
Doktor der Naturwissenschaften
(Dr. rer. nat.)
in der Wissenschaftsdisziplin Theoretische Astroteilchenphysik

eingereicht an der
Mathematisch-Naturwissenschaftlichen Fakultät
der Universität Potsdam

von

VOLKMAR WIELAND

Potsdam, den 16. März 2015

“When you have eliminated the impossible,
whatever remains, however improbable,
must be the truth.”

Sherlock Holmes

Contents

Chapter 1

Introduction

For centuries mankind observed the sky with all possible means of collecting the light reaching Earth from the vast depth of the Universe, not knowing there was something else. For only one century we know that the Universe is also swarmed with highly energetic particles - the so-called cosmic rays. For just a few decades we also know that they are not just an astronomical phenomenon, but have also an impact here on Earth by causing phenomena like aurorae and lightnings.

The relatively young research field of astroparticle physics, which stands at the crossroad of astrophysics and particle physics, has brought forth many fascinating insights about cosmic rays. Yet, one mystery still remains: What is the origin of cosmic rays?[1]. For one hundred years, scientists from all over the world working in experimental and theoretical research fields are combining their efforts to solve this great mystery and trace back these particular messengers from the Universe.

1.1 A Brief History of Cosmic Rays

The first hint on the existence of particle radiation coming from space was found by the Austrian-American physicist Victor Francis Hess in 1912. Prior to his experiments, scientists had the assumption that the level of ionising radiation would decrease with increasing altitude, since the distance to the source of the radiation in Earth's lithosphere would increase. However, early measurements in the atmosphere revealed higher levels of ionising radiation than expected. Undertaking several balloon flights, Hess measured the ionisation rate in different altitudes and found a significant increase with rising altitude. His logical conclusion was that some radiation of great power must be entering Earth's atmosphere from above[2].

The American experimental physicist Robert A. Millikan coined the term "cosmic rays" for this radiation in the 1920s, believing that it consisted largely out of gamma rays, i.e., photons with very high energy. However, some years later it was found that the intensity of the cosmic ray flux was varying with latitude, indicating that they are deflected by Earth's magnetic field and, therefore, must be charged particles. Subsequent experiments led to the conclusion that the primary cosmic rays are mostly protons, with a small amount of Helium nuclei and a minor fraction of heavier nuclei[3].

In the 1930s, the French physicist Pierre Victor Auger undertook experiments with several separated ground-based detectors which detected many near-simultaneous discharges. This lead to the conclusion that highly energetic primary cosmic-ray particles interact with nuclei in Earth's atmosphere, thereby creating a cascade of secondary particles leading to an extensive shower of electrons, muons and photons at ground level[4].

---

[1] Ginzburg/Syrovatsky, Progress of Theoretical Physics Supplement 20 [1961].

[2] Hess, Physikalische Zeitschrift 13 [1912].

[3] Freier et al., Physical Review 74 [1948]

[4] Auger et al., Reviews of Modern Physics 11 [1939]

Since the 1950s, many different experiments all over the world and even in space were carried out, are still running or are planned for the future to measure the energy spectrum of the cosmic rays with increasing accuracy. Today, our knowledge about the cosmic ray spectrum spans over 12 decades of energy, reaching from $\approx 10^9\,\text{eV}$ up to $\approx 10^{21}\,\text{eV}$ ($1\,\text{eV} \approx 1.602 \times 10^{-19}\,\text{J}$), and over 32 orders of magnitude in flux density, reaching from one particle per square metre per second at 1 GeV down to one particle per square metre per year at 1 PeV and even one particle per square kilometre per year at 1 EeV.

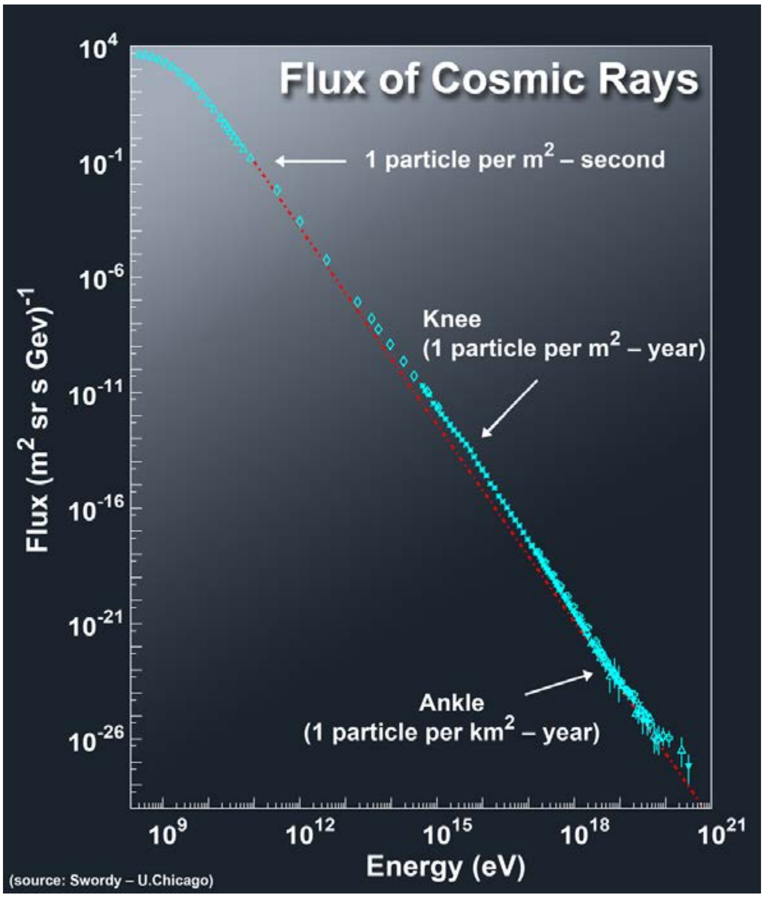

(source: Swordy – U.Chicago)

Figure 1.1: The energy spectrum of cosmic rays is the fingerprint of the cosmic rays which we can detect here on Earth.[5]

The spectrum is nearly featureless and it can be described by a so-called power law, i.e., $N(E) \propto E^{-\gamma}$, where N is the particle flux at a certain particle energy E and γ is the spectral index. The value of the spectral index varies marginally with the energy. It has the value $\gamma = 2.7$ for energies below $4 \times 10^{15}\,\text{eV}$, then the spectrum “softens” with a value of $\gamma = 3.1$ up to $4 \times 10^{18}\,\text{eV}$, whereafter it “hardens” again with a value of $\gamma \approx 2.7$. Due to the similarity the shape of the cosmic-ray spectrum has to a human leg, the two breaks in the spectrum are called “knee” and “ankle”, respectively[6].

Above $4 \times 10^{19}\,\text{eV}$, the spectrum is cut off due to the Greisen–Zatsepin–Kuzmin limit[7,8]. Particles above this energy interact with photons of the cosmic microwave background, thereby creating a Δ resonance which decays into a proton and π^0 or into a neutron and a π^+. This limit prevents high energy cosmic-ray particles from travelling more then $\approx$ 160 million light-years ($1\,\text{light-year} \approx 9.4607 \times 10^{15}\,\text{m}$).

---

[5] Astrid Chantelauze, HAP, *Cosmic ray spectrum.*

[6] Hörandel, Progress in Particle and Nuclear Physics 64 [2010].

[7] Greisen, Physical Review Letters 16 [1966].

[8] Zatsepin/Kuz’min, Soviet Journal of Experimental and Theoretical Physics Letters 4 [1966].

1.2 The Origin of Cosmic Rays - A Cosmic Detective Story

Gathering the Clues

Multiple methods have been devised to detect cosmic rays. Basically, they can be divided into two different approaches. Cosmic rays can be detected indirectly by using Cherenkov telescopes to observe the Cherenkov radiation emitted by particles flying faster than the local speed of light through Earth's atmosphere or water. The other approach is to detect cosmic rays directly by using scintillators, cloud chambers or bubble chambers. Using these methods, we are able to measure the composition and the spectrum of the cosmic rays.

However, what we can measure is merely the fingerprint the cosmic rays leave when they hit Earth. Although cosmic rays provide an exciting new way of looking at the Universe, there is a major disadvantage compared to light. Since they are charged particles, they are deflected by the interstellar magnetic field due to the Lorentz force, whereas the neutral photons can pass through it on a straight line. Only cosmic-ray particles at the highest energies are fast enough to have a large enough gyroradius to get only marginally deflected.

For photons it is almost always easy to pinpoint the source where they come from. For the majority of the cosmic-ray particles, however, we cannot say more *a priori* than that we detect them coming isotropically from all over the sky. The path of a charged particle through the interstellar magnetic field is determined by the laws of diffusion. Since this is a purely stochastic process, the particles in question could still have come from anywhere. What adds another difficulty to the case is the fact that we do not know precisely the strength and the distribution of the interstellar magnetic field, since almost no *in situ* measurement are available[9]. Fortunately, one thing we know is that the speed - and, therefore, the energy - of the charged particle cannot be altered by the Lorentz force. Therefore, it is reasonable to presume that the particle energy we observe on Earth is the same as the energy with which the particle was emitted in the first place. What is now left to us, is to find the sources that are capable of accelerating particles to such high energies.

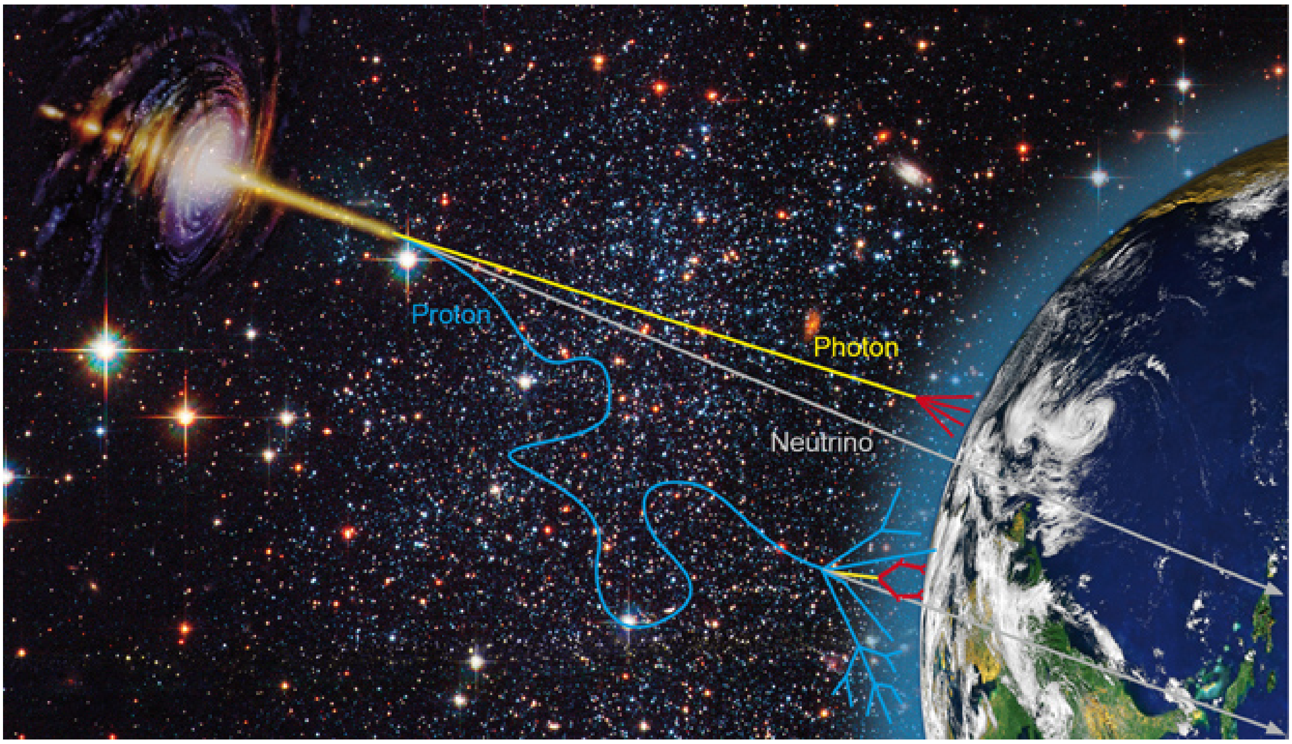

Figure 1.2: What is the origin of cosmic rays? The interstellar magnetic field makes it hard to answer this question, because it alters the trajectory of charged particles. This is where our cosmic detective story begins.[10]

---

[9] Gurnett et al., Science 341 [2013]

[10] DESY, *Astroparticle physics research explores the universe with high energy neutrinos and gamma rays.*

Examining the Suspects

When it comes down to identifying the main suspects, the crucial criterion is the gyroradius r_g of the accelerated particles. A charged particle with charge q and mass m moving at a velocity $\boldsymbol{v}$ in a magnetic field $\boldsymbol{B}$ undergoes a gyrating motion due to the Lorentz force $\boldsymbol{F}_L = q\,\boldsymbol{v} \times \mathbf{B}$. The acting counter-force in this process is the centripetal force $\boldsymbol{F}_c = mv^2/r_g$. Equating both forces and considering only particle motion perpendicular to a homogeneous magnetic field, yields the equation for the gyroradius:

$$r_g = \frac{mv_\perp}{|q|B}. \tag{1.1}$$

A possible source for high-energy cosmic rays can only accelerate particles up to the point where the diameter of the particle's circular orbit, $2r_g$, becomes larger than the size of the source L. Beyond this point, the particle will be able to escape the source. This constraint, namely $2r_g < L$, leads us to a condition under which a source would be able to contain the particles it accelerated up to an energy E:

$$BL > \frac{2E}{|q|c}, \tag{1.2}$$

where c is the speed of light and the definition of the relativistic momentum $p \approx E/c$ was used instead of the classical momentum mv in equation (1.1), since we are dealing with highly relativistic particles. This condition is called the Hillas criterion[11]. It can be illustrated graphically by the Hillas diagram as shown in Figure 1.3.

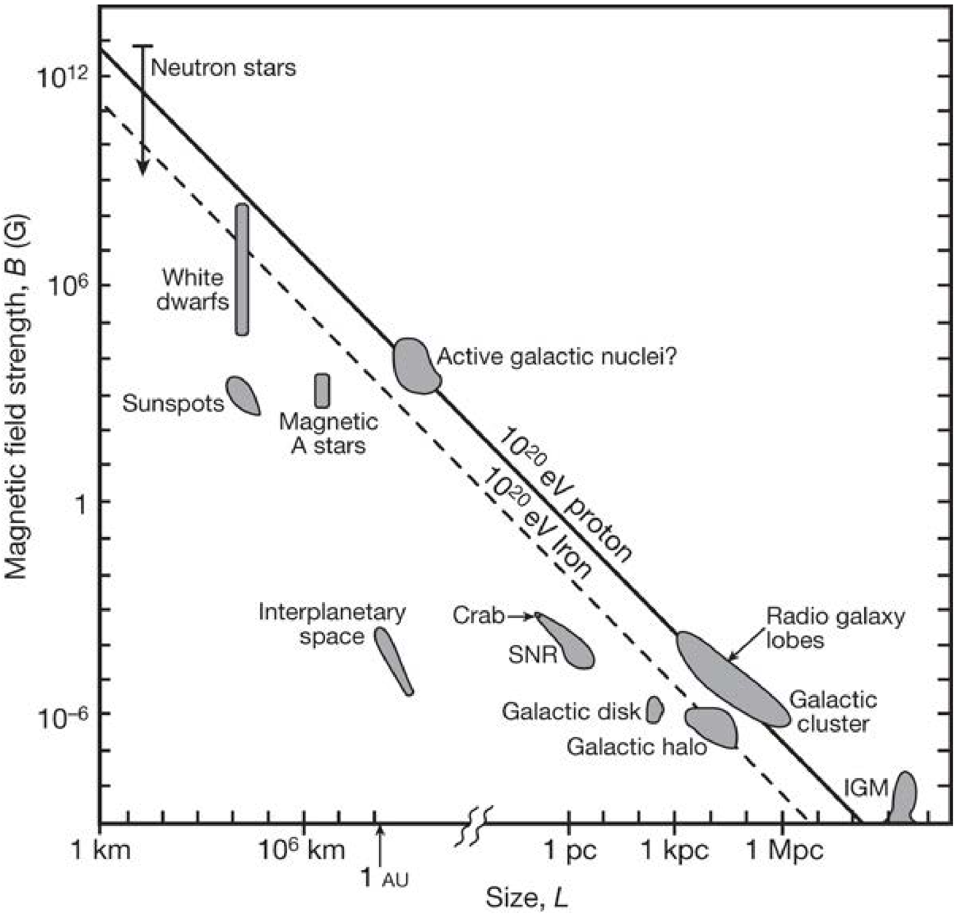

Figure 1.3: The Hillas diagram captures all known possible sources for cosmic rays. The theoretical upper limits of the particle energy are determined by the size of and the magnetic field strength inside the celestial objects. Here, upper-right means higher energy.[12]

---

[11] Hillas, Annual Review of Astronomy and Astrophysics 22 [1984].

[12] Pablo M. Bauleo and Julio Rodriguez Martino, *Hillas Diagram.*

Figure 1.3 most impressively shows to how much more nature is capable compared to humanity, if we consider the largest human made particle accelerator, currently the Large Hadron Collider (LHC). Compared to most of the celestial objects, it is able to produce very strong magnetic fields at around 10^5 G ($1\,\mathrm{G} = 10^{-4}\,\mathrm{T}$). On the other hand, its size of 27 km looks minuscule next to nearly all displayed celestial objects. The maximum energy to which it is able to accelerate particles lies at around 10^{12} eV, which is approximately the maximum energy a particle can get in interplanetary space.

Particles with energies below $\approx 10^9$ eV most likely originate from the Sun in form of solar wind and solar flares. These particles are deflected by Earth's magnetic field and enter the atmosphere in the polar regions where they create the beautiful aurorae.

For particle energies up to $\approx 10^{18}$ eV, most of the probable sources can be accounted for in our own galaxy such as neutron stars, white dwarfs or the galactic halo. The structures called "knee" and "ankle" in Figure 1.1 are the two remarkable features of the cosmic-ray spectrum lying within this energy range. While the origin of the former is still under debate[13], the latter clearly marks the point where cosmic-ray particles can no longer be contained within our galaxy[14], because their gyro radius would exceed the extension of our galaxy.

For particles with energies beyond $\approx 10^{18}$ eV, only sources outside the Milky Way come into consideration. Only the most extreme environments of the Universe are capable of accelerating particles to such high energies. Among them are active galactic nuclei (AGNs), radio galaxies lobes and galactic clusters.

Although cosmic rays are detected isotropically over the sky, which makes it difficult to pinpoint their sources, many of the above mentioned objects were successfully confirmed to be producing high-energy cosmic rays due to the by-products they fortunately emit. Gamma rays and neutrinos cannot be deflected by a magnetic field and, therefore, are able to reach Earth on a straight line, as shown in Figure 1.2. Indeed, high-energy gamma rays[15] and neutrinos[16] have been observed from several objects and could clearly reveal them as probable sources of cosmic rays.

---

[13] Apel et al., Physical Review Letters 107 [2011].

[14] Apel et al., Physical Review D 87 [2013].

[15] The Pierre Auger Collaboration, Science 318 [2007].

[16] Aartsen et al., Physical Review Letters 111 [2013]

Pinning Down the Culprit

One particular galactic source shall be of special interest to us. For several decades, they have been under suspicion to be responsible for the majority of galactic cosmic rays. They are also considered to be among the most extreme objects of the Universe. However, they are so rare that only a few eyes have seen them. The objects under consideration here are supernovae or merely their remains, the so-called supernova remnants.

Based on observations made in other galaxies similar to ours, it was estimated that about three supernovae should go off in the Milky Way every century. However, the 20th century was surprisingly devoid of such events. The youngest supernova remnant in our galaxy, which can be seen in Figure 1.4, bears the somewhat unromantic designation SNR G1.9+0.3 and is likely to be about 100 years old[17]. Thus, no man alive has ever seen a supernova in our galaxy with his own eyes.

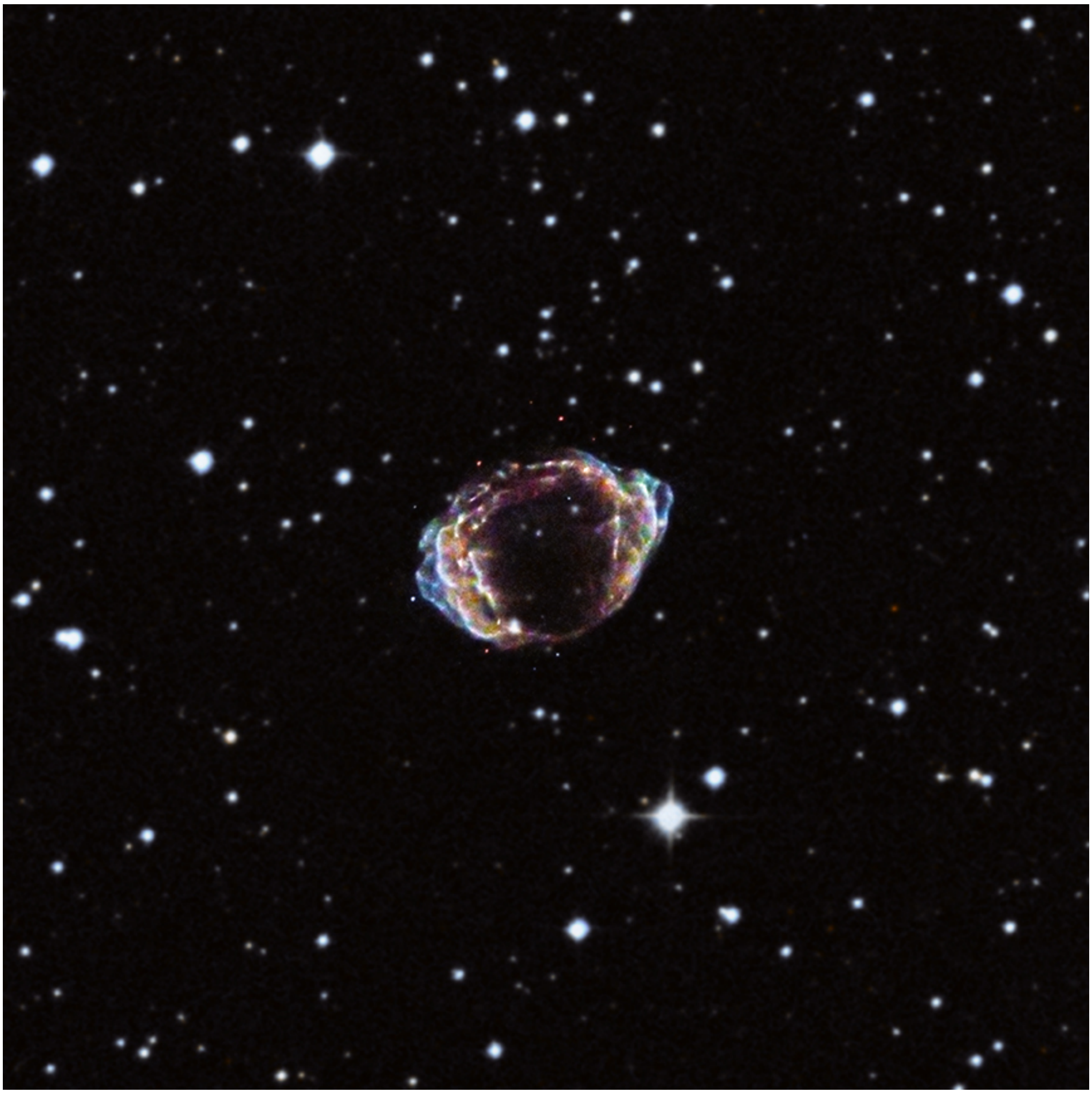

Figure 1.4: This is a composite image of the supernova remnant G1.9+0.3. Shown here are X-ray data (red, green, blue) and optical data (white, cyan).[18]

---

[17] Reynolds et al., The Astrophysical Journal Letters 680 [2008]

[18] X-ray: NASA/CXC/NCSU/K.Borkowski et al.; Optical: DSS, *G1.9+0.3: The Remarkable Remains of a Recent Supernova.*

Nevertheless, we know that the total kinetic energy ejected in one supernova explosion is approximately 10^{63} eV[19]. This is more than sufficient to sustain the yearly rate of cosmic rays detected on Earth. The latter number can be estimated by considering that the local interstellar energy density of cosmic rays is about $1.8\,\mathrm{eV\,cm^{-3}}$ [20] filling the volume of the Milky Way with a diameter of ≈ 100000 light-years and a thickness of ≈ 1000 light-years. The time cosmic rays spend in our galaxy propagating from the source to Earth was estimated to be roughly 15×10^6 yr with measurements of radioactive isotopes within the population of cosmic-ray particles[21]. Putting those numbers together yields a rate of cosmic rays with an energy of $\approx 6.2 \times 10^{60}$ eV per year or one hundred times that number per century. Accordingly, even one supernova per century would be enough to sustain the number of galactic cosmic rays detected on Earth.

This is already a strong hint to support the assumption for supernovae being the main suspect. But we can add more to that. Looking at the Hillas diagram (Figure 1.3), we can figure out that supernova remnants (SNRs) are housing magnetic fields with a strength of more than 10^{-4} G and that they have a size of about 1 pc (1 pc $\approx 3.0857 \times 10^{16}$ m). Using the Hillas criterion in equation (1.2), we can estimate that supernova remnants are capable of containing accelerated particles up to an energy of up to 10^{18} eV. This is already the energy which is labelled "ankle" in Figure 1.1, i.e., the point where the presumed origin of cosmic rays turns from galactic to extragalactic.

Up to this point, we already have enough facts to assume that supernovae or supernova remnants, respectively, are capable of accelerating charged particles up to enormous energies. But is this enough to pin them down? Fortunately, by doing thorough investigations, NASA scientists were able to find the "smoking gun" in at least two cases which are shown below[22].

Figure 1.5: These two composite images show the supernova remnants W44 (*left*) and IC 443 (*right*) which were found to be accelerating cosmic-ray particles. Shown here are gamma-ray data (magenta), radio data (left: yellow), optical data (right: yellow) and infrared data (left: red; right: blue, cyan, green, red).[23]

These results are a major step forward in constructing a conclusive picture for this case. However, it remains to be seen if all supernova remnants are sources of cosmic rays. Nonetheless, now that we have found that they have the power to accelerate cosmic-ray particles, it remains to be investigated what are the means they use to do it. This very investigation is the focus of this dissertation.

---

[19] Smartt, Annual Review of Astronomy and Astrophysics 47 [2009].

[20] Webber, The Astrophysical Journal 506 [1998].

[21] Beringer et al., Physical Review D 86 [2012]

[22] Ackermann et al., Science 339 [2013]

[23] NASA/DOE/Fermi LAT Collaboration, NRAO/AUI, JPL-Caltech, ROSAT, *The W44 supernova remnant.* and NASA/DOE/Fermi LAT Collaboration, NOAO/AURA/NSF, JPL-Caltech/UCLA, *The UC 443 supernova remnant.*

1.3 Outlook

Before we start further investigations on the particle acceleration processes in supernova remnants, some basic information will be needed to better understand the object under consideration. Supernova remnants are the remains of one of the most powerful explosions in the Universe. As we know from our experience with explosions here on Earth, every such event causes a strong shock wave which propagates outward from the explosion site. It is only logical to presume that supernovae also cause shock waves and, indeed, there is strong observational evidence that this is the case. Therefore, the physics of shock waves, or simply shock physics, shall be the first point we turn our attention to in our investigation. Chapter 2 will give an overview of this fascinating subject, starting with an experimental outline in Section 2.1 and a brief theoretical description in Section 2.2. After that we will turn to the observational facts and theoretical models of supernova remnant shocks in Section 2.3 and the very mechanism presumed to be their means of accelerating cosmic-ray particles in Section 2.4.

Equipped with this background knowledge, we will turn our attention to the means by which I did my investigations. Since up to now it would be very hard to study supernova remnants on site, the only way we are left with to gain more knowledge about them is to model and simulate them with earthbound computers. For astrophysical plasmas like the object under consideration, the method known as Particle-in-Cell simulations has proven to be very efficient. Chapter 3 is dedicated solely to this subject. A quick glance at other methods in Section 3.1 will give a clue why Particle-in-Cell simulations were my method of choice. Following these remarks, I will explain the basic principles governing this method in Section 3.2. The dedicated simulation code I used, will be introduced in Section 3.3 along with its specifics and the technical studies I did with it prior to my investigations regarding the particle acceleration mechanism in supernova remnants.

Provided with all necessary tools we will start our investigation in Chapter 4, where we will take a closer look at the environment in a supernova remnant shock and see how we can manage to model it in Section 4.1. The particular environment I studied are the so-called perpendicular shocks. I will describe the new simulation setup for this environment in detail in Section 4.2 and the setup of the actual simulation in Section 4.3. The results I obtained with my simulation will follow in Section 4.4 and will be discussed and compared with results from earlier publications and with results by other groups in Section 4.5.

After all is said and done, I will conclude this thesis with some final remarks in Chapter 5.

Chapter 2

Shock Physics

SHOCKS are common phenomena in nature including our daily life. They also play an important role in astrophysics. The shocks of supernova remnants are considered the most promising candidate for the acceleration of particles up to very high energy[24]. Therefore, this chapter is devoted to the description of the physical processes happening in shocks, especially supernova remnant shocks, as far as we are able to understand them.

2.1 Shock Physics in a Nutshell

Whenever a fast flow encounters an obstacle which forces the flow to slow down sufficiently, the result of this is a shock[25]. The critical number for the occurrence of a shock is the famous sonic Mach number $M_s = v/c_s$, where v is the velocity of the obstacle relative to the bulk velocity of the flow and c_s is the speed of sound in the medium of the flow.

An obstacle moving through a medium always excites compression waves, which propagate through the medium at the speed of sound. If the velocity of the obstacle relative to the flow is subsonic, i.e., $M_s < 1$, the medium has sufficient time to rearrange itself and to dodge around the obstacle. If the velocity is supersonic, i.e., $M_s \geq 1$, the medium has no time to rearrange itself, but gets extremely compressed at the obstacle. This effect is called a shock or shock wave.

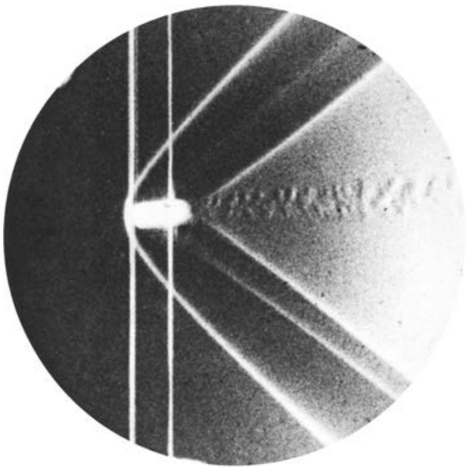

Figure 2.1: This first ever photo of a shock was taken by Ernst Mach in 1888 in Prague, using Schlieren Photography on a 5 mm-diameter negative. It depicts the waves around a supersonic brass bullet as well as the bow shock and trailing edge shock.[26]

---

[24] Ginzburg/Syrovatsky, Progress of Theoretical Physics Supplement 20 [1961].

[25] Treumann/Jaroschek, ARXIV [astro-ph] 0805.2132v1 [2008].

[26] Ernst Mach, *Photograph of a bullet in supersonic flight.*

Basic Shock Structure

The point of the shock wave that is farthest away from the obstacle is called the shock front. It is characterised by a sudden jump in several physical parameters. Most notable is a jump in the flow velocity, which abruptly drops from supersonic to subsonic. Accompanying this is a jump in the temperature, since the kinetic energy of the flow is converted into thermal energy. Yet another jump can be found in the density of the medium. As mentioned above, the medium gets extremely compressed at the shock front, and, although it can disperse again behind the shock, the density still is higher than in the unshocked medium. A shock process is an adiabatic compression and, since entropy is generated at the shock front, an irreversible process.

The surface at which the jumps occur is called shock discontinuity. It separates the unshocked medium in front of the shock from the shocked medium behind the shock, which are called upstream and downstream medium, respectively (see Figure 2.2). In some cases, it is also possible that two shock fronts develop: the forward shock, which is moving away from the site where the shock was created in forward direction and the reverse shock, which moves in the opposite direction and mostly back towards the site of the shock's creation (see Figure 2.3). Both shocks have their accompanying upstream and downstream region, in which the latter are separated by a so-called contact discontinuity, i.e., a surface across which there is no particle transport.

Figure 2.2: This is an illustration of a simple shock structure with the shock discontinuity separating the unshocked upstream medium (marked with index u) and the shocked downstream medium (marked with index d) drawn in a frame where the shock discontinuity is at rest.

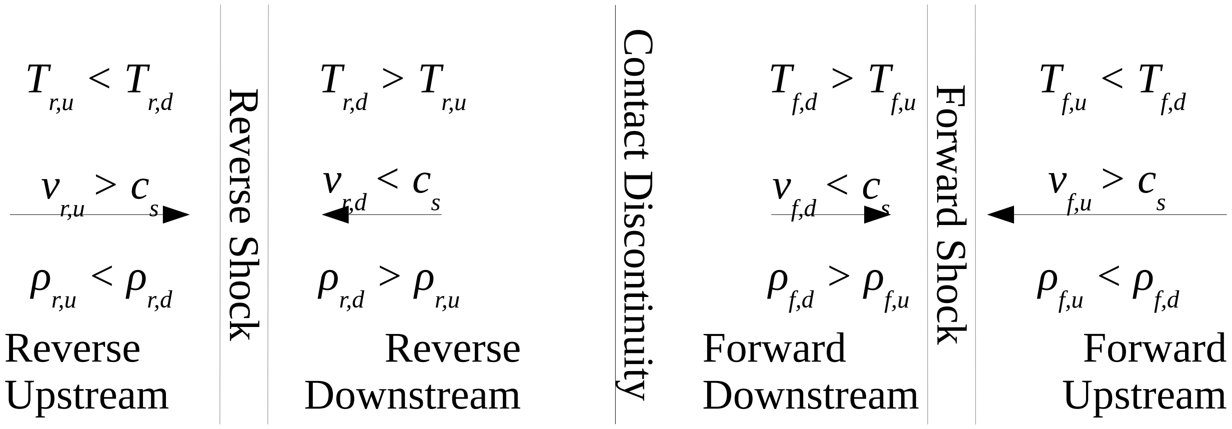

Figure 2.3: This is an illustration of a double-shock structure with forward shock moving away from the shock-creation site, reverse shock moving back towards the shock-creation site and the contact discontinuity separating the downstream regions of the forward and the reverse shock drawn in a frame where the contact discontinuity is at rest. The physical parameters of the upstream and downstream medium are marked with index u an index d, respectively.

Examples of Shocks

Well known examples for shocks can be found in our daily life. Every time one turns on a water tap, it is possible to witness the creation of a stationary termination shock inside the sink. When the water hits the bottom of the sink, it has to spread out sideways at a speed higher than the local surface-wave speed. At some point, the velocity abruptly drops to a speed below the local wave speed and the water forms a circular termination shock. This phenomenon is also called hydraulic jump[27].

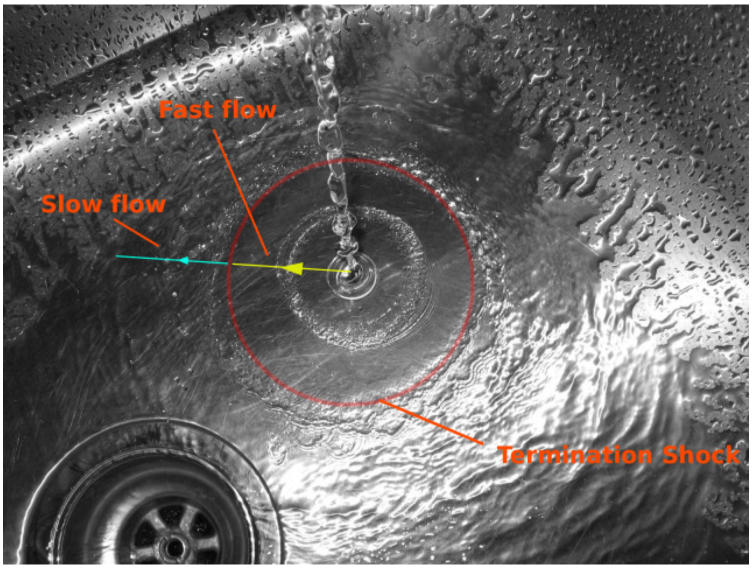

Figure 2.4: A circular termination shock can be created in a sink by turning on the water tub.[28]

Staying with the liquid element, it is possible to witness the creation of bow shocks in front of ships. If a ship is driving faster than the speed of surface waves, the water in front of the ship is no longer able to dodge around the hull, but is compressed into a massive bow wave. The faster the ship travels, the higher the bow wave gets.

Figure 2.5: The massive wave in front of a ship's bow was the eponym for the term "bow shock".[29]

---

[27] Douglas et al., Fluid Mechanics

[28] TiCPU, *A termination shock in a sink basin.*

[29] Enrique Muller, *USS Connecticut (BB-18) running speed trials off the Maine coast, 1906.*

The probably most popular example for shocks is the aerodynamic bow shock. For instance, if an aircraft flies faster than sound waves are able to propagate in air, the particles of the air in front of it are compressed. This bow shock is also audible in form of the sonic boom. Bow shocks were also the first shocks ever observed by Ernst Mach[30] (see Figure 2.1).

Figure 2.6: A supersonic aircraft compresses the air in front of it, which forms a bow shock.[31]

A double-shock structure quite similar to the one illustrated in Figure 2.3 can be found in the heliosphere. The particles of the solar wind are supersonic with respect to the interstellar medium. Since its pressure drops as it moves outward, at some point the solar wind is slowed down by interaction with the interstellar medium to subsonic speed and forms a termination shock. The interstellar medium is slowed down vice versa by interaction with the solar wind and creates a bow shock. At the heliopause, which takes the role of the contact discontinuity, the solar wind is completely stopped on its way outward and, on the other hand, the interstellar medium is stopped on its way inward[32].

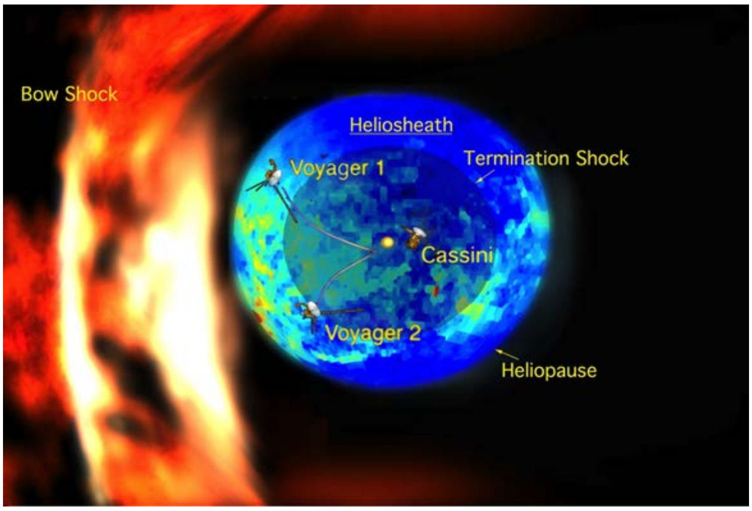

Figure 2.7: This computer model by NASA of the heliosphere shows all features of a double-shock structure.[33]

---

[30] Mach/Thiele, Arbeiten über Erscheinungen an fliegenden Projektilen.

[31] Ensign John Gay, U.S. Navy, *Lieutenant Ron Candiloro, assigned to Fighter Squadron One Five One (VF-151), breaks the sound barrier in an F/A-18 "Hornet".*

[32] Krimigis et al., Science 326 [2009]

[33] NASA/JPL/JHUAPL, *Bubble of Our Sun's Influence.*

2.2 Mathematical Description of Shocks

A shock discontinuity, the surface where the jump in several physical parameters occurs, is indeed a solution of hydrodynamics. However, the hydrodynamic equations are only valid on scales where the medium in question can be described as a fluid, i.e., larger than the mean free path for two-body collisions. However, a real shock is thinner than that and, therefore, needs a different description.

First of all, a shock front is described by its geometrical shape. Since its width is very thin compared to its tangential extension, it can be considered as a thin, locally flat surface. The vector $\boldsymbol{n}$ normal to this surface is called the shock normal[34].

The jump in the physical parameters at the shock front is subject to some conditions which can be derived using the conservation laws for mass, momentum and energy. These conditions are also known as Euler equations[35]. Here we can use them in their one-dimensional form, since we only have variations in the shock-normal direction, which I will denote as the x-direction.

$$\frac{\partial \rho}{\partial t} + \frac{\partial}{\partial x}(\rho v) = 0, \tag{2.1}$$

$$\frac{\partial \rho v}{\partial t} + \frac{\partial}{\partial x}\left(\rho v^2 + p\right) = 0, \tag{2.2}$$

$$\frac{\partial \rho E_m}{\partial t} + \frac{\partial}{\partial x}\left[\rho v \left(E_m + \frac{p}{\rho}\right)\right] = 0, \tag{2.3}$$

whereby $E_m = U_m + 1/2\, v^2$ is the specific total energy of the fluid comprised of the specific internal energy U_m and the specific kinetic energy $1/2\, v^2$.

Solving these equations for a stationary shock, i.e., all temporal derivatives are zero, yields the Rankine-Hugoniot conditions[36,37,38]

$$\rho_u v_u = \rho_d v_d, \tag{2.4}$$

$$\rho_u v_u^2 + p_u = \rho_d v_d^2 + p_d, \tag{2.5}$$

$$\rho_u v_u \left(\frac{v_u^2}{2} + U_{m,u}\right) + p_u v_u = \rho_d v_d \left(\frac{v_d^2}{2} + U_{m,d}\right) + p_d v_d, \tag{2.6}$$

where the indices u and d denote the upstream and the downstream region, respectively.

The above equations give rise to more relations, that can be obtained by using the equation of state for an ideal gas, $H_m = \Gamma/(\Gamma-1)\, p/\rho = \Gamma/(\Gamma-1)\, k_B T/m$, together with the relation for the specific enthalpy $H_m = U_m + p/\rho$. Since the shock is moving through the upstream medium, it is convenient to write the resulting relations in terms of the upstream Mach number $M_{s,u} = v_u/c_{s,u} = v_u\sqrt{\rho_u/\Gamma p_u}$ and the adiabatic index Γ:

$$\frac{\rho_d}{\rho_u} = \frac{v_u}{v_d} = \frac{(1+\Gamma)M_{s,u}^2}{2+(\Gamma-1)M_{s,u}^2}, \tag{2.7}$$

$$\frac{p_d}{p_u} = \frac{(1-\Gamma)+2\Gamma M_{s,u}^2}{1+\Gamma}, \tag{2.8}$$

$$\frac{T_d}{T_u} = \frac{\left[(1-\Gamma)+2\Gamma M_{s,u}^2\right]\left[2+(\Gamma-1)M_{s,u}^2\right]}{(1+\Gamma)^2 M_{s,u}^2}. \tag{2.9}$$

Using equation (2.7), one can estimate the maximum compression ratio of a shock, by setting $M_u \to \infty$ and using $\Gamma = 5/3$ for an ideal gas:

$$\frac{\rho_d}{\rho_u} \approx \frac{1+\Gamma}{\Gamma-1} = 4. \tag{2.10}$$

---

[34] Treumann/Jaroschek, ARXIV [astro-ph] 0805.2132v1 [2008].

[35] Treumann/Jaroschek, ARXIV [astro-ph] 0805.2162v1 [2008].

[36] Rankine, Philosophical Transactions of the Royal Society of London 160 [1870].

[37] Hugoniot, Journal de l'École Polytechnique 57 [1887].

[38] Hugoniot, Journal de l'École Polytechnique 58 [1889].

2.3 Supernova Remnant Shocks

One type of shocks we are interested in within the field of astroparticle physics are the shocks created by supernova remnants. Supernovae are among the most extreme objects in the Universe. The shock wave generated in a supernova explosion travels at a highly supersonic speed of $\approx 10^7\,\mathrm{m\,s^{-1}}$, in some cases even up to 10% of the speed of light through the interstellar medium[39]. A lot of stellar material is ejected in a supernova explosion that amounts to $\approx 1\,M_\odot$. The total energy carried away by the ejecta reaches up to $\approx 10^{63}\,\mathrm{eV}$[40].

On the other hand, supernova remnant shocks present the property of being a very dilute plasma. Compared to the handful of particles per cubic centimetre which can be found in the interstellar medium, the plasma inside a supernova remnant shock is only up to one or two orders of magnitude denser. Therefore, the particles inside the plasma dominantly interact via collective interactions due to the Coulomb force. Such a plasma is called collisionless.

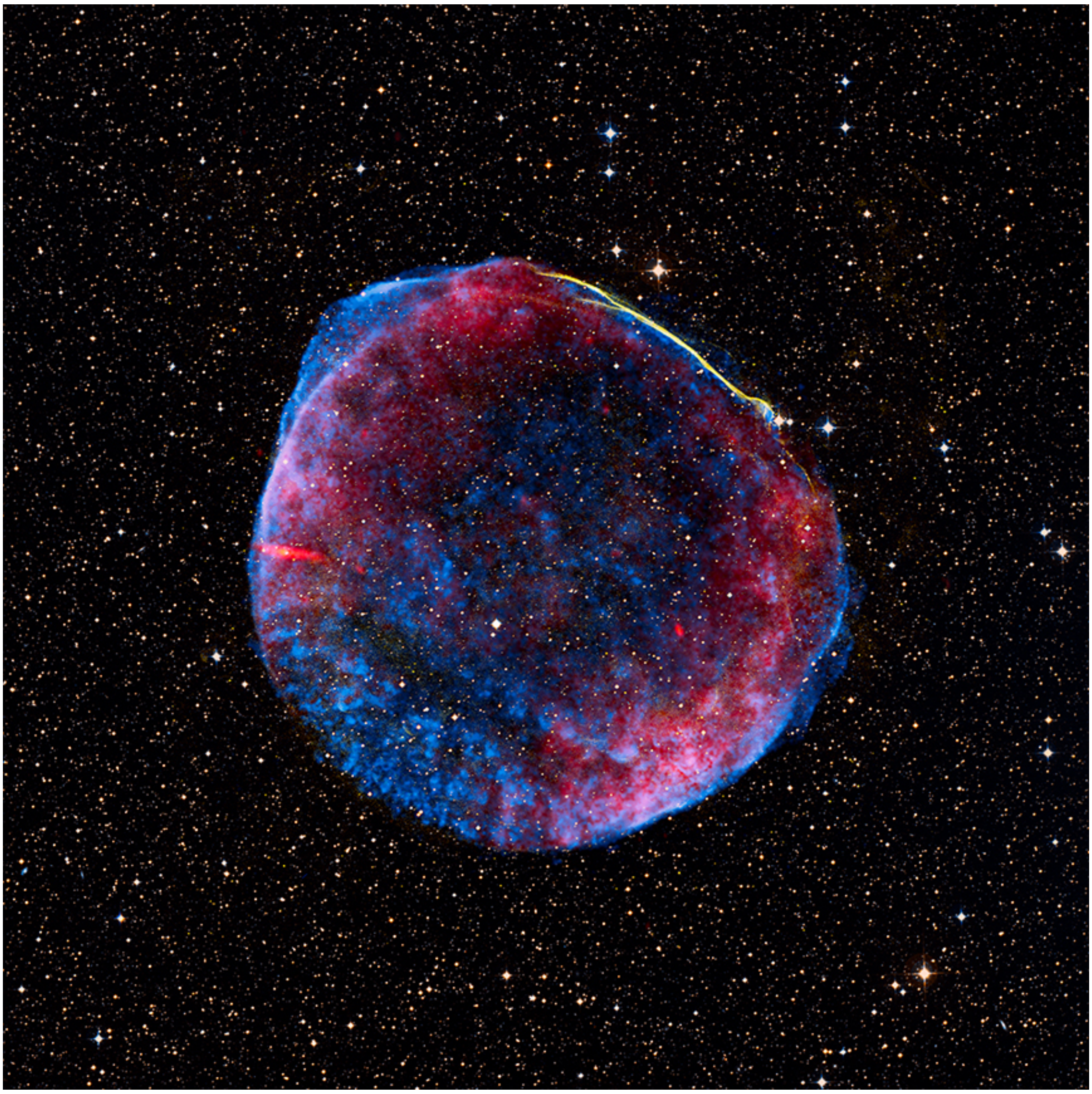

Figure 2.8: This is a composite image of the SN 1006 supernova remnant. Shown here are X-ray data (blue), optical data (yellow, orange and light blue), plus radio data (red). The non-thermal emission of X-rays is a good indicator for the extreme conditions in the outer shell of this supernova remnant.[41]

---

[39] Schawinski et al., Science 321 [2008]

[40] Smartt, Annual Review of Astronomy and Astrophysics 47 [2009].

[41] X-ray: NASA/CXC/Rutgers/G.Cassam-Chenaï, J.Hughes et al.; Radio: NRAO/AUI/NSF/GBT/VLA/Dyer, Mad-

Although it is the final stage in the life of a star, a supernova remnant still evolves. Its evolution can be divided into the following four phases[42]:

- The **free expansion phase** happens in the first $\approx 10^2 - 10^3$ years after the former star went supernova. In this phase the ejecta from the supernova expand freely into the ambient medium and drive a fast and strong forward shock into the latter. The ambient medium is accelerated, compressed and heated in a layer between the contact discontinuity and the forward shock. Its pressure against the out-flowing ejecta causes the creation of a reverse shock and it also causes the ejecta to slow down while it is expanding and adiabatically cooling down.
- The **Sedov-Taylor phase**, which lasts for $\approx 10^4$ years, starts at the time when the accumulated mass of compressed ambient medium at the forward shock equals the mass of ejected material and the free expansion comes to an end. The reverse shock moves inwards and heats the ejecta. The thermal pressure of the hot gas dominates the further expansion of the supernova remnant. During this phase the ejecta continue to expand adiabatically and cool down further.
- During the **snowplough phase**, which lasts for $\approx 10^9$ years, the outer shell of the supernova remnant cools down sufficiently for ionised atoms to capture free electrons and to start radiative cooling. The thermal pressure in the outer shell drops rapidly and the expansion slows down. Only the hotter inner part of the remnant continues to drive the expansion. More ambient medium is swept up by the forward shock until the swept-up mass highly exceeds the mass of the ejecta.
- The final phase, the **fadeaway phase**, sees the break up of the shock structure. When the interior of the supernova remnant has cooled down sufficiently, the expansion speed falls below the speed of sound and the shock wave turns into an ordinary sound wave. The outer shell breaks up into clumps and gradually merges with the ambient medium.

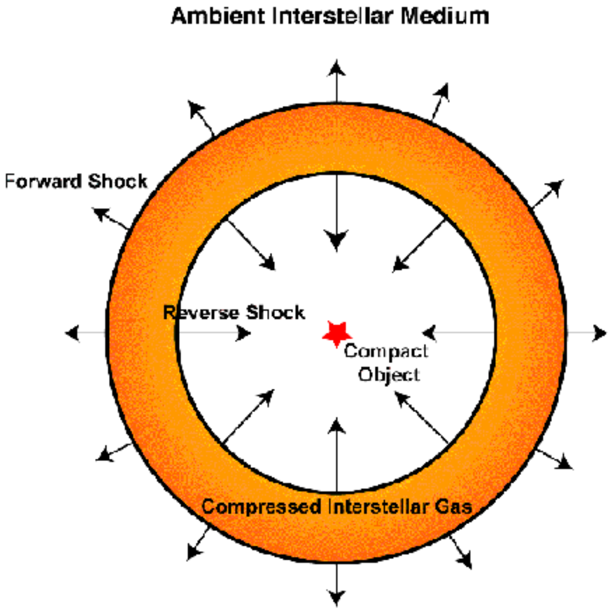

Figure 2.9: This is a sketch of the basic shock structure of a supernova remnant during the first two phases. Comparing this sketch to the previous image in Figure 2.8, one can clearly identify the forward and the reverse shock of the SN 1006 supernova remnant.[43]

---

dalena & Cornwell; Optical: Middlebury College/F.Winkler, NOAO/AURA/NSF/CTIO Schmidt & DSS, *SN 1006: Liberating Star Stuff.*

[42] Reynolds, Annual Review of Astronomy and Astrophysics 46 [2008].

[43] High Energy Astrophysics Science Archive Research Center (HEASARC), Astrophysics Science Division, NASA/GSFC; High Energy Astrophysics Division, Smithsonian Astrophysical Observatory, *SNR Basic Shock Structure.*

2.4 Diffusive Shock Acceleration

The extreme conditions mentioned in the previous Section, are mostly present in the first two evolutionary phases when the forward shock is at its highest speed and sweeps up a great amount of ambient medium. These are also the phases when the non-thermal X-ray emission is strongest. Adding these facts to those mentioned in the introduction (Section 1.2), makes supernova remnant shocks a main suspect for the origin of high-energy cosmic rays.

However, as always, not only the power is necessary, but also the means to do it. In other words, a mechanism is needed to exercise the power contained within a supernova explosion to accelerate particles. Such a mechanism was already proposed over half-a-century ago by Enrico Fermi[44]. One distinguishes between first-order and second-order Fermi acceleration, referring to the order of the velocity of the accelerating object to which the energy gain per interaction is proportional.

Second-order Fermi Acceleration

Second-order Fermi acceleration occurs within the magnetised interstellar medium. A charged particle moving through this medium is reflected by randomly moving "magnetic mirrors". These can be clouds of magnetised plasma. Depending on the direction in which the magnetic mirror moves relative to the incoming particle, i.e., if it is approaching or receding, the particle will either gain or lose kinetic energy, respectively.

Fermi argued, that in an interstellar environment with random motion the probability of head-on collisions is higher than that of head-tail collisions. Therefore, particles would, on average, be accelerated. The energy gain per reflection is proportional to the square of the velocity of the magnetic mirror v_m:

$$\left\langle \frac{\Delta E}{E} \right\rangle \sim \frac{v_m^2}{c^2}. \tag{2.11}$$

First-order Fermi Acceleration

First-order Fermi acceleration occurs in the vicinity of a shock front, which is the reason it is also called diffusive shock acceleration (DSA). In contrast to the second-order acceleration process, the motion of a shock front is not random but rather directional. It was therefore argued by theorists that the acceleration by shock waves would be more efficient[45], since we would expect far more head-on collisions.

The acceleration process is illustrated in Figure 2.10 with a simplified sketch showing a stationary shock, i.e., it is drawn in the shock rest frame. A charged particle ahead of the shock front is scattered at magnetic inhomogeneities in the upstream medium. These can be magnetohydrodynamic (MHD) waves or the same magnetised plasma clouds as in the second-order acceleration process. The particle can be reflected back towards the shock front and, since the upstream medium is flowing towards the shock front at supersonic speed, the particle gains kinetic energy. Nearly the same is true for a particle in the downstream region. Only the change in kinetic energy is different, since the downstream medium is flowing away from the shock front at subsonic speed and, therefore, the particle will lose some energy. However, the amount of energy gained on the upstream side of the shock is far greater than the amount of energy lost on the downstream side.

---

[44] Fermi, Physical Review 75 [1949].

[45] Axford/Leer/Skadron, The acceleration of cosmic rays by shock waves.

A particle in the downstream region has a certain probability of being reflected back to the shock front. The particle flux away from the shock can be given by the downstream particle density and the downstream flow velocity: $n_d v_d$. The particle flux toward the shock can be given by the same particle density and the velocity of the individual particle: $1/4\, n_d v$, where $v \gg v_d$. The fraction of the two fluxes then gives the probability of a particle escaping the shock: $4\, v_d/v$[46]. The particles that make it back to the upstream region can be reflected a second time and thereby gaining kinetic energy proportional to the relative velocity between the upstream and downstream region $v_s = v_u - v_d$:

$$\left\langle \frac{\Delta E}{E} \right\rangle \sim \frac{v_s}{c}. \tag{2.12}$$

The process of shock crossing and particle reflection in the upstream and downstream region can be repeated several times before the particle escapes from the shock. Thereby, particles can be accelerated up to very high energies with a final spectrum which is a power law $\mathrm{d}N(E)/\mathrm{d}E \sim E^{-\gamma}$, with a spectral index $\gamma \gtrsim 2$[47].

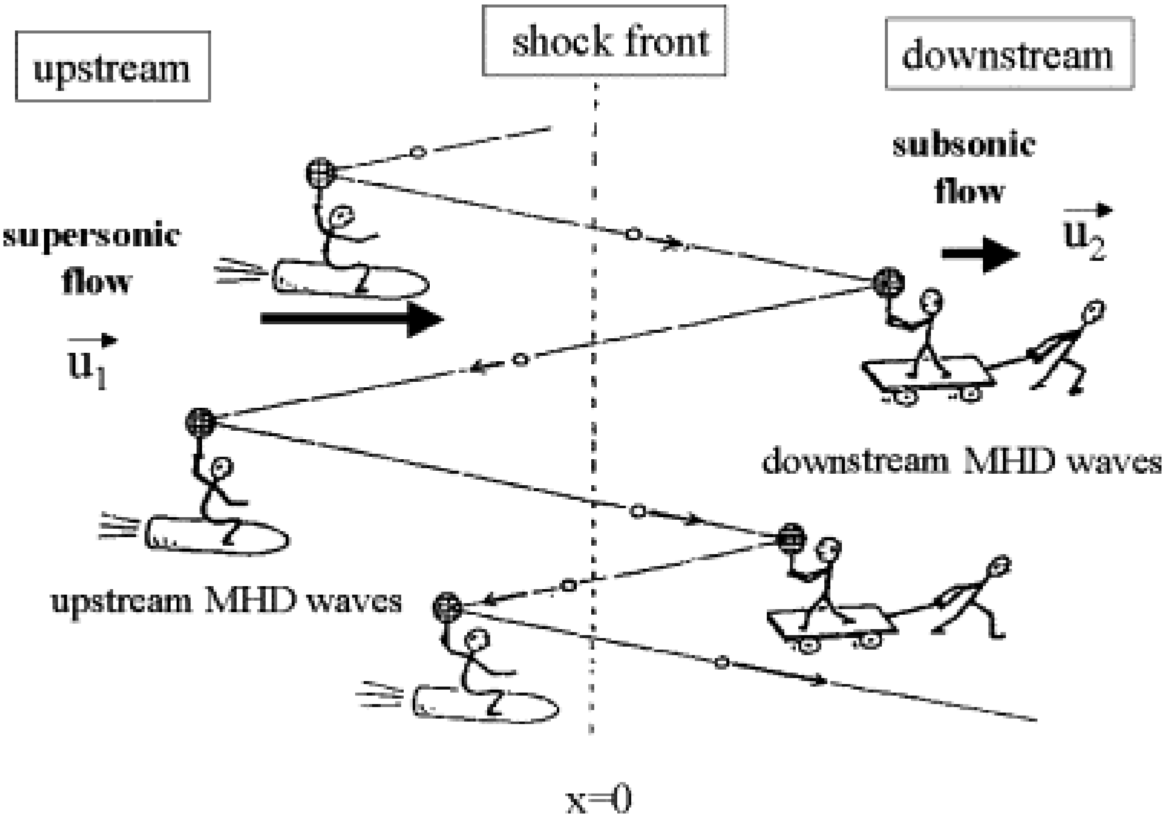

Figure 2.10: This is a cartoon of the diffusive shock acceleration. In diffusive shock acceleration the particles are scattered around the shock moving much faster than the shock. One requirement for this process is the presence of upstream waves and downstream turbulence or waves.[48]

---

[46] Bell, Monthly Notices of the Royal Astronomical Society 182 [1978].

[47] Bell, Monthly Notices of the Royal Astronomical Society 182 [1978].

[48] Manfred Scholer, *Cartoon of the diffusive shock acceleration.*

Open and Solved Questions

Up to a few years ago, there was the question which particle species dominates in the acceleration processes happening in supernova shock fronts. Be it electrons or ions, the associated model was called leptonic or hadronic, respectively. The decisive criterion in this matter is the gamma ray emission detected from supernova remnants. The question that has to be answered is whether this emission comes from bremsstrahlung or from the decay of pions. The former is emitted by leptons scattered at hadronic nuclei. The latter originates from collisions between hadronic nuclei in which neutral pions are created which quickly decay into two gamma rays. Until recently, it was still too difficult to spot the difference in the spectra of supernova remnants. Observations in recent years, however, have shifted the solution to this question in favour of the hadronic model[49,50,51,52].

A still open question is how the particles get injected into the Fermi acceleration processes in the first place. Plasma particles with just a thermal distribution do not have enough initial energy to enter the game of Fermi acceleration, since their mean free path is too small and they get deflected at the shock front. Only particles with more than thermal energy can cross the shock front and "see" the hydrodynamic discontinuity. Therefore, a pre-acceleration mechanism is needed. This is the so-called injection problem[53].

One possible pre-acceleration mechanism is the shock surfing acceleration (SSA)[54]. This process assumes the presence of an electrostatic potential inside the shock front that is caused by the different inertia of electrons and ions. Ions having an energy smaller than this potential are captured inside the shock front and begin to gyrate around the upstream magnetic field. Electrons cannot be reflected by the large-scale shock potential and another process on smaller scales is needed to capture them inside the shock front. Amano/Hoshino (2009) and Matsumoto/Amano/Hoshino (2012) argue that electrostatic waves caused by the Buneman instability can fill this role. If the shock has a magnetic field that is not aligned with the flow direction of the upstream plasma, i.e., the angle between the magnetic field $\boldsymbol{B}$ and the shock normal $\boldsymbol{n}$ is $\theta_{Bn} > 0°$, then the gyrating particles will move parallel to the shock surface along the motional electric field, which is generated by the motion of the upstream plasma towards the shock front.

Another pre-acceleration mechanism is the shock drift acceleration (SDA)[55]. Like SSA, this process also works at shocks with $\theta_{Bn} > 0°$. Particles in the upstream region of the shock can be reflected at the gradient of the magnetic field at the shock front acting as a magnetic mirror. The particle will begin to move parallel to the upstream motional electric field and thereby gain kinetic energy. The same process can also happen to particles that are undergoing SSA and thereby gained enough energy to escape the electrostatic potential inside the shock front. In that way SDA can be a second stage of pre-acceleration following SSA[56].

The overall picture of supernova remnants shows a variety of interesting physical processes happening on vastly different scales. On the level of micro physics, one has the pre-acceleration of particles and their injection into Fermi acceleration processes. While particles get accelerated on the small scales, the supernova remnant expands on the level of macro physics into the surrounding interstellar medium and sweeps up more and more material and, in the end, more particles which can be accelerated. Eventually, particles can escape from the supernova remnant, travel through the interstellar medium on winding paths and finally reach Earth, where we are able to detect these messengers from one of the most extreme environments in the Universe.

---

[49] Giuliani et al., The Astrophysical Journal Letters 742 [2011]

[50] Giordano et al., The Astrophysical Journal Letters 744 [2012]

[51] Ajello et al., The Astrophysical Journal 744 [2012]

[52] Ackermann et al., Science 339 [2013]

[53] Bell, Monthly Notices of the Royal Astronomical Society 182 [1978].

[54] Sagdeev/Shapiro, Letters to Jounal of Experimental and Theoretical Physics 17 [1973].

[55] Krauss-Varban/Wu, Journal of Geophysical Research 94 [1989].

[56] Amano/Hoshino, The Astrophysical Journal 661 [2007].

Chapter 3

Particle-in-Cell Plasma Simulations

Since it is not possible for us to study supernova shock fronts *in situ*, we are bound to model these objects and simulate them with earthbound computers. Besides some others, Particle-in-Cell simulations are among the most used methods to simulate astrophysical plasmas. In this chapter, I will describe which principles are behind this method and how I used this essential tool for my research to do plasma simulations.

3.1 Models for Plasma Simulations

The great challenge of plasma simulations is to find the right representation of the plasma one wants to simulate in the first place.

At large length scales and for collisional plasmas a magnetohydrodynamical (MHD) model is the mostly preferred approach. In this model the plasma or the different particle species the plasma consists of are considered as a fluid. The Navier-Stokes equations of fluid dynamics and Maxwell's equations of electrodynamics govern the temporal evolution of the system consisting of plasma and electromagnetic fields[57]. The fluid elements used in this model only have bulk properties like density and temperature. Therefore, the phase space distribution function of the plasma particles is a Maxwellian and is nearly insensitive to influences by physical processes.

To study in more detail the impact physical processes have on the distribution function, other models are necessary. The so-called hybrid model represents the electrons as a fluid as in a MHD model, and, on the other hand, represents the ions as particles. For the latter, the Lorentz force instead of the Navier-Stokes equations is the equation of motion. However, this approach is only useful if the evolution of the distribution function of one particle species is of interest.

If one is interested in the evolution of the distribution function of all particle species involved, one has to use a fully kinetic model to describe the plasma. This approach is used in Particle-in-Cell (PIC) simulations[58]. It is also necessary to use this representation, if one wants to model a collisionless plasma like those we find in space.

PIC simulations have the advantage of being self-consistent and very accurate in terms of the veracity of the representation of real plasma processes. However, the higher accuracy comes at the cost of higher computational requirements, because using this method requires the simulation to track the path of a large number of particles and update the electromagnetic fields on a large numerical grid. Fortunately, the use of supercomputers and advanced parallelisation techniques allow us to reduce the time a simulation needs to run and have helped to apply PIC simulations to a large variety of problems, like the study of laser-plasma interactions, interactions of the solar wind with Earth's magnetosphere or the acceleration of cosmic ray particles in supernova remnants.

---

[57] Davidson, An Introduction to Magnetohydrodynamics.

[58] Dawson, Reviews of Modern Physics 55 [1983].

3.2 The Principles of Particle-in-Cell Simulations

3.2.1 Basic Equations

Particle-in-Cell simulations are used to sample the phase space distribution function of one or more particle species $f(\boldsymbol{x}, \boldsymbol{p}, t)$. Instead of using the distribution function directly, we use it as a probability distribution for an ensemble of Lagrangian markers, which measure the distribution function at certain points in phase space. For PIC simulations, these markers are so-called macro particles.

The evolution of the phase space distribution function is governed by the Vlasov equation[59]:

$$\frac{\mathrm{d}f}{\mathrm{d}t} = \frac{\partial f}{\partial t} + \boldsymbol{v} \cdot \frac{\partial f}{\partial \boldsymbol{x}} + \left[\boldsymbol{E}(\boldsymbol{x}, t) + \frac{\boldsymbol{v}}{c} \times \boldsymbol{B}(\boldsymbol{x}, t)\right] \cdot \frac{\partial f}{\partial \boldsymbol{p}} = 0. \tag{3.1}$$

Since the Vlasov equation is linear, an ensemble of macro particles is a solution, if the trajectory of every macro particle on its own is a solution. The total distribution function $f(\boldsymbol{x}, \boldsymbol{p}, t)$ is then replaced by a sum over all macro particles $\sum_i f_i(\boldsymbol{x}, \boldsymbol{p}, t)$.

The macro particles used in PIC simulations are characterised by a weight factor w_i, which represents the number of real particles inside one macro particle, and a shape function S, which describes the shape of the macro particles in phase space:

$$f_i(\boldsymbol{x}, \boldsymbol{p}, t) = w_i S(\boldsymbol{x} - \boldsymbol{x}_i(t))\delta(\boldsymbol{v} - \boldsymbol{v}_i(t)). \tag{3.2}$$

Inserting equation (3.2) into the Vlasov equation (3.1) and taking the first moments with respect to $\boldsymbol{x}$ and $\boldsymbol{p}$ leads us to the equations of motion for a macro particle[60,61]:

$$\dot{\boldsymbol{x}} = \boldsymbol{v} = \frac{\boldsymbol{p}}{m} \qquad \text{and} \qquad \dot{\boldsymbol{p}} = q\left[\boldsymbol{E}(\boldsymbol{x}, t) + \frac{\boldsymbol{v}}{c} \times \boldsymbol{B}(\boldsymbol{x}, t)\right], \tag{3.3}$$

where m is the mass of the particle and q is its charge.

To complete the description of the plasma, and thereby adding a description for the electric field $\boldsymbol{E}$ and the magnetic field $\boldsymbol{B}$, the Vlasov equation (3.1) is accompanied by Maxwell's equations to form the Vlasov-Maxwell system:

$$\nabla \times \boldsymbol{B} = \mu_0 \epsilon_0 \frac{\partial \boldsymbol{E}}{\partial t} + \mu_0 \boldsymbol{J}, \tag{3.4}$$

$$\nabla \times \boldsymbol{E} = -\frac{\partial \boldsymbol{B}}{\partial t}, \tag{3.5}$$

$$\nabla \cdot \boldsymbol{E} = \frac{\rho}{\epsilon_0}, \tag{3.6}$$

$$\nabla \cdot \boldsymbol{B} = 0. \tag{3.7}$$

Finally, we add the sources of the electric and magnetic field to this system by defining

$$\rho = \sum_i q_i \int f_i(\boldsymbol{x}, \boldsymbol{p}, t) \mathrm{d}\boldsymbol{p}, \tag{3.8}$$

$$\boldsymbol{J} = \sum_i q_i \int \frac{\boldsymbol{p}}{m} f_i(\boldsymbol{x}, \boldsymbol{p}, t) \mathrm{d}\boldsymbol{p}. \tag{3.9}$$

---

[59] Vlasov, Soviet Physics Uspekhi 10 [1968].

[60] Birdsall/Langdon, Plasma physics via computer simulation.

[61] Hockney/Eastwood, Computer simulation using particles.

3.2.2 Computational Grid

Spatial Grid

Particle-in-Cell simulations use a computational grid to store the information on particles and electromagnetic fields. A possible method to do this, which is widely used nowadays in PIC simulations, is the finite-difference time-domain (FDTD) method proposed by Yee[62]. Figure 3.1 illustrates the grid used in this method.

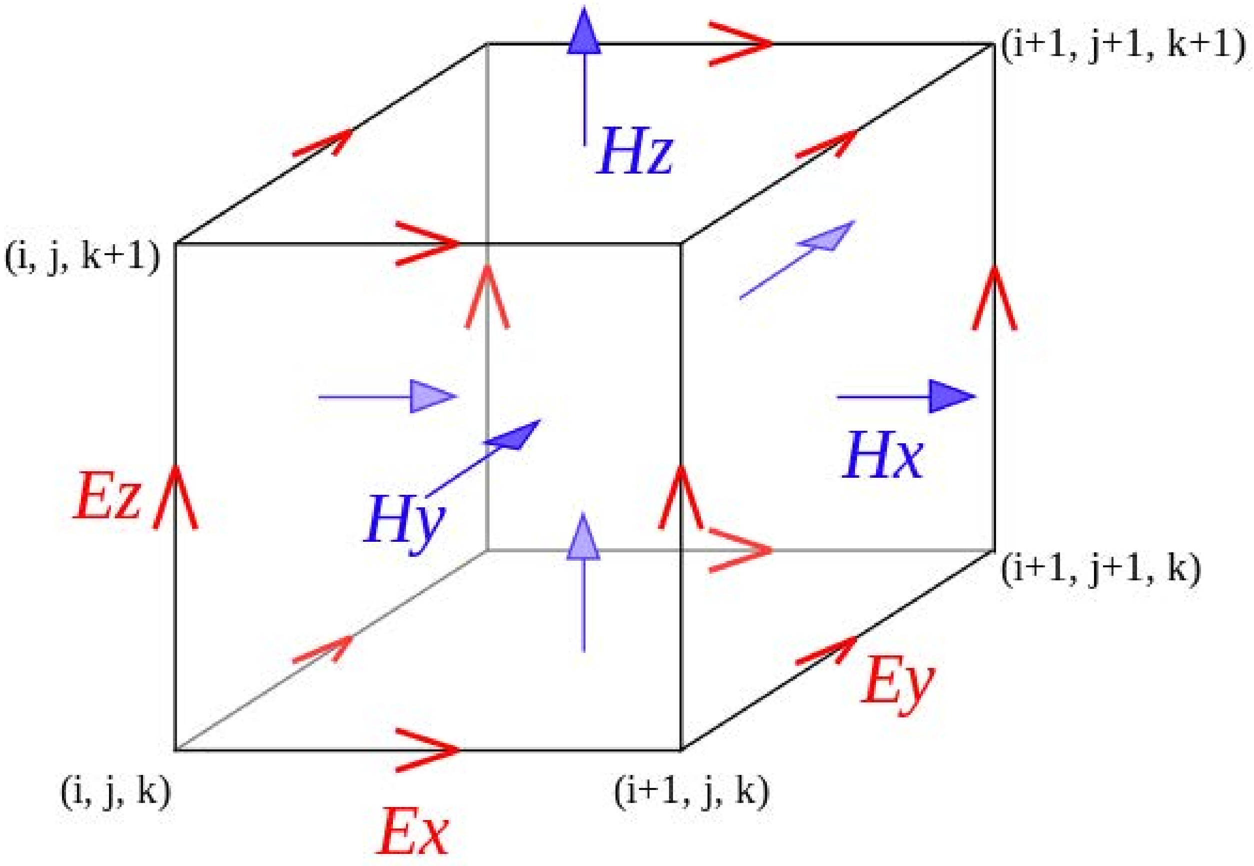

Figure 3.1: This is an illustration of a standard Cartesian Yee cell in three dimensions used for the finite-difference time-domain (FDTD) method, about which electric and magnetic field vector components are distributed.[63]

The electric and magnetic fields are spatially staggered, in order to get the curl of one field right at the position of the other one. For instance, to update the magnetic field B^z at $(i+1/2, j+1/2, k)$, one has to calculate

$$B^z_{i+1/2,j+1/2,k} = (\nabla \times \boldsymbol{E})^z_{i+1/2,j+1/2,k} = \frac{E^y_{i+1,j+1/2,k} - E^y_{i,j+1/2,k}}{\Delta x} - \frac{E^x_{i+1/2,j+1,k} - E^x_{i+1/2,j,k}}{\Delta y},$$

where Δx and Δy is the grid spacing in x- and y-direction, respectively.

Maxwell's equations (3.4) and (3.5) are used in PIC simulations to update the electric and magnetic field at their corresponding grid nodes in a self-consistent manner. Maxwell's other two equations (3.6) and (3.7) are automatically satisfied at each time step if they were satisfied initially. This statement holds true, if the continuity equation $\partial\rho/\partial t + \nabla \cdot \boldsymbol{J} = 0$ is satisfied at all times.

---

[62] Yee, IEEE Transactions on antennas and propagation 14 [1966].

[63] Steven G. Johnson, *Yee-cube*.

Temporal Grid

The phase space coordinates of the particles are staggered on a temporal grid. The positions of the macro particles $\boldsymbol{x}$ are placed at integer time steps, whereas their velocities $\boldsymbol{v}$ are placed halfway between the integer time steps. This so-called leapfrog method[64], as illustrated in Figure 3.2, is a very fast integration method to solve the equations of motion (3.3) and at the same time retains good accuracy.

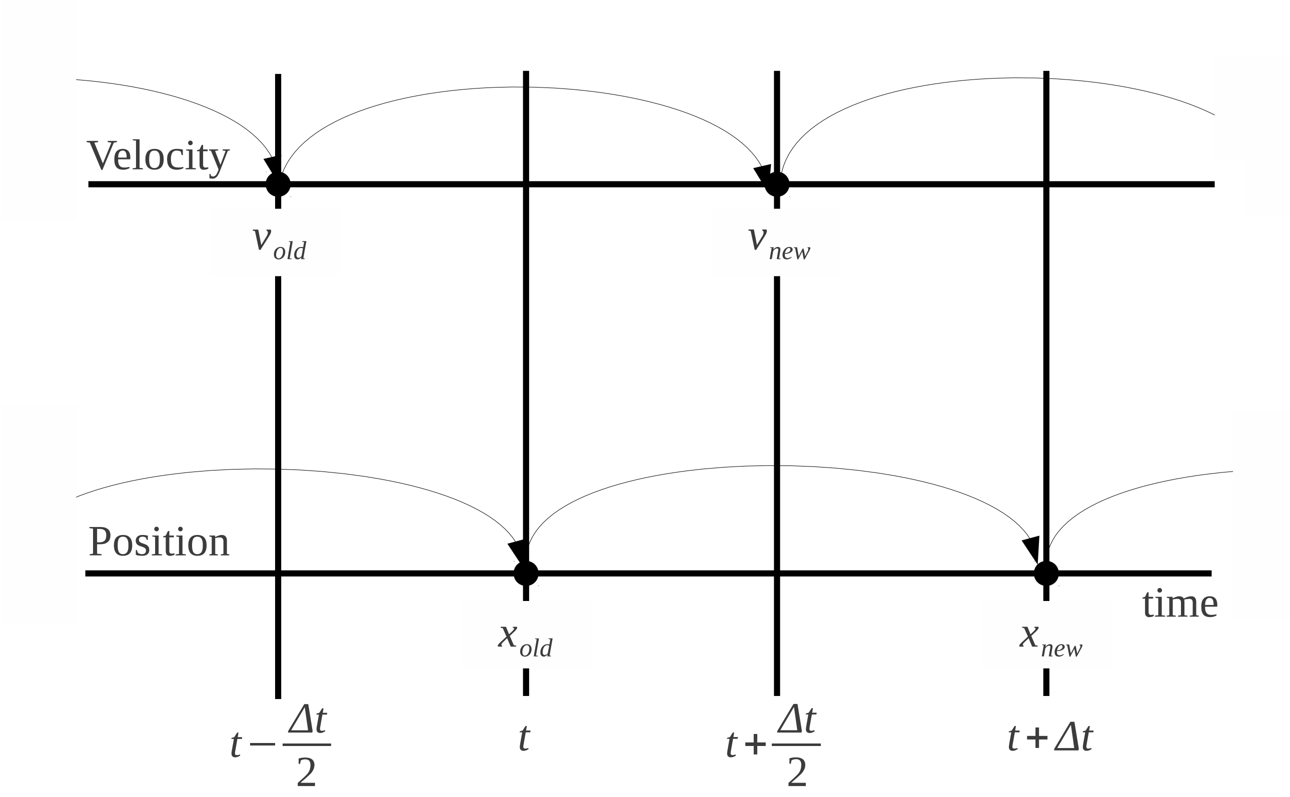

Figure 3.2: This is a schematic illustration of the leapfrog intergration method.

Using this method, the equations of motion (3.3) are replaced by the finite difference equations

$$\frac{\boldsymbol{x}^{t+1}-\boldsymbol{x}^{t}}{\Delta t}=\boldsymbol{v}^{t+1/2} \qquad \text{and} \qquad m\frac{\boldsymbol{v}^{t+1/2}-\boldsymbol{v}^{t-1/2}}{\Delta t}=q\left(\boldsymbol{E}^{t}(\boldsymbol{x}^{t},t)+\boldsymbol{v}^{t}\times\boldsymbol{B}^{t}(\boldsymbol{x}^{t},t)\right), \tag{3.10}$$

where Δt is the temporal grid spacing.

At each time step the electric and magnetic fields are interpolated from the grid nodes to the actual position of each individual particle. The Lorentz force, acting upon each particle, is then calculated and the velocity and the position of all particles are updated according to equations (3.10). Since moving charges always produce a current, these are also accounted for in a PIC simulation and distributed to the according grid nodes to update the electric field.

---

[64] Birdsall/Langdon, Plasma physics via computer simulation.

3.3 Particle-in-Cell Simulations with THISMPI

3.3.1 Code Development History

The number of Particle-in-Cell codes in use is tremendous. As mentioned above, PIC codes can be applied to numerous problems of plasma physics. However, each problem needs its own solution. Therefore, usually for each problem a new PIC code has to be designed.

TRISTAN

The code we use for our studies, originates from the TRISTAN (Tri-dimensional Stanford) code developed by Oscar Buneman in 1990 at Stanford University[65]. Its original purpose was to simulate the interaction of the solar wind with Earth's magnetosphere. Later on, this code was developed further to include the simulation of plasma jets.

To make use of the large parallel computing possibilities which evolved in the last decade, a parallelised version of the TRISTAN code, TRISMPI, was developed by Jacek Niemiec. He used the Message Passing Interface (MPI)[66,67] technology to divide the simulation box into several domains, which independently calculate the updates for particles and fields and communicate with each other via MPI. This code also makes use of the charge-conserving current-deposition scheme proposed by Umeda[68]. The first results using TRISMPI are published in Niemiec et al. (2008).

THISMPI

The next milestone in the development of the code was the adaptation of TRISMPI to a fully 2.5-dimensional code done by Thomas Stroman[69], which received the name THISMPI (Two-and-a-Half-dimensional Stanford code with Message Passing Interface). The fractional dimension refers to the fact that the code uses three dimensions for particle velocities, electric and magnetic field but confines the position of the particles to two dimensions. This practice is also often referred to as "2D3V". Additional modifications include the use of a fourth-order field-pusher proposed by Greenwood[70] and a high-frequency filter proposed by Friedman[71]. THISMPI was used for several simulations and results are published in Stroman/Pohl/Niemiec (2009), Niemiec et al. (2010) and Stroman et al. (2012).

THATMPI

Parallel to the productive use of THISMPI, Jacek Niemiec developed the code further to simulate the shock front arising from the collision of two plasma populations. We called this adapted version THATMPI (Two-and-a-Half-Dimensional Advanced Stanford code with Message Passing Interface). We also included a new particle pusher proposed by Vay[72]. First results with the use of this version are published in Niemiec et al. (2012).

My part in the further development of THATMPI was the new setup for a perpendicular shock, which I will describe in more detail in Section 4.2. Moreover, I did some technical research using THISMPI and THATMPI, which I will describe in Section 3.3.3. Finally, a major part of my work, which must not be underestimated, was the clean-up and optimisation of the heavily unorganised THATMPI and the creation of a detailed documentation for THISMPI and THATMPI, which did not exist before and can now be downloaded here: `http://volkmarwieland.wordpress.com/publications/thismpi-manual`.

---

[65] Buneman, Computer Space Plasma Physics.

[66] Gropp/Lusk/Skjellum, Using MPI.

[67] Gropp/Lusk/Thakur, Using MPI-2.

[68] Umeda et al., Computer Physics Communications 156 [2003]

[69] Stroman, Particle-in-cell simulation of astrophysical plasmas: probing the origin of cosmic rays.

[70] Greenwood et al., Journal of Computational Physics 201 [2004]

[71] Friedman et al., Damped time advance methods for particles and EM fields

[72] Vay, Physics of Plasmas 15 [2008].

3.3.2 THISMPI Characteristics

Although the computational power of modern computer clusters is really tremendous, still we are not able to reproduce nature in a simulation. The great challenge is to find a good compromise between the veracity of the model and the computational resources needed to simulate it. Therefore, with THISMPI and THATMPI we also make several such compromises.

Dimensionality

As mentioned in the previous section, the code operates in 2.5 dimensions. While keeping three components for the fields and the particle velocities, we restrict the particles to a two-dimensional plane. Figure 3.3 illustrates the 2.5-dimensional grid used in our code.

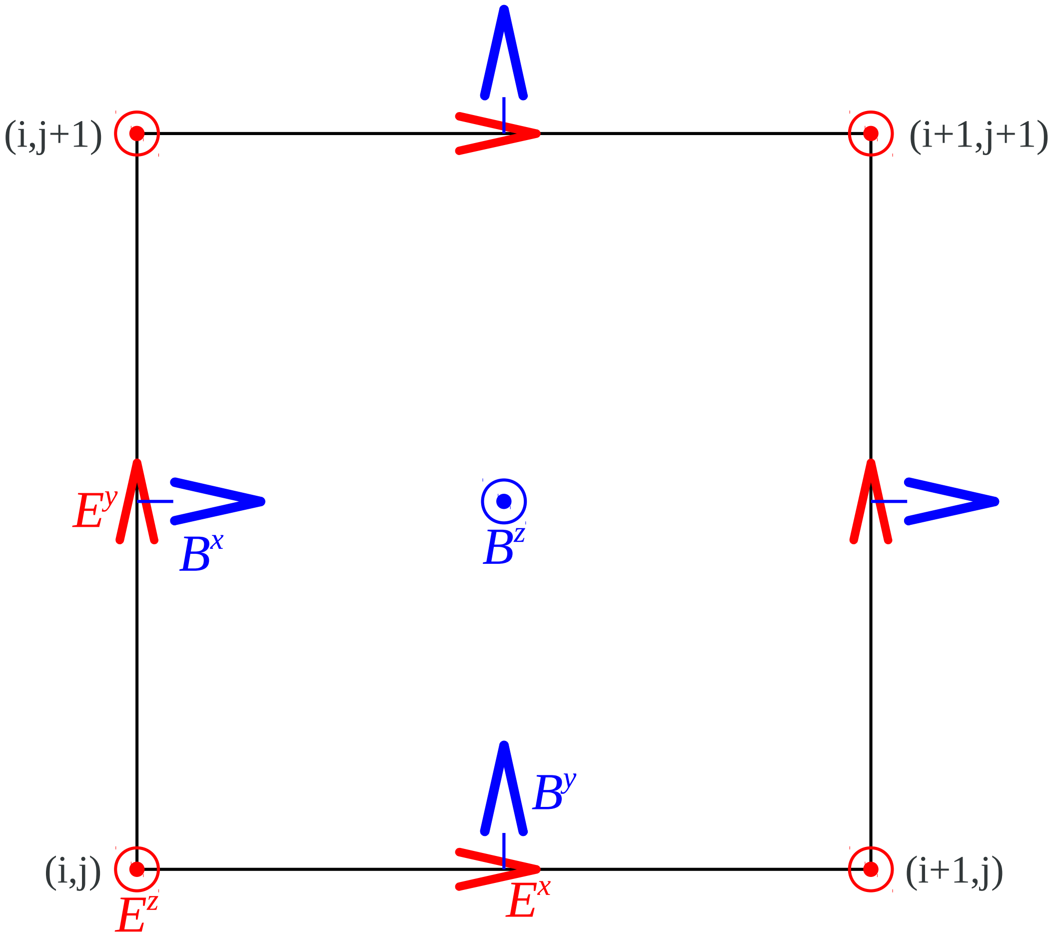

Figure 3.3: This is an illustration of a Cartesian Yee cell in 2.5 dimensions used for the FDTD method in THISMPI and THATMPI, about which electric and magnetic field vector components are distributed.

On the one hand, this reduces the computational expense for the simulation. On the other hand, one has to take great care not to miss important physics. However, if the effects of interest do not require a fully three-dimensional setup to occur, a simulation with reduced dimensionality can provide useful insight into a system's evolution at much lower computational costs. Moreover, realistic three-dimensional PIC simulations may be far beyond our current and near-future computational capabilities, as pointed out by Vladimirov et al.[73]: To follow the acceleration of cosmic ray particles, one may need a simulation with $\approx 10^{11}$ cells in each dimension and $\approx 10^{14}$ time steps.

---

[73] Vladimirov/Bykov/Ellison, The Astrophysical Journal 688 [2008].

Macro Particles

Instead of point-like physical particles, in our PIC code we use macro particles, which comprise many real particles. Therefore, the charge q and the mass m of such a macro particle can be much larger than the real physical values, which makes the numerical handling much easier. Moreover, as long as we maintain the charge to mass ratio q/m, the response of a macro particle to electromagnetic fields will be the same as for a single physical particle. The particles we use are electrons and hydrogen ions, i.e., protons or, for generality, just called ions. We initialise ions and electrons in the same place at the beginning of a simulation in order to achieve an initially neutrally charged simulation box.

Another convenient side-effect of macro particles is their finite size in contrast to point-like physical particles. Where the latter tend to influence each other via Coulomb interaction on approach, the macro particle "clouds" are able to approach each other arbitrarily close without any significant interaction. This makes them an ideal tool to simulate collisionless plasmas, where particles only interact via collective interactions. In our code, the size and shape of the macro particles can be chosen as being a one-cell wide square or a two-cell wide triangle[74], both of which provide a good balance between computation speed and physical accuracy.

Mass Ratio

The considerable difference in mass between protons and electrons is also a point where we have to make a compromise. Since the proton mass m_p is roughly 1836 times larger than the electron mass m_e, the proton plasma frequency $\omega_{pi} = \sqrt{n_p e^2/\epsilon_0 m_p}$ is nearly 43 times smaller than it's electron counterpart for an equal particle number density. Moreover, the proton cyclotron frequency $\omega_{ci} = eB/m_p$ is 1836 times smaller than it's electron counterpart. In an environment like the interstellar medium, where we have magnetic fields with $B \approx 3\,\mu\mathrm{G}$ and $n_e \approx 1\,\mathrm{cm}^{-3}$ [75], electrons would undergo nearly two million plasma oscillations during the same period over which the protons would just complete one gyration. In order to be able to study effects of both electrons and protons in a simulation, we have to reduce the mass ratio m_p/m_e.

One has to take great care at this point not to alter the physics. Antoine Bret and Mark Dieckmann[76] investigated the influence of a reduced mass ratio on the growth rates of various instabilities. Since various systems have a different functional dependency on the mass ratio, it is hard to estimate the influence of a reduced mass ratio on the evolution of instabilities *a priori*. However, one can say that it is likely to under- or overestimate some physical processes in a simulation where m_p/m_e is much smaller than 1836.

Another fact one has to take into account when choosing the proton to electron mass ratio is, up to what size and with what resolution one wants to simulate an astrophysical plasma. On the one hand, the shortest length and time scales are given by the scale on which electron plasma oscillations occur, hence, the electron skin length $\lambda_{se} = c/\omega_{pe}$ and the electron plasma frequency $\omega_{pe} = \sqrt{n_e e^2/\epsilon_0 m_e}$. If the cell size $\Delta \ll \lambda_{se}$ and the time step $\Delta t \ll \omega_{pe}^{-1}$, these oscillations will be sufficiently resolved. On the other hand, the largest length and time scales are given by the proton skin length λ_{si} and the proton plasma frequency ω_{pi}. If these oscillations need to be included in the simulation as well, the size of simulation box and the simulation time must be $L > \lambda_{si}$ and $T > \omega_{pi}^{-1}$ to encompass them. Even larger length and time scales are needed if there are processes involved that occur on scales larger than the proton plasma oscillations. In order to resolve processes of both electrons and protons at a reasonable computational cost, we have to reduce the mass ratio. In our simulations, we usually use the value $m_p/m_e = 50$.

---

[74] Umeda, Study on Nonlinear Processes of Electron Beam Instabilities via Computer Simulations.

[75] Ferrière, Reviews of Modern Physics 73 [2001].

[76] Bret/Dieckmann, Physics of Plasmas 17 [2010].

Unit System

The final compromise is more like a choice of a unit system. Our code makes use of Heaviside-Lorentz units, such that $\epsilon_0 = 1$, $\mu_0 = 1/c^2$ and $\boldsymbol{B} = c\boldsymbol{B}$. Using these units, Maxwell's equations (3.4), (3.5), (3.6), (3.7) read

$$\nabla \times \boldsymbol{B} = \frac{1}{c}\left(\boldsymbol{J} + \frac{\partial \boldsymbol{E}}{\partial t}\right), \tag{3.11}$$

$$\nabla \times \boldsymbol{E} = -\frac{1}{c}\frac{\partial \boldsymbol{B}}{\partial t}, \tag{3.12}$$

$$\nabla \cdot \boldsymbol{E} = \rho, \tag{3.13}$$

$$\nabla \cdot \boldsymbol{B} = 0. \tag{3.14}$$

With the omission of the natural constants ϵ_0 and μ_0, Maxwell's equations become much more symmetric and much easier to handle numerically. The last remaining natural constant in the equations is the speed of light c. However, we have to alter this constant as well, in order to satisfy the Courant condition $c\,\Delta t/\Delta < 1$ [77]. Therefore, in our code we use $c = 0.5$.

---

[77] Courant/Friedrichs/Lewy, Mathematische Annalen 100 [1928].

3.3.3 Technical Investigations

The development of a simulation code always begins with tests of its physical veracity. One has to make sure, that the code does really reproduce the physical system one wants to simulate. That is why thorough testing is needed before a new code or new features of a code can be put into practice. The best way to do this, is to study very simple physical phenomena, that are easy to set up in the simulation and also easy to analyse.

Self-force Analysis

The most simple physical problem conceivable is the analysis of the motion of a single particle in a space devoid of any forces. As we all know from classical mechanics, a freely moving particle should stay in its state of motion without any change. However, in a numerical simulation on a finite computational grid a non-physical "self-force", which the particle induces on itself, could occur[78]. Due to Newton's second law $\boldsymbol{F} = m\boldsymbol{a}$, this manifests as a non-physical acceleration of the particle. An ideal Particle-in-Cell code should be free of this non-physical effect. I investigated if THISMPI satisfies this condition.

To this end, I devised a very simple setup using a single charged test particle with mass $m = 1$ and charge $q = 0.01$ (in simulation units), equipped with its Coulomb field

$$\begin{aligned} \boldsymbol{E} &= \frac{1}{4\pi}\frac{q}{r^3}\boldsymbol{r} \\ \Leftrightarrow \begin{pmatrix} E^x \\ E^y \end{pmatrix} &= \frac{1}{4\pi}\frac{q}{(x^2+y^2)^{3/2}}\begin{pmatrix} x \\ y \end{pmatrix}, \end{aligned} \tag{3.15}$$

and a magnetic field due to its motion, given by the equation

$$\begin{aligned} \boldsymbol{B} &= \frac{1}{4\pi c}\frac{q}{r^3}\boldsymbol{v}\times\boldsymbol{r} \\ \Leftrightarrow B^z &= \frac{1}{4\pi c}\frac{q}{(x^2+y^2)^{3/2}}\left(v^x y - v^y x\right). \end{aligned} \tag{3.16}$$

I discovered that, once the test particle is set into motion, it slows down and eventually oscillates around its initial position. The reason for this is the creation of a "mirror charge" at the position where the particle started in the first place. "Mirror charge" means that a new Coulomb field is created which would correspond to a particle of opposite charge. Its cause is a rearranging process of the particle's Coulomb field once the particle starts to move. In its initial state, the Coulomb field was symmetric. Once the particle starts to move, this symmetric state is no longer stable within our PIC code. The new stable state has an asymmetric deformation in the direction of motion.

To circumvent the "mirror charge" effect and in order to study the free motion of the test particle, I established charge neutrality by initialising a second particle of opposite charge at the same location as the test particle. On the one hand, in that way there was no need to initialise any fields in the beginning that could introduce numerical errors. On the other hand, by moving the second particle very fast in the opposite direction, I was able to remove the influence of the mirror charge and was left with the free motion of the test particle. However, the particle was still subject to a minor deceleration of the order of

$$\boldsymbol{a}_{\text{self}} \approx 10^{-7}\left(\frac{q}{0.01}\right)^2\left(\frac{m}{1}\right)^{-1}\frac{\boldsymbol{v}_0}{|\boldsymbol{v}_0|}. \tag{3.17}$$

The cause of this non-physical acceleration is a small displacement between the symmetry point of the Coulomb field surrounding the particle and the actual position of the particle. Most of the time the symmetry point is a little bit ahead of the particle, hence, the particle is repelled by its own Coulomb field.

We can learn two important lessons from this technical exercise. First, it is more than just a practical approach to initialise both electrons and ions at the same location and start with a neutrally

---

[78] Grigoryev/Vshivkov/Fedoruk, Numerical "Particle-in-Cell" Methods.

charged simulation box. On the one hand, this circumvents the need to initialise all accompanying Coulomb fields around thousands of computational particles and, on the other hand, it avoids the effect of particles oscillating around their starting point. Second, a numerical grid always causes non-physical accelerations on computational particles due to finitely accurate field interpolation. Although it may be small, eventually it can be the cause of non-physical effects occurring in the simulation. However, for our needs the effect is sufficiently small, since most physical processes we are interested in are happening on much shorter time scales.

Scattering Cross Section

The next complexity stage is to add another particle to the simulation. This time we are interested in the scattering behaviour of a lighter test particle at a heavier target particle. Since our goal is to simulate a collisionless plasma, the best we could wish for would be that no scattering occurs. However, even macro particle "clouds" are not perfectly collisionless as we will see.

This scattering experiment was devised as follows. For the test particle I used an electron with mass $m_e = 1$. The target particle was a proton with mass $m_i = 50$ (all in simulation units). The much higher mass of the ion ensures that its movement can be neglected for the case of this simulation. The target particle was again equipped with its Coulomb field

$$\begin{aligned} \boldsymbol{E} &= \frac{1}{4\pi}\frac{q}{r^3}\boldsymbol{r} \\ \Leftrightarrow \begin{pmatrix} E^x \\ E^y \end{pmatrix} &= \frac{1}{4\pi}\frac{q}{(x^2+y^2)^{3/2}}\begin{pmatrix} x \\ y \end{pmatrix}, \end{aligned} \tag{3.18}$$

whereas for the test particle I used the same trick as described in the previous section to get rid of the non-physical mirror charge. For several different values of the impact parameter b I recorded the scattering angle θ.

The resulting scattering angles have a maximum at an impact parameter of one grid cell, which is also the minimum impact parameter due to the size of the macro particle "cloud". This maximum scattering angle amounts to a very good value of $\theta_{\max} \ll 1^\circ$ for an initial test-particle velocity $v_0 = 0.2c$. Repeating the same experiment for different initial velocities, yields an estimate for the maximum momentum transfer per time step during a two-body Coulomb interaction of $|\Delta p/\Delta t| \approx 10^{-5}$. Since in our actual simulations we have many electrons and protons per grid-cell, we could expect substantial shielding of the particle's Coulomb fields. Moreover, two-body collisions are always random, which would yield in a nearly equal amount of momentum transfers with positive and negative value. Therefore, we can conclude that interactions of this kind are negligible.

However, our simulations do not contain only two particles but thousands of them. Therefore, it is also important to get an estimate of the scattering behaviour of a test particle in a cloud of randomly distributed electrons and ions. To this end, I devised a simulated recreation of the classical Rutherford experiment.

Basically, I used the same setup as for the two-body scattering experiment. Instead of a single target particle, I used a "foil" which was several grid cells wide and a few grid cells thick and consisted of the same number of randomly distributed electrons and ions. The test particle penetrated the "foil" at different locations and for each run of the experiment I recorded the final scattering angle at which the particle left the target on the other side.

The results show that particles with initial velocities at a considerable fraction of the speed of light are only subject to minor scattering with $\theta \ll 1^\circ$. However, particles with initial velocities of $v_0 \lesssim 0.03c$ can be artificially scattered on timescales comparable to the time of a real simulation if the randomly distributed charges are not sufficiently balanced. Since most of the particles in our real simulations, especially those in the post-shock region, are considerably faster, this artificial scattering does not affect the process of electron acceleration.

Summarising the results, we can claim with good confidence that the assumption of a collisionless plasma is valid for the PIC simulations we conduct with THISMPI. The above results are my contribution to Niemiec et al. (2012).

Scaling Tests

Another critical aspect of doing large computer simulations is the so-called scalability of a simulation code. Today we are able to use large computational resources. However, the question is if one is able to use them efficiently. With parallel computing the execution of a programme can be splitted into several parts and distributed to several processors or processor cores. Doing this, a gain in execution speed is the most notable difference compared to execution on one processor. The challenge for code developers now lies within the means of how to parallelise their code such that it can use the available resources most efficiently.

THISMPI is parallelised in the following way. The simulation box is divided into several domains which are distributed to the same number of processes, which independently calculate the updates for particles and fields. Particles and field components which are crossing domain boundaries are communicated between domains via MPI. In that way, only the initial setup of MPI, the communication between the domains and the writing of output add up to the sequential part of THISMPI. All other parts of our code can be perfectly run in parallel. Therefore, we would expect excellent scalability results.

The scalability of a code is measured by two values[79]: speedup and parallelisation. The theoretical speedup of a programme $S(N)$ compares the time the programme's execution needs on N processors T_N compared to the execution time on one processor T_1:

$$S(N) = \frac{T_1}{T_N}. \tag{3.19}$$

The ideal speedup is obtained if $T_N = T_1/N$ and, therefore $S(N) = N$. Most of today's simulation programmes do not reach the ideal value. Nevertheless, many programmes are able to reach linear speedup, i.e., $S(N) = \alpha N$, with $\alpha < 1$.

To test the speedup of THISMPI, I divided the same simulation box into more and more domains, which is called strong scaling, and distributed them to several independent processes on the PAX cluster at DESY Zeuthen[80]. Comparing the execution times T_N, yields a very good speedup for THISMPI of $S(N) \approx 0.75N$.

The parallelisation of a code is a statement of how good it is parallelised, i.e., how big the parallel portion of the code's execution time is compared to the total execution time. It can be estimated by

$$P_{\text{est}} = \frac{1/S(N) - 1}{1/N - 1}. \tag{3.20}$$

To test the parallelisation of THISMPI, I used the values for the speedup $S(N)$ from the speedup test. The results show, that P_{est} already reaches an excellent 99% for 32 processor cores. Scaling tests performed on even bigger computer clusters confirm that our code shows very good parallelisation results up to about ten thousand cores.

Besides strong scaling there is also weak scaling. Here the size of the simulation box is increased under the condition of a fixed problem size per processor, i.e., we just add up more and more equally sized domains. An ideally paralellised code should maintain a constant execution time, regardless of the number of domains.

Again I used the PAX cluster at DESY Zeuthen to test the weak scalability of THISMPI. The results show, that the simulation time indeed stays nearly constant, regardless of the number of domains used for the test.

Summarising all results, we can claim that THISMPI is a code that is fit for running on super computers housing thousands or even ten thousands of processor cores with excellent strong and weak scalability.

---

[79] Amdahl, Validity of the Single Processor Approach to Achieving Large-Scale Computing Capabilities.

[80] More information on the PAX cluster can be found here: `http://www-zeuthen.desy.de/technisches_seminar/texte/waschk_20100427.pdf`

Chapter 4

Perpendicular Shock Front Simulation

The main part of my work was to develop a setup for our Particle-in-Cell (PIC) code THATMPI that is able to simulate a shock front with a magnetic field $\boldsymbol{B}_0$ perpendicular to the shock normal $\boldsymbol{n}$. There are different methods to devise such a setup. In this chapter, I will describe which method I chose and what distinguishes it from others. Furthermore, I will show the results of my simulations and compare them to the simulation results achieved with the THATMPI version with parallel magnetic field and to results from other groups.

4.1 How to Build a Shock Front

As described in Section 2.1, a shock front is characterised by a sudden jump in several physical parameters, like particle density, particle velocity and temperature. If a simulated recreation of a shock wants to be true to the real conditions of shock physics, it needs to include these jumps. Although this is the one common goal for all shock simulations, the way to get there can be utterly different.

Injection Method

The injection method is sometimes also called reflection, wall or piston method and was first used by Burgess et al.[81] in hybrid simulations.

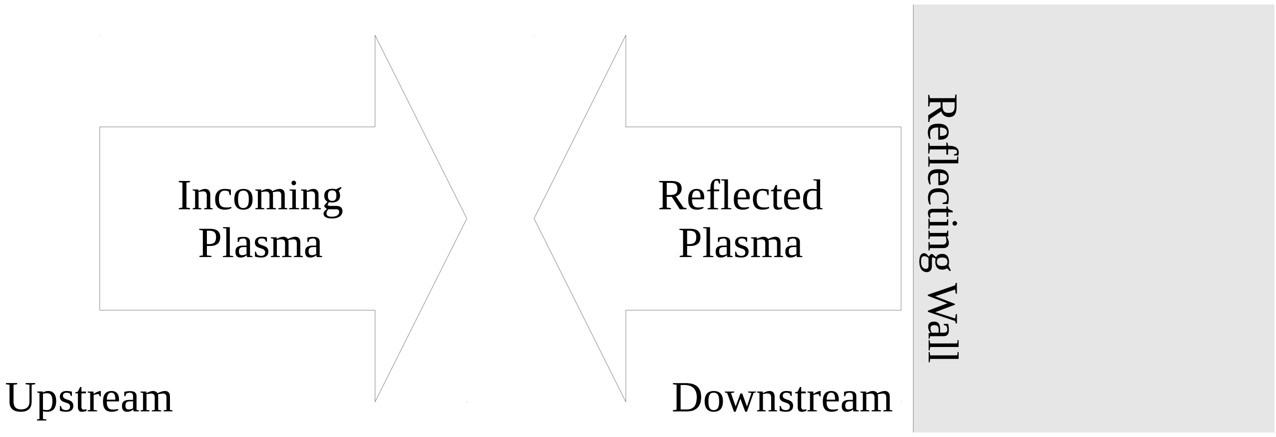

Figure 4.1: This is an illustration of the injection method showing the directions of motion of the incoming and reflected plasma.

---

[81] Burgess/Wilkinson/Schwartz, Journal of Geophysical Research: Space Physics 94 [1989].

Using this method, the simulated plasma is injected from one side of the simulation box and streams towards the other side. The other end of the simulation box represents a conducting wall, i.e., every particle that reaches this boundary is reflected back. Once the reflected particles interact with the incoming particles, a collisionless shock is formed.

The whole simulation is placed in the downstream rest frame and the shock front propagates upstream. Automatically, one has the disadvantage of only having one shock (see Figure 2.2). Moreover, this method assumes the existence of an infinitely sharp contact discontinuity.

Relaxation Method

The relaxation method was also first used in hybrid simulations by Leroy et al.[82,83].

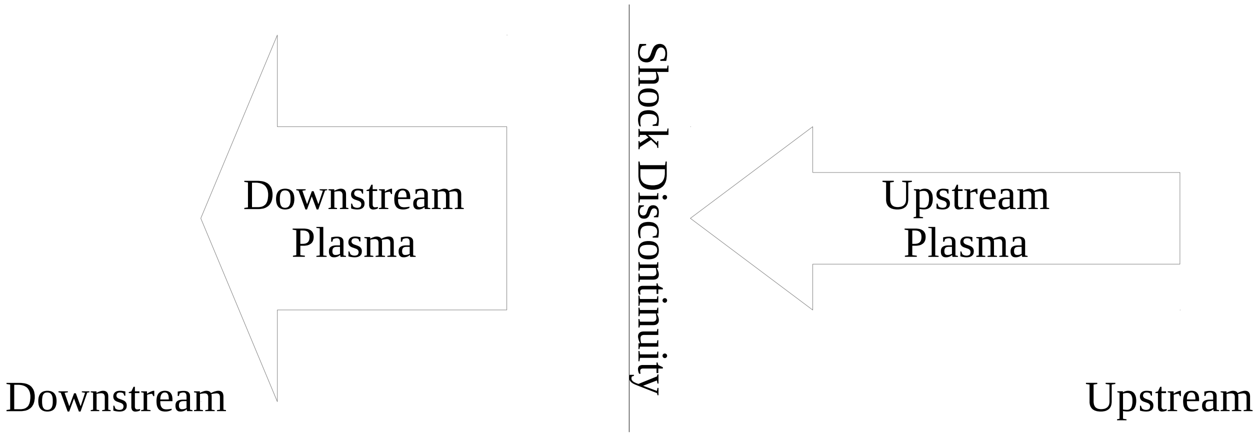

Figure 4.2: This is an illustration of the relaxation method showing the directions of motion of the two plasma populations.

Using this method, the simulation starts with a simulation box already filled with plasma. The plasma is separated by a discontinuity into two uniform plasma slabs that initially satisfy the shock jump conditions. One is then free to choose the physical parameters of one of the regions. The parameters for the other region are obtained by solving for the shock jump conditions as described in Section 2.2.

The simulation is placed in the shock rest frame. This method has the same disadvantages as the injection method of having only one shock (see Figure 2.2) and of assuming an initially infinitely sharp discontinuity. Another disadvantage might be the need to calculate the physical parameters out of the shock jump conditions. For instance, in order to determine a unique initial downstream state, one needs all physical parameters of the upstream region and one additional parameter of the downstream region. In that way, the initial state of the downstream region is always bound to the initial state of the upstream region. One has no freedom to choose the downstream parameters by oneself.

---

[82] Leroy et al., Geophysical Research Letters 8 [1981].

[83] Leroy et al., Journal of Geophysical Research: Space Physics 87 [1982].

Collision Method

Our group developed a new setup, which has some similarities to the relaxation method but adds more freedom to choose the physical parameters, which is called the collision method.

This setup also starts with a simulation box filled with plasma separated into two uniform regions. But in contrast to the relaxation method, the plasma slabs are not separated by a sharp discontinuity but by a void. The two regions are then allowed to move towards each other. Once they collide, they begin to form a double shock (see Figure 2.3).

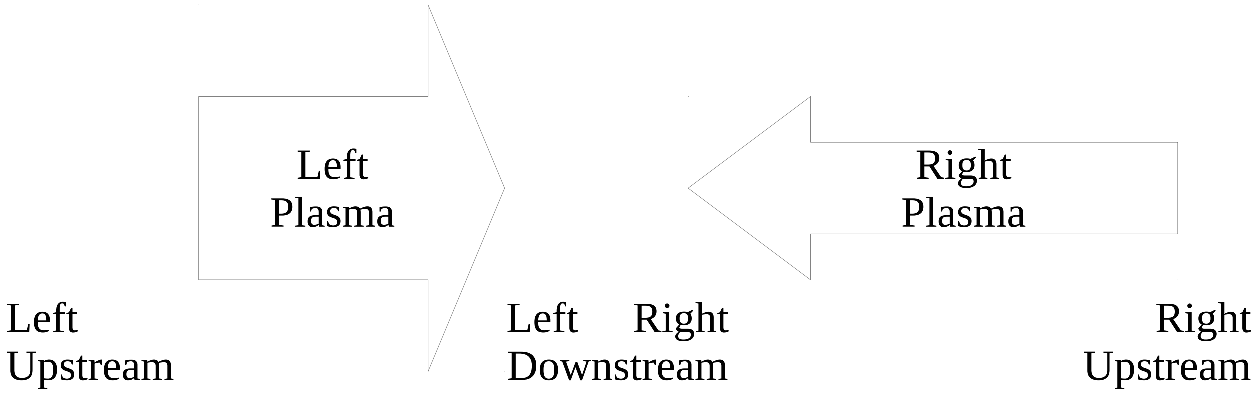

Figure 4.3: This is an illustration of the collision method showing the directions of motion of the two plasma populations.

Our simulation is placed in the centre-of-momentum frame. In contrast to the injection and the relaxation method, the collision method leads to the development of two shocks from first principles without assuming the existence of a discontinuity in the first place. Moreover, one has full freedom to choose the physical parameters for both plasmas.

Using this very easy and clean method, one can study physical processes in a variety of astrophysical plasma shocks. The setup as described above can be used to simulate unmagnetised shocks, but one can also add a magnetic field to this basic setup to simulate magnetised shocks. It has already proven its merits for the simulation of unmagnetised and magnetised parallel shocks[84], where the magnetic field $\boldsymbol{B}_0$ is parallel to the shock normal $\boldsymbol{n}$.

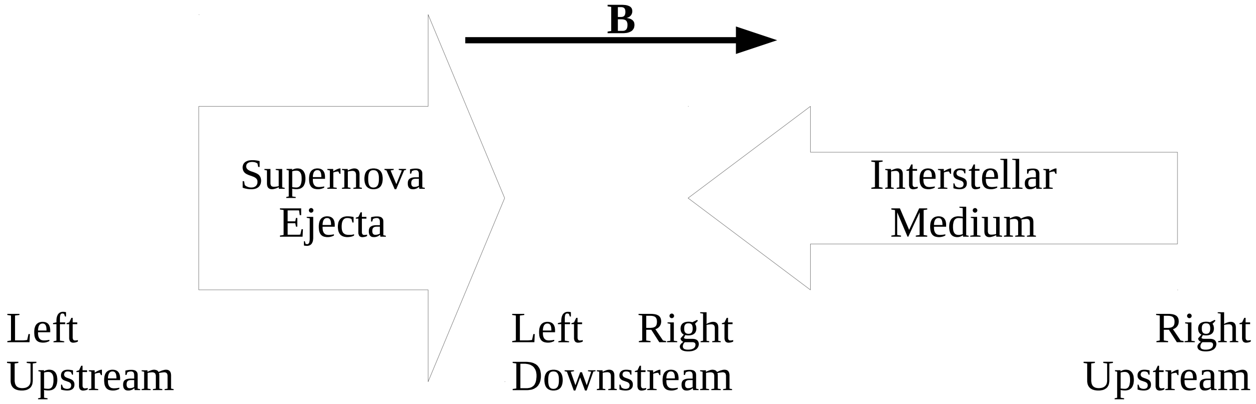

Figure 4.4: This is an illustration of the THATMPI setup for a parallel shock showing the directions of motion of the two plasma populations and the direction of the magnetic field.

---

[84] Niemiec et al., The Astrophysical Journal 759 [2012].

4.2 Simulation of a Perpendicular Shock Front

In our recent work, Niemiec et al. (2012) (hereafter N2012), we studied unmagnetised shocks (with Alfvénic Mach number $M_A \to \infty$) and weakly magnetised strictly parallel shocks, i.e., with $M_A \approx 22$ and $\theta_{Bn} = 0°$. In both cases we observed the development of a double-shock structure consisting of a forward shock, a reverse shock and a contact discontinuity (CD). We showed that while non-relativistic shocks in both unmagnetised and magnetised plasmas can be mediated by Weibel-type instabilities, the efficiency of shock-formation processes is higher when a large-scale magnetic field is present. We observed mainly filamentation-like instabilities out of which the shock structure eventually arises. The particle distributions we observed at the end of our simulations exhibited no significant evidence of pre-acceleration. However, we noted that we still had anisotropy in the ion distribution by that time.

After we studied parallel shocks in great detail, it was the next logical step to move on to perpendicular shocks. It was my task to develop a new setup for our code to accomplish this. With this new setup for perpendicular shocks we anticipated new insight into the processes operating in supernova shock fronts and, at best, a solution to the injection problem. The content of the remaining sections in this chapter are taken from a forthcoming paper that is going to be published together with Martin Pohl, Jacek Niemiec, Iman Rafighi and Ken-Ichi Nishikawa[85].

A naive approach to set up a magnetised plasma system would be to establish a homogeneous magnetic field $\boldsymbol{B}_0$ perpendicular to the streaming direction of the plasma beams throughout the whole simulation box. Since the simulation is done in the centre-of-momentum frame, one has to perform two separate Lorentz transformations for each of the two counter-streaming plasmas. In the non-relativistic limit, the transformations for the electric and magnetic field are defined as $\boldsymbol{E} = \boldsymbol{E}' + \boldsymbol{v} \times \boldsymbol{B}'$ and $\boldsymbol{B} = \boldsymbol{B}'$, respectively, where $\boldsymbol{E}'$ and $\boldsymbol{B}'$ are the electric and magnetic field measured in the rest frame of the plasma, and $\boldsymbol{v}$ is the velocity of the new frame relative to the plasma rest frame, which, in each case, has the opposite sign of the streaming velocities of the two plasma slabs in our simulation. In the plasma rest frame, the electric field is $\boldsymbol{E}' = 0$. In our simulation the two plasmas have streaming velocities v_L^x and v_R^x - the indices L and R refer to the initial position of the plasmas on the *left* and *right* side of the simulation box, respectively - and the magnetic field is aligned in y-z-direction, which leads to

$$\begin{pmatrix} E_L^x \\ E_L^y \\ E_L^z \end{pmatrix} = \begin{pmatrix} 0 \\ v_L^x B_L^z \\ -v_L^x B_L^y \end{pmatrix} \quad \text{and} \quad \begin{pmatrix} E_R^x \\ E_R^y \\ E_R^z \end{pmatrix} = \begin{pmatrix} 0 \\ v_R^x B_L^z \\ -v_R^x B_L^y \end{pmatrix}. \tag{4.1}$$

Since v_L^x and v_R^x have opposing signs, the motional electric field has opposing signs in the two plasmas, which is illustrated in Figure 4.5. Without further modification, this setup would lead to the creation of an artificial dipole in the middle of the simulation box, that would induce a transient by large $\nabla \times \boldsymbol{E}$ contributions that may limit the veracity of the simulation.

---

[85] Wieland et al., The Astrophysical Journal 2014

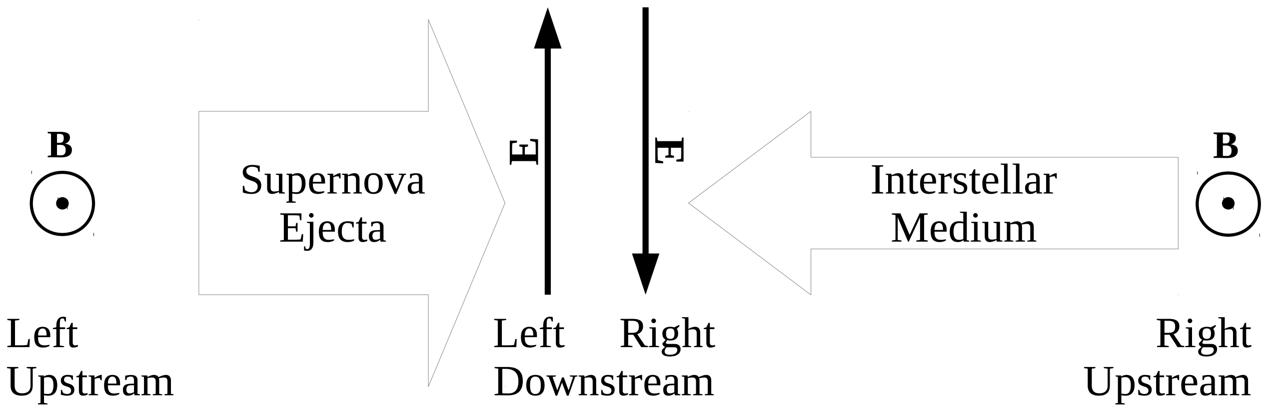

Figure 4.5: This is an illustration of the setup for a perpendicular shock showing the directions of motion of the two plasma populations and the directions of the magnetic field and motional electric field.

In order to avoid the creation of this artificial dipole antenna, we developed a setup with a transition zone between a full motional electric field inside the plasmas and zero electric field in the plasma-free area between the two slabs. This is achieved by implementing a spatial gradient in the perpendicular magnetic fields B^y and B^z ahead of the colliding plasma slabs. The transition zone in the electric field automatically follows from the Lorentz transformations.

To establish the transition zone, the new setup uses a cosine function in the magnetic field at the edge of both plasma slabs ($x_{0L} \leq x \leq x_{0L} + w_{\text{grad}}$ and $x_{0R} + w_{\text{grad}} \leq x \leq x_{0R}$, respectively):

$$\begin{aligned} B^y_L(x) &= \frac{B_0}{2\sqrt{2}}\left[\cos\left(\frac{x - x_{0L}}{w_{\text{grad}}}\pi\right) + 1\right], \qquad & B^y_R(x) &= \frac{B_0}{2\sqrt{2}}\left[\cos\left(\frac{x - x_{0R}}{w_{\text{grad}}}\pi\right) + 1\right], \\ B^z_L(x) &= \frac{B_0}{2\sqrt{2}}\left[\cos\left(\frac{x - x_{0L}}{w_{\text{grad}}}\pi\right) + 1\right], \qquad & B^z_R(x) &= \frac{B_0}{2\sqrt{2}}\left[\cos\left(\frac{x - x_{0R}}{w_{\text{grad}}}\pi\right) + 1\right], \end{aligned} \tag{4.2}$$

where B_0 is the value of the homogeneous magnetic field inside the plasma slabs. The full magnetic field inside the left and right plasma extends from the left box boundary up to x_{0L} and from x_{0R} up to the right box boundary, respectively, while the transition zone extends from x_{0L} to $x_{0L} + w_{\text{grad}}$ and from $x_{0R} - w_{\text{grad}}$ to x_{0R}, respectively. The factor $2\sqrt{2}$ appears due to two normalizations, the first being the normalization of the term in brackets to values between 0 and 1 and the second being $|\boldsymbol{B}| = B_0$. Outside the plasma slabs the magnetic field is $B^y = B^z = 0$.

Lorentz transformation then yields the following relations for the electric field inside the two plasma slabs ($x < x_{0L}$ and $x > x_{0R}$, respectively):

$$\begin{aligned} E^y_L &= \frac{v^x_L B_0}{\sqrt{2}}, \qquad & E^y_R &= \frac{v^x_R B_0}{\sqrt{2}}, \\ E^z_L &= -\frac{v^x_L B_0}{\sqrt{2}}, \qquad & E^z_R &= -\frac{v^x_R B_0}{\sqrt{2}}, \end{aligned} \tag{4.3}$$

and the following relations in the transition zone ($x_{0L} \leq x \leq x_{0L} + w_{\text{grad}}$ and $x_{0R} + w_{\text{grad}} \leq x \leq x_{0R}$, respectively):

$$\begin{aligned} E^y_L(x) &= \frac{v^x_L B_0}{2\sqrt{2}}\left[\cos\left(\frac{x - x_{0L}}{w_{\text{grad}}}\pi\right) + 1\right], \qquad & E^y_R(x) &= \frac{v^x_R B_0}{2\sqrt{2}}\left[\cos\left(\frac{x - x_{0R}}{w_{\text{grad}}}\pi\right) + 1\right], \\ E^z_L(x) &= -\frac{v^x_L B_0}{2\sqrt{2}}\left[\cos\left(\frac{x - x_{0L}}{w_{\text{grad}}}\pi\right) + 1\right], \qquad & E^z_R(x) &= -\frac{v^x_R B_0}{2\sqrt{2}}\left[\cos\left(\frac{x - x_{0R}}{w_{\text{grad}}}\pi\right) + 1\right], \end{aligned} \tag{4.4}$$

where the factors $\sqrt{2}$ and $2\sqrt{2}$ again appear due to normalization.

In order to achieve a stable gradient, one has to compensate for any electric field arising from $\nabla \times \boldsymbol{B}$. This is done by imposing a current sheet in the transition zone, which leads to

$$\frac{\partial \boldsymbol{E}}{\partial t} = c\nabla \times \boldsymbol{B} - \boldsymbol{J} = 0. \tag{4.5}$$

The derivation of the current $\boldsymbol{J}$ is rather simple. Since we only have $\partial B^y/\partial x$ and $\partial B^z/\partial x$, we just need to set up a compensating current in y- and z-direction, such that $J^y = -c\,\partial B^z/\partial x$ and $J^z = c\,\partial B^y/\partial x$. Moreover, due to $\boldsymbol{J} = nq\boldsymbol{v}_{\text{rel}}$, where n is the particle density in the corresponding plasma, which is kept constant throughout the whole extent of the plasma including the transition zone, q is the particle charge and $\boldsymbol{v}_{\text{rel}}$ is the particle velocity relative to the plasma slabs, one just has to differentiate equation (4.2) with respect to x, multiply it with c and divide it by nq to obtain the necessary distributions of the relative particle velocity in the current sheet:

$$\begin{aligned} v^y_{\text{rel},L}(x) &= \frac{B_0 c\pi}{2\sqrt{2}n_L q w_{\text{grad}}} \sin\left(\frac{x - x_{0L}}{w_{\text{grad}}}\pi\right), & v^y_{\text{rel},R}(x) &= \frac{B_0 c\pi}{2\sqrt{2}n_R q w_{\text{grad}}} \sin\left(\frac{x - x_{0R}}{w_{\text{grad}}}\pi\right), \\ v^z_{\text{rel},L}(x) &= -\frac{B_0 c\pi}{2\sqrt{2}n_L q w_{\text{grad}}} \sin\left(\frac{x - x_{0L}}{w_{\text{grad}}}\pi\right), & v^z_{\text{rel},R}(x) &= -\frac{B_0 c\pi}{2\sqrt{2}n_R q w_{\text{grad}}} \sin\left(\frac{x - x_{0R}}{w_{\text{grad}}}\pi\right), \end{aligned} \tag{4.6}$$

where n_L and n_R are the plasma particle densities in the left and the right plasma population, respectively, and an additional factor of -1 was applied for v^y_{rel} due to $J^y = -c\,\partial B^z/\partial x$.

Figure 4.6 illustrates the setup of the transition zone as described above.

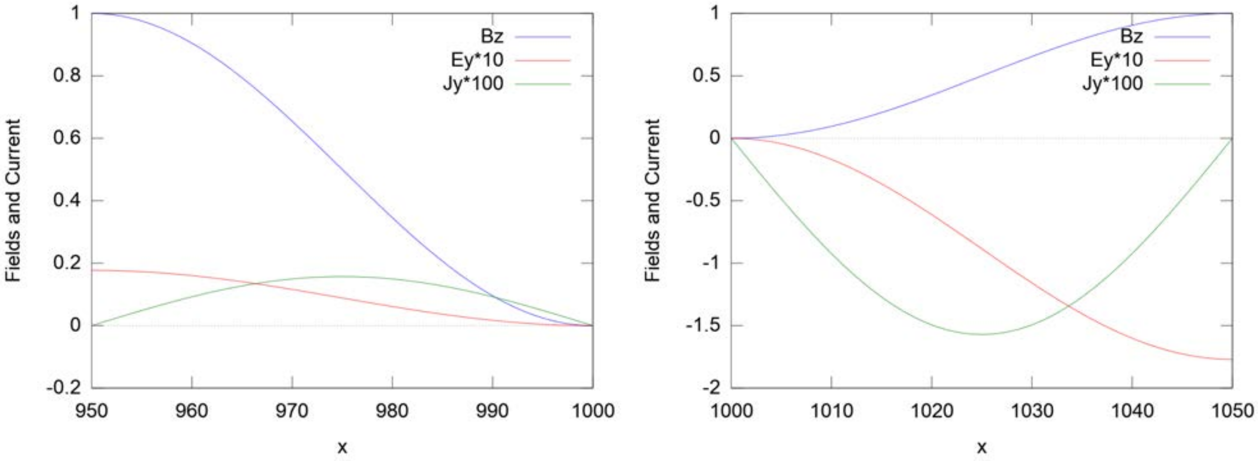

Figure 4.6: These two figures illustrate the setup in the transition zone in the left and in the right plasma. Shown are the perpendicular magnetic field B^z (*blue*), the motional electric field $E^y \times 10^1$ (*red*) and the current sheet $J^y \times 10^2$ (*green*).

The current is carried by ions to guarantee sufficient stability of the current sheet. In our simulation, the two plasmas fully collide after $2w_{\text{grad}}/(v^x_L - v^x_R) \approx 32\,\omega_{pe}^{-1}$ which by our choice of simulation parameters (see Section 4.3) corresponds to only $\approx 1\,\omega_{ce}^{-1}$ but to $\approx 1/50\,\omega_{ci}^{-1}$, i.e., a current carried by electrons would have dissolved before the plasmas collide.

In order to restrain instabilities to arise only from the collision and at the same time avoid Buneman-type instabilities[86], we made tests to ensure that the stability of the current sheet is sufficiently maintained. Therefore, all instabilities observed in our simulation only arise from the collision.

---

[86] Buneman, Physical Review 115 [1959].

Figure 4.7 in compares the stability in particle and field density of a setup with a constant perpendicular magnetic field B^z throughout the simulation box, which has a jumping motional electric field E^y, and the new setup with the transition zone as described above. One can clearly see, that the new setup is very stable over many time steps, whereas the setup with constant magnetic field is not stable. In fact, in the latter setup, one can see a transient in the electric field, which is emitted in the beginning at the strong gradient in the middle of the simulation box, and which eventually perturbs the magnetic field. Note, that this is just a demonstration simulation to demonstrate the stability of the new setup. In a realistic setup the two plasmas are much closer in the beginning, as can be seen in Figure 4.6 and will fully collide at about $31.6\,\omega_{pe}^{-1}$.

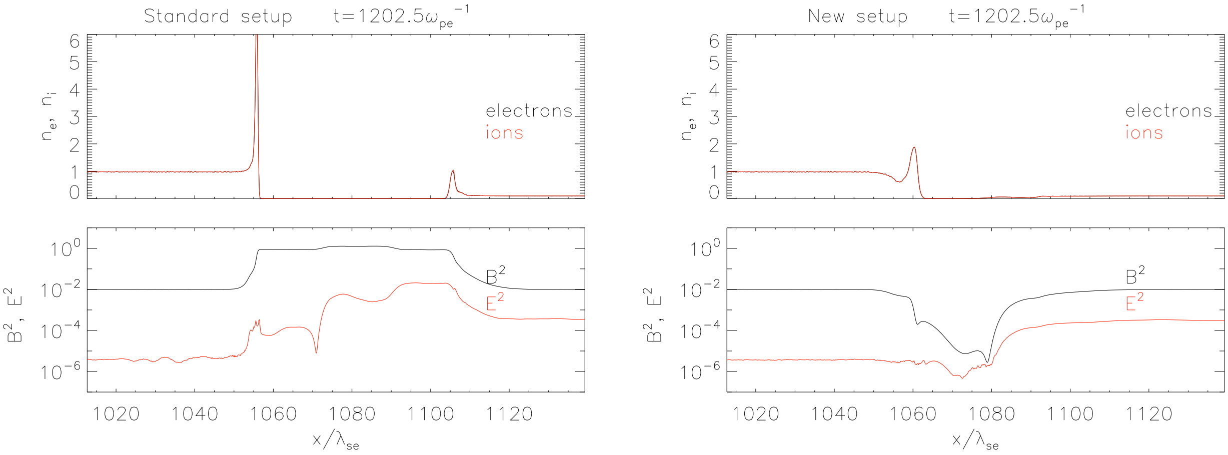

Figure 4.7: This is a stability comparison of a setup with constant perpendicular magnetic field B^z, which has a jumping motional electric field E^y (*left panel*), and the new setup with transition zone (*right panel*) after $1202.5\,\omega_{pe}^{-1}$, just before the collision of the two plasmas. Displayed are the particle density distributions (*top panel*) and the field distributions (*lower panel*). The collision zone is at $x \approx 1063\,\lambda_{se}$ and the edges of the two plasmas started - in this demonstration simulation - at $x = 1012.7\,\lambda_{se}$ and $x = 1519.0\,\lambda_{se}$. The area between the plasmas stays largely free of electromagnetic fields with the new setup until they smoothly collide with each other. In contrast, using the standard method introduces strong transient fields into the same area and leads to a strong field and density compression even before the collision.

For comparison, Murphy et al. (2010) and Murphy/Dieckmann/Drury (2010) use the collision method but without establishing a transition zone in the motional electric field, such that their initial setup exhibits an artificial dipole in the middle of the simulation box. In their results they report the creation of an electromagnetic pulse at the position where the two plasmas encounter each other, which possibly emerged from the initial dipole. In contrast, our simulation avoids the creation of an initial dipole and we also do not observe a pulse in the collision zone.

4.3 Simulation Setup

For ease of comparison, we basically used the same simulation parameters as for simulation run M1 in N2012. All parameters are chosen such that our simulation results may be applied to the environment of a plasma shock formed by supernova ejecta (SNE) penetrating into the interstellar medium (ISM).

The two plasmas are composed of equal numbers of electrons and ions, which are initialised at the same location in order to make the plasmas initially neutral. The plasmas have different densities, and the density ratio is 10. In our simulation frame, which is the centre-of-momentum frame, the *dense* plasma representing the SNE moves to the right with $v_L^x = 0.0354\,c$, while the *tenuous* plasma representing the ISM moves to the left with $v_R^x = -0.354\,c$. The two plasmas collide at a relative speed of $v_{\rm rel} = 0.39\,c$ and form a double-shock structure consisting of a forward shock moving to the right with $v_{S,R}^x = 0.04\,c$, a reverse shock moving to the left with $v_{S,L}^x = -0.09\,c$, and a contact discontinuity (CD) separating the downstream regions of the two shocks. In time, the CD starts also moving in the simulation frame with $v_{\rm CD}^x = -0.06\,c$, which is due to the system being initially in momentum balance but not in ram-pressure balance.

We use ten particles per cell per particle species for both plasma slabs. However, we assign statistical weights to the tenuous plasma particles to establish the intended density ratio between the dense and the tenuous plasma. In such a way, numerical noise is reduced. In order to resolve the characteristic length scales of both electrons and ions in our simulations, we choose a reduced mass ratio of $m_i/m_e = 50$.

The electrons and ions of both plasmas are initially in thermal equilibrium and have a very cold thermal distribution with $v_{e,\rm th} = \sqrt{k_B T_0/m_e} = 0.002\,c$. In the current study, we only consider a magnetised plasma in which the initial homogeneous magnetic field is aligned perpendicular to the plasma flow. In order to not miss any important processes in either dimension, we chose the magnetic field such that it has equally large components in y- and z-direction, i.e., $\boldsymbol{B} = B_0(0, 1/\sqrt{2}, 1/\sqrt{2})$. The strength of the magnetic field can be given by the ratio of the electron cyclotron frequency $\omega_{ce} = eB_0/m_e$ to the electron plasma frequency of the dense plasma $\omega_{pe,L} = \sqrt{n_{e,L}e^2/\epsilon_0 m_e}$, where $n_{e,L}$ is the electron density of the dense plasma and ϵ_0 is the vacuum permittivity. This value amounts to $\omega_{ce}/\omega_{pe,L} = 0.032$.

In order to save valuable computational resources and on account of the slower shock-forming processes in non-relativistic plasma flows, our simulations were performed using a 2D3V model, i.e., we restrict all particles to two spatial dimensions while keeping all three components of their velocities. Since the magnetic field bends the particle trajectories out of the simulation plane, particles have three degrees of freedom, and the non-relativistic adiabatic index is $\Gamma = 5/3$. Given the magnetic field strength, the Alfvén speed $v_A = B_0/\sqrt{\mu_0(n_e m_e + n_i m_i)}$ for the tenuous and the dense plasma can be calculated as $v_{A,R} = 1.4 \times 10^{-2}\,c$ and $v_{A,L} = 4.5 \times 10^{-3}\,c$. In the upstream rest frames of the tenuous and the dense plasma the speed of the forward and reverse shock can be measured to $v'_{S,R} \approx 0.39\,c$ and $v'_{S,L} \approx -0.13\,c$, respectively. Thus, the Alfvénic Mach number $M_A = v'_S/v_A$ of the forward shock is $M_{A,R} = 27.8$ and that of the reverse shock is $M_{A,L} = 28.4$.

Although the Alfvénic Mach number of the resulting shocks is quite similar, the sonic Mach number is different. The latter can be calculated as $M_s = v'_S/c_s$, where $c_s = \sqrt{2\Gamma k_B T_0/m_i}$ is the sound speed. Given $c_s \approx 5 \times 10^{-4}\,c$, we can calculate the sonic Mach numbers of the forward and the reverse shock to $M_{s,R} = 755.2$ and $M_{s,L} = 251.7$, respectively, which are numbers typical for SNRs. However, the Mach numbers of our two shocks are only observed in SNRs if there is strong magnetic-field amplification in the upstream region[87]. Otherwise, the sonic and Alfvénic Mach numbers would be much more similar.

---

[87] Drury/Downes, Monthly Notices of the Royal Astronomical Society 427 [2012].

The spatial dimensions in our simulation and all figures are given in terms of the electron skin length of the dense plasma $\lambda_{se} \equiv \lambda_{se,L} = c/\omega_{pe,L} = 7.9\,\Delta$, where Δ is the size of the grid cells. The temporal dimensions are given in terms of the inverse of the electron plasma frequency of the dense plasma $\omega_{pe}^{-1} \equiv \omega_{pe,L}^{-1} = 15.8\,\Delta t$, where Δt is the time step. Given a mass ratio of 50, the corresponding values for the ions are $\lambda_{si,L} = c/\omega_{pi,L} = 55.9\,\Delta$ and $\omega_{pi,L}^{-1} = 111.8\,\Delta t$. The corresponding parameter values for the tenuous plasma are $\lambda_{se,R} = 25\,\Delta$, $\omega_{pe,R}^{-1} = 50\,\Delta t$, $\lambda_{si,R} = 176.8\,\Delta$, $\omega_{pi,R}^{-1} = 353.6\,\Delta t$. For completeness, we also give the values for the inverse cyclotron frequencies as $\omega_{ce}^{-1} = 500\,\Delta t$ for the electrons and $\omega_{ci}^{-1} = 25000\,\Delta t$ for the ions.

The simulation discussed in this paper was performed on a numerical grid with a size of $L_x \times L_y = 18987.4 \times 324.1\,\lambda_{se}^2 = 2683.4 \times 45.8\,\lambda_{si}^2$ with radiating boundary conditions in x-direction and periodic boundary conditions in y-direction. A number of initial tests have been run in order to find the right size for the simulation box. The simulation time was $T = 31645.5\,\omega_{pe}^{-1} = 4472.3\,\omega_{pi}^{-1} = 1000\,\omega_{ce}^{-1} = 20\,\omega_{ci}^{-1}$, which is $2554\,\omega_{pe}^{-1} = 361\,\omega_{pi}^{-1}$ or 8 % longer than our simulation for the parallel shock (see N2012). Compared to the simulations done by Kato/Takabe (2010) and Guo/Sironi/Narayan (2014), this is also a factor 4 and 2 longer, respectively.

The simulation was performed with a modified version of the TRISTAN code[88], which was adapted to work in 2D3V and parallelised using MPI[89]. Other modifications we introduced include a fourth-order finite-difference time-domain (FDTD) field-pusher with a weak Friedman filter[90] that efficiently filters numerical Cerenkov radiation, and a new particle pusher proposed in Vay (2008) that achieves better energy conservation and less numerical self-heating.

In order to make efficient use of the computational resources, our simulation starts with a much smaller size in x-direction and is allowed to grow along with the continuous increase of occupied volume by the interpenetrating plasma flows. The number of domains in y-direction stays constant, while new domains are added in x-direction once the simulated plasma approaches the boundary of the simulation box.

Using a so-called moving injector, particles are continuously injected in a small injection layer at the outer edges of the two plasma slabs. The injection layer retreats from the collision zone as far as necessary in order to preserve all particles and fields within the collision zone, but it stays as close as possible such that newly injected particles do not have to travel too long a distance without any interaction, which further helps to avoid numerical Cerenkov radiation and unnecessary computational expense.

---

[88] Buneman, Computer Space Plasma Physics.

[89] Niemiec et al., The Astrophysical Journal 684 [2008].

[90] Greenwood et al., Journal of Computational Physics 201 [2004]; Friedman et al., Damped time advance methods for particles and EM fields

4.4 Simulation Results

4.4.1 Early-stage Evolution

Contact Discontinuity Formation

Since our simulation starts with two separated plasma slabs, a shock has yet to form. Once the two plasmas start to interpenetrate each other, Weibel-like instabilities lead to current filamentation. In turn, these instabilities lead to an amplification of the ambient magnetic field, which has a strong influence on the motion of the plasma particles. The electron component in both streams is rapidly decelerated and strongly confined to the collision region. Once trapped within the collision region, the electron populations commence heating. Due to their larger rigidity, the ions are able to penetrate deeper into the counter-streaming plasma, but only up to roughly one gyro radius. Note that the latter is ten times larger for the tenuous-plasma ions, since their bulk speed in the centre-of-momentum frame is ten times larger than the speed of the dense-plasma ions.

At about $t \approx 1000\,\omega_{pe}^{-1} \approx 140\,\omega_{pi}^{-1} \approx 32\,\omega_{ce}^{-1} \approx 0.6\,\omega_{ci}^{-1}$ the magnetic turbulence emerging from the collision zone has reached sufficient strength to prevent newly incoming particles to cross into the counter-streaming plasma, and a contact discontinuity (CD) is formed. This stage is shown in Figure 4.8. The CD is located at around $x \approx 5670\,\lambda_{se}$, which is approximately the location where the two plasma streams first encountered each other. Already in Figure 4.8(a), which shows the particle density profiles of all four particle species averaged over the y-direction, it becomes apparent that the newly formed CD allows no electrons to pass. They are efficiently stopped at the CD and start to pile up in the collision zone. This can be also seen in Figures 4.8(d) and 4.8(f), which show the particle density distributions of the dense-plasma and tenuous-plasma electrons, respectively. The phase-space plot for the electrons in Figure 4.8(h) demonstrates the heating mentioned earlier, where one can see a broadening of the phase-space distribution of the electron beams behind the CD.

Nearly the same is true for the ions. The only difference here is that a certain fraction of both ion populations is able to cross into the counter-streaming plasma before the CD is fully formed. These fractions form a separate population on the far side of the CD. They are rapidly decelerated by the incoming plasma stream and are reflected back towards the collision zone, where they encounter the now fully formed CD. Since these ions have no means to either pass through the CD or to escape the continuous inflow of plasma particles, they are trapped near the CD and will eventually become part of the downstream population of the forward and reverse shock, respectively. These populations are visible as tails in the density profiles in Figure 4.8(a). In the ion phase-space plot in Figure 4.8(i), the tenuous-plasma ions that have crossed into the counter-streaming dense plasma are visible as a long tail to the left of the CD at $v^x \approx -0.25\,c$, whereas the reflected tenuous-plasma ions can be seen to the right of the CD at $v^x \approx 0.25\,c$. Due to their ten times smaller initial speed, the penetration depth of the dense-plasma ions into the counter-streaming tenuous plasma is ten times smaller than that of the tenuous-plasma ions. They are visible to the right of the CD at $v^x \approx 0.05\,c$, whereas the reflected dense-plasma ions are obscured in Figure 4.8(i) by the tenuous-plasma ions penetrating into the dense plasma.

Compared to our results for the parallel shock (see N2012) with the CD of the parallel shock forming around $t \approx 400\,\omega_{pi}^{-1} \approx 2830\,\omega_{pe}^{-1}$, the perpendicular shock reaches this stage in nearly a third of this time. Moreover, the perpendicular shock efficiently decelerates all particles on encounter with the counter-streaming plasma and confines them to the collision region already at this early stage of the simulation. Eventually, this will lead to much weaker instabilities in the upstream regions of the two shocks. In fact, the upstream regions of the two shocks will be nearly devoid of large-scale instabilities as will be demonstrated later.

From the profile of the average magnetic field in Figure 4.8(b), one can observe that the amplification of the magnetic field for the perpendicular shock is about one order of magnitude larger compared to the parallel shock already at this early stage of the simulation (compare Figure 5 in N2012) on account of the much stronger particle confinement to the collision region. Moreover, due to the absence of large-scale turbulence in the perpendicular shock, the contact discontinuity emerges far clearer from the surrounding magnetic field and is visible as a sharp peak in the field profile.

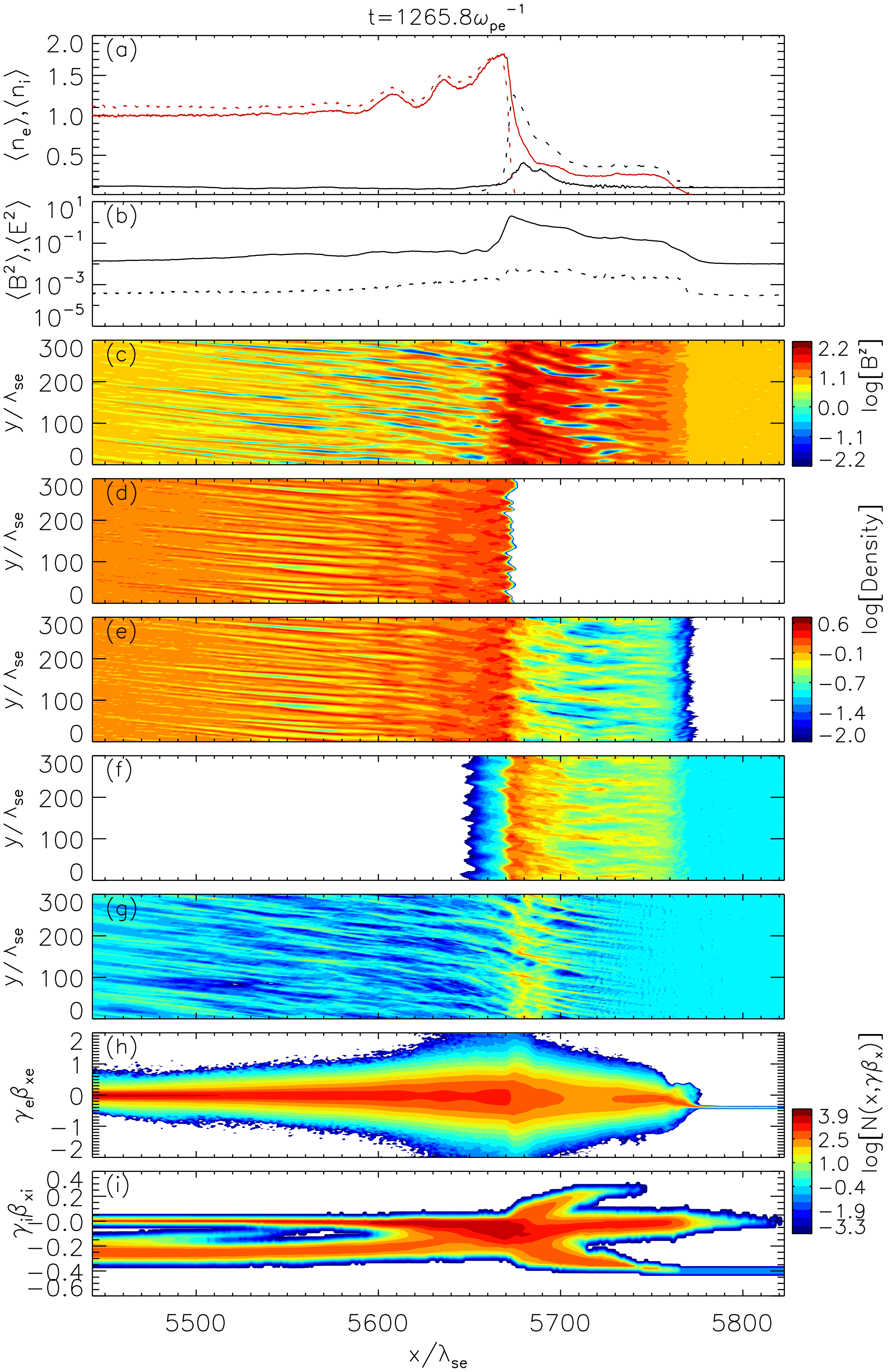

Figure 4.8: Structure of the plasma-collision region at time $t = 1265.8\,\omega_{pe}^{-1}$. Displayed are the profiles of (a) the average particle-number density normalised to the far-upstream density of the dense plasma (red lines: dense plasma, black lines: tenuous plasma; solid lines: ions, dotted lines: electrons), (b) profiles of the average magnetic (solid line) and electric (dotted line) energy density in simulation units, (c) the amplitude of the magnetic field B^z (in sign-preserving logarithmic scale as $\mathrm{sgn}(B^z)\,(2 + \log\left[\max(10^{-2}, |B^z|)\right])$), the density of dense-plasma electrons (d), dense-plasma ions (e), tenuous-plasma electrons (f), and tenuous-plasma ions (g), all normalised to the far-upstream density of the dense plasma, and the longitudinal phase-space distribution of electrons (h) and ions (i).

Double-shock Structure Formation

The continuous inflow of plasma particles towards the CD and the inability of the particles to cross it causes the creation of shocks on both sides of the CD. Since the tenuous plasma coming from the right side of our simulation box represents the interstellar medium (ISM) and the dense plasma coming from the left represents the supernova ejecta (SNE), we designate the right shock as the forward shock and the left shock as the reverse shock.

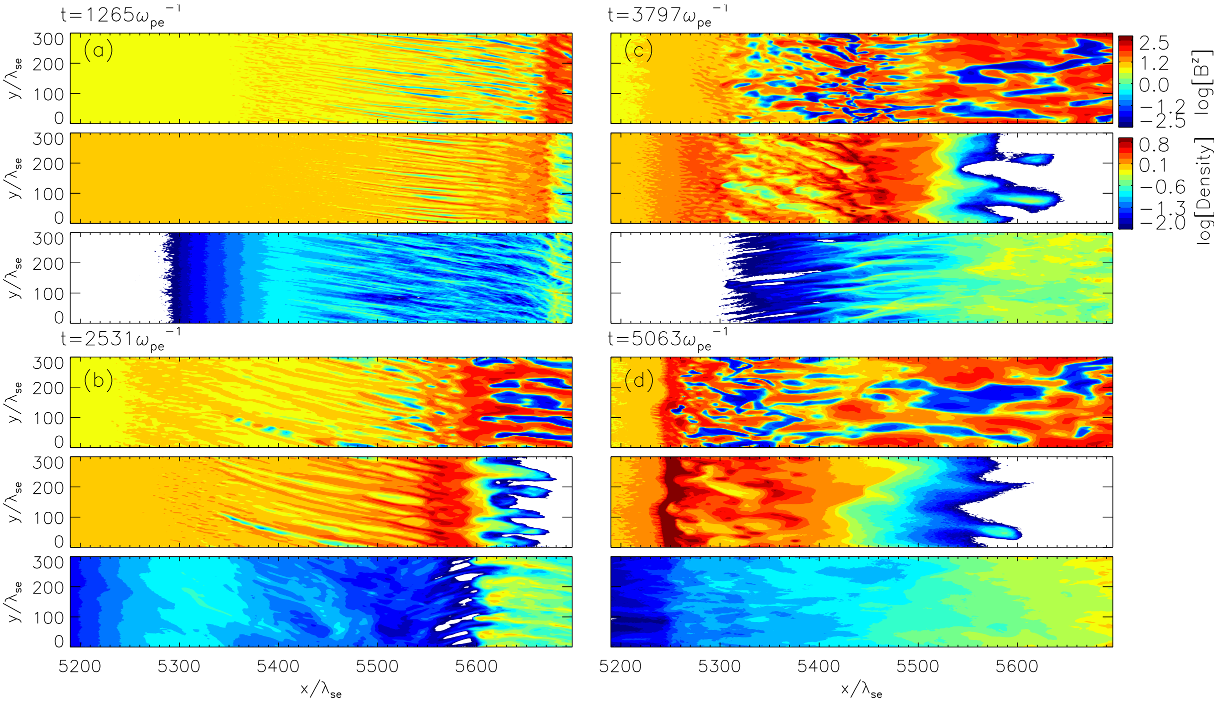

Figure 4.9: Snapshots of the nonlinear evolution of the filamentation-like instability in the dense-plasma region in the vicinity of the contact discontinuity at times (a) $t = 1265$, (b) 2531, (c) 3787, and (d) $5063\,\omega_{pe}^{-1}$. From top to bottom, each panel shows the amplitude of the magnetic field B^z (in sign-preserving logarithmic scale; see Figure 4.8(c)), the density of dense-plasma ions, and the density of tenuous-plasma ions, both normalised to the far-upstream density of the dense plasma.

The stages leading to the development of the reverse shock are displayed in Figure 4.9 as a sequence of snapshots that show the magnetic field component B^z and the density distributions of dense-plasma and tenuous-plasma ions at $t = 1265\,\omega_{pe}^{-1}$, $2531\,\omega_{pe}^{-1}$, $3787\,\omega_{pe}^{-1}$, and $5063\,\omega_{pe}^{-1}$. The distribution of dense-plasma and tenuous-plasma electrons closely follows that of the ions. A remarkable exception are the ion populations that were able to cross into the counter-streaming plasma prior to the full formation of the CD. They are visible as green wisps of low density in the density distributions in Figure 4.9.

Following the movement of the tenuous-plasma ions through the subsequent panels, we can see that this particular population detaches itself from the main population in panel (b) where the CD is located at $x \approx 5600\,\lambda_{se}$. However, they are decelerated by the incoming plasma stream and are pushed back towards the CD which has now reached a position at $x \approx 5550\,\lambda_{se}$ as can be seen in panel (c). On encounter with the CD, the ions are reflected back into the dense plasma, which can be seen in panel (d). At this stage, the reverse shock has formed at $x \approx 5240\,\lambda_{se}$ and the reflected ions are trapped between the shock and the CD at $x \approx 5500\,\lambda_{se}$ and become part of the downstream region of the reverse shock. The same process happens on the other side of the CD for the dense-plasma ions, but on smaller length scales.

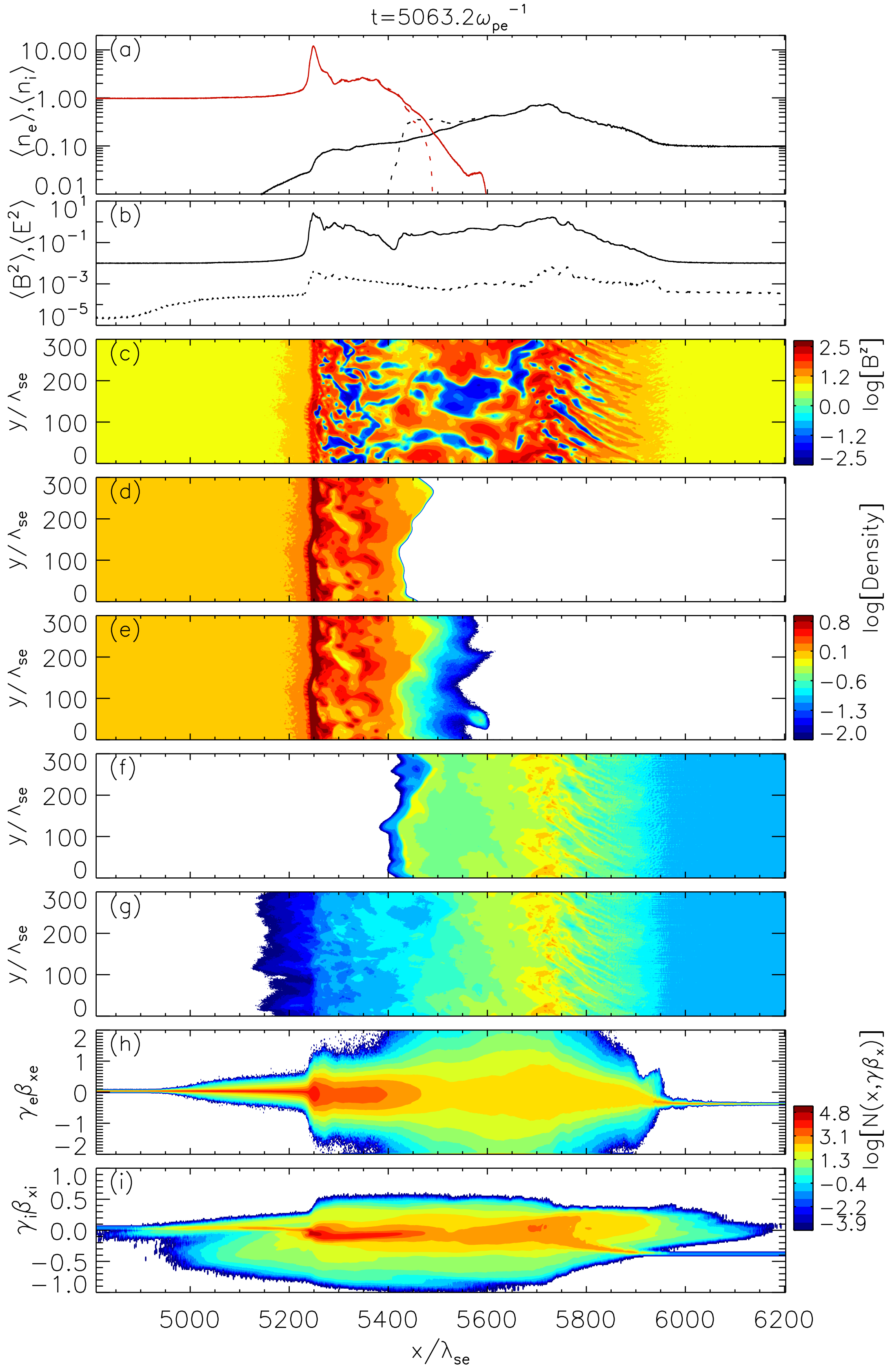

Figure 4.10: Structure of the plasma-collision region at time $t = 5063.2\,\omega_{pe}^{-1}$. Displayed are the profiles of (a) the average particle-number density normalised to the far-upstream density of the dense plasma (red lines: dense plasma, black lines: tenuous plasma; solid lines: ions, dotted lines: electrons), (b) profiles of the average magnetic (solid line) and electric (dotted line) energy density in simulation units, (c) the amplitude of the magnetic field B^z (in sign-preserving logarithmic scale as $\mathrm{sgn}(B^z)\,(2+\log\left[\max(10^{-2},|B^z|)\right])$), the density of dense-plasma electrons (d), dense-plasma ions (e), tenuous-plasma electrons (f), and tenuous-plasma ions (g), all normalised to the far-upstream density of the dense plasma, and the longitudinal phase-space distribution of electrons (h) and ions (i). Note, that a logarithmic scale is used for the density profiles in panel (a).

The original Weibel-like instabilities visible in Figure 4.9(a) are quickly dissolved by the particles of the dense plasma that are reflected at the CD. Once sufficient density in the reflected particles is accumulated, the shock emerges. Strong turbulence in the magnetic field now dominates the downstream region of the reverse shock. Again, the same happens for the forward shock. The double-shock structure consisting of forward shock, reverse shock and CD has fully formed at about $t \approx 5000\,\omega_{pe}^{-1} \approx 700\,\omega_{pi}^{-1} \approx 158\,\omega_{ce}^{-1} \approx 3\,\omega_{ci}^{-1}$. This stage is shown in Figure 4.10. The forward shock, reverse shock and CD are located at around $x \approx 5760\,\lambda_{se}$, $x \approx 5250\,\lambda_{se}$ and $x \approx 5440\,\lambda_{se}$, respectively.

Note, that the CD has moved about $230\,\lambda_{se}$ during ≈ 3800 inverse plasma times since the last simulation snapshot displayed in Figure 4.8. Thus, the CD moves with the predicted speed of $v^x_{\mathrm{CD}} = -0.06\,c$ already at this early stage of the simulation.

Comparing the two snapshots in Figures 4.8 and 4.10, one immediately notices the nearly total disappearance of the shock precursor in the upstream region of the reverse shock. In the upstream region of the forward shock, the formerly transverse filaments are replaced by oblique structures in the immediate vicinity of the shock, which can be seen in Figures 4.10(c), (f) and (g), and which will be discussed in more detail in Section 4.4.2. Due to the strong confinement of all particles to the collision region, the upstream regions of both shocks are devoid of any instabilities. This development is consistent with the results published by Kato/Takabe (2010) and Caprioli/Spitkovsky (2014).

The two proto-shocks are most prominently visible as strong peaks in the density profiles (Figure 4.10(a)). We can also see an initial density overshoot, i.e., the density compression at the shock front temporarily surpasses the expected magnetohydrodynamic compression level of $n_d/n_u = 4$, with n_d and n_u being the particle density downstream and upstream of the shock, respectively. The density compression at forward and reverse shock peak at $n_{R,d}/n_{R,u} \approx 8$ and $n_{L,d}/n_{L,u} \approx 14$, respectively. These strong density amplifications are also visible in the density distribution plots (Figures 4.10(d), (e), (f) and (g)), whereas comparable features were not observed in our simulations of parallel shocks (see Figure 8 in N2012). In the latter case, the shock developed more gradually with density amplifications growing steadily over the whole simulation time. In the perpendicular shock case, we have a proto-shock established already at a very early stage of the simulation.

The phase-space plot for the electrons (Figure 4.10(h)) indicates that heating takes place in the whole collision region. In the phase-space plots for the ions (Figure 4.10(i)), we can now see populations of reflected ions on both sides of the shock. Note that the dense-plasma ions only constitute a minor fraction of these populations and are visible at the very left end of panel (i) at $v^x \approx -0.1\,c$. The major fraction of reflected ions is constituted by tenuous-plasma ions being either reflected at the CD back into the incoming tenuous plasma, which cause the creation of the forward shock, or on the far side of the CD into the incoming dense plasma, which contribute to creating the reverse shock.

4.4.2 Late-stage Evolution

We let our perpendicular shock simulation run for $31645.5\,\omega_{pe}^{-1} = 4472.3\,\omega_{pi}^{-1} = 1000\,\omega_{ce}^{-1} = 20\,\omega_{ci}^{-1}$. The structure of the shock at the end of the simulation is presented in Figure 4.11. At this stage of the simulation we have a very clear separation of the particles into forward and reverse shock. The shocks are located at around $x \approx 6800\,\lambda_{se}$ (forward shock) and $x \approx 2800\,\lambda_{se}$ (reverse shock). The shock speeds measured in the simulation frame are consistent with the theoretical steady-state values of $v_{S,R}^{x} = 0.04\,c$ for the forward shock and $v_{S,L}^{x} = -0.09\,c$ for the reverse shock. The CD has reached a position at $x \approx 3850\,\lambda_{se}$, which is again consistent with the predicted speed of $v_{\mathrm{CD}}^{x} = -0.06\,c$.

Looking at the density profiles in Figure 4.11(a), it becomes apparent that the compression ratio at the shocks is very well in agreement with the magnetohydrodynamical jump conditions for non-relativistic gas with $\Gamma = 5/3$, which predict $n_{R,d}/n_{R,u} = 3.86$ and $n_{L,d}/n_{L,u} = 4.02$ in the simulation frame for the forward and reverse shocks, respectively (upper and lower dashed lines in Figure 4.11(a)). The compressed regions extend over a large area in the downstream region of the two shocks. Compared to the results of our parallel shock simulation, these regions have nearly twice the size for the perpendicular case, namely $\approx 3000\,\lambda_{se} = 424\,\lambda_{si}$ for the forward shock and $\approx 1000\,\lambda_{se} = 141\,\lambda_{si}$ for the reverse shock. The factor three between the sizes of the compressed regions corresponds to the same factor in the shock speeds in the CD frame (see Section 4.3).

More characteristics of the system are discussed in the following sections. In sections 4.4.2 and 4.4.2, we elaborate on features visible at the forward and the reverse shock, respectively. In section 4.4.2 we take a closer look at the structure of the CD.

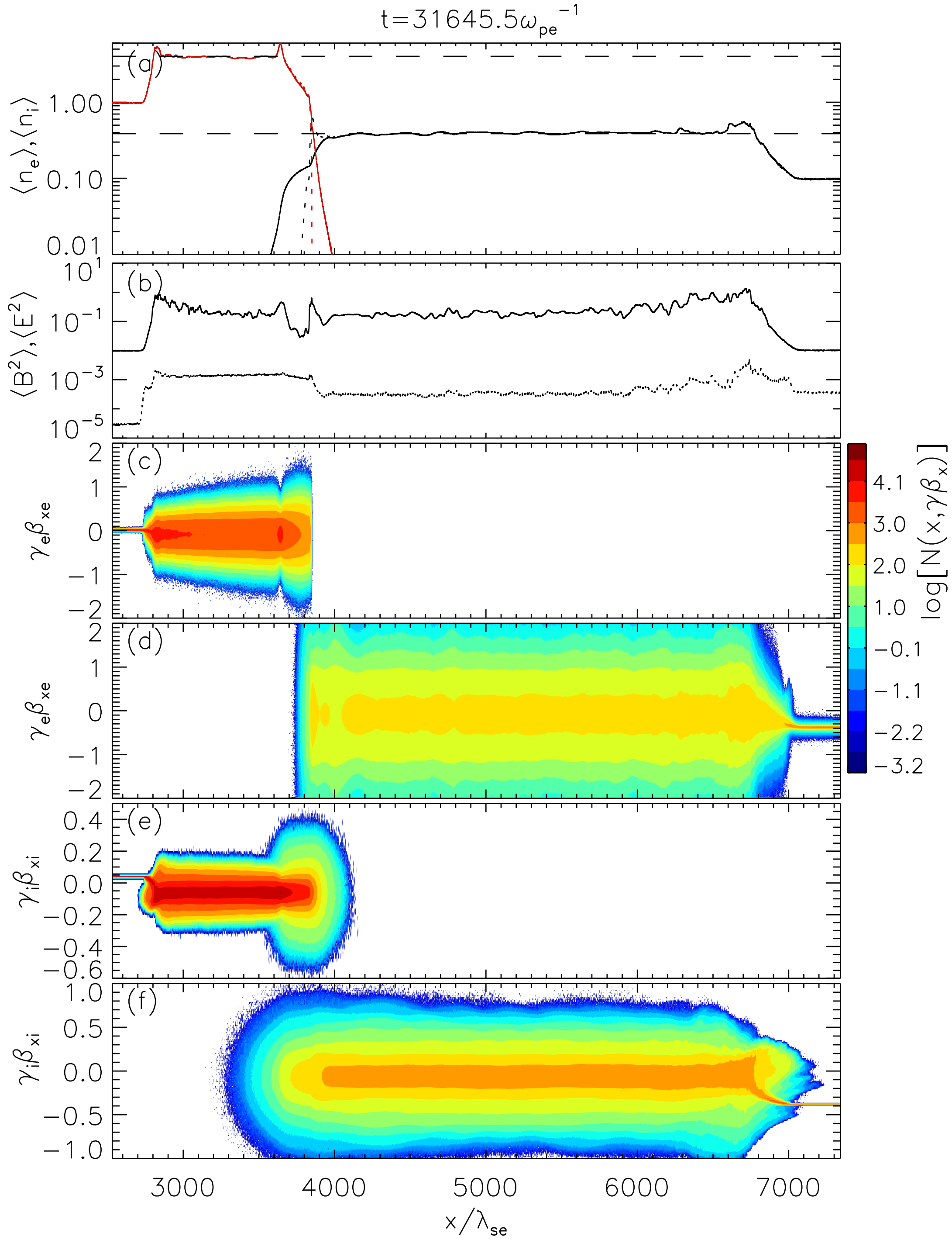

Figure 4.11: Structure of the collision region at the end of the simulation at time $t = 31645.5\,\omega_{pe}^{-1}$. Shown are the profiles of (a) the average particle-number density (a logarithmic scale is used), (b) the average magnetic and electric energy density (see Figures 4.8(a) and (b)), and the longitudinal phase-space distributions separately for all particle species: electrons of the dense (c) and tenuous (d) plasma and ions of the dense (e) and tenuous (f) component. In panel (a), the horizontal dashed lines mark the magnetohydrodynamic compression level of $n_{R,d}/n_{R,u} = 3.86$ for the forward shock (lower line) and $n_{L,d}/n_{L,u} = 4.02$ for the reverse shock (upper line).

Structure of the Forward Shock Transition

Figures 4.12 and 4.13 present the structure of the forward shock transition at the end of the simulation at time $t = 31645.5\,\omega_{pe}^{-1}$. Displayed in Figure 4.12 are the density distribution of the tenuous-plasma ions, the amplitude of the electric field component E^x and the amplitude of the magnetic field component B^z with correct aspect ratio. The distribution of the tenuous-plasma electrons (not shown) closely follows that of the tenuous-plasma ions. The distribution of B^y (not shown) also closely follows that of B^z. The downstream structures visible in E^x can also be found in similar form in E^y and E^z (not shown). Figure 4.13 presents a magnified version of Figure 4.11 showing the density and field profiles of the forward-shock transition and the phase-space distribution of only tenuous-plasma electrons and ions in y- and z-direction.

At first glance, one can see a clear transition from weak large-scale turbulence deep inside the downstream region of the shock towards strong small-scale turbulence near the shock front. The shock front appears as a clearly visible density amplification between $x = 6700\,\lambda_{se}$ and $x = 6800\,\lambda_{se}$, which is peaking at a compression ratio of ≈ 5.8, i.e., it shows a density enhancement of about 45 %. We can also observe an overshoot between $x = 6600\,\lambda_{se}$ and $x = 6700\,\lambda_{se}$ and a shock ramp between $x = 6800\,\lambda_{se}$ and $x = 7000\,\lambda_{se}$. The entire ramp, which has an extent of ≈ 60 local skin lengths, is filled with small-scale filamentary structures. Another significant feature is the nearly total absence of a shock precursor. These characteristics are in stark contrast to our results from the parallel shock (see Figure 10 in N2012), where we observed strong turbulence over the whole shock with variations only in size and orientation and a very extended precursor.

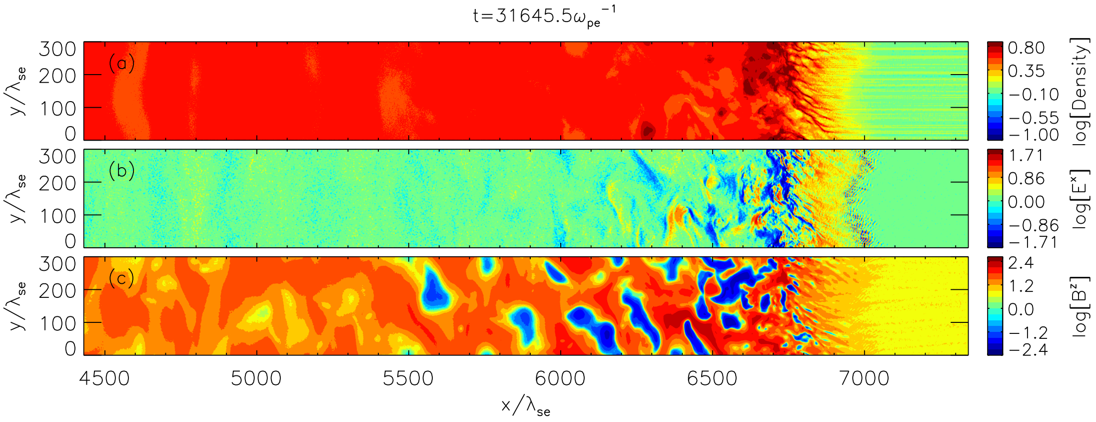

Figure 4.12: Structure of the forward-shock transition at the end of the simulation at time $t = 31645.5\,\omega_{pe}^{-1}$. Shown is (a) the density distribution of the tenuous-plasma ions normalised to the far-upstream density of the tenuous plasma, (b) the amplitude of the electric field E^x (in sign-preserving logarithmic scale as $\mathrm{sgn}(E^x)\,\left(2 + \log\left[\max(10^{-2}, |E^x|)\right]\right)$) and (c) the amplitude of the magnetic field B^z (in sign-preserving logarithmic scale as $\mathrm{sgn}(B^z)\,(2 + \log\left[\max(10^{-2}, |B^z|)\right])$).

Similar filamentary structures like the ones we observe in the shock ramp were also seen in Kato/Takabe (2010) and Murphy et al. (2010) and identified as current filaments. A linear analysis suggests that these structures are caused by an ion-beam Weibel instability that has a mode parallel to the ambient magnetic field. We can observe this mode in the upstream Fourier spectrum in Figure 4.14(c) at $k_\perp \lambda_{se} \approx 0.2$.

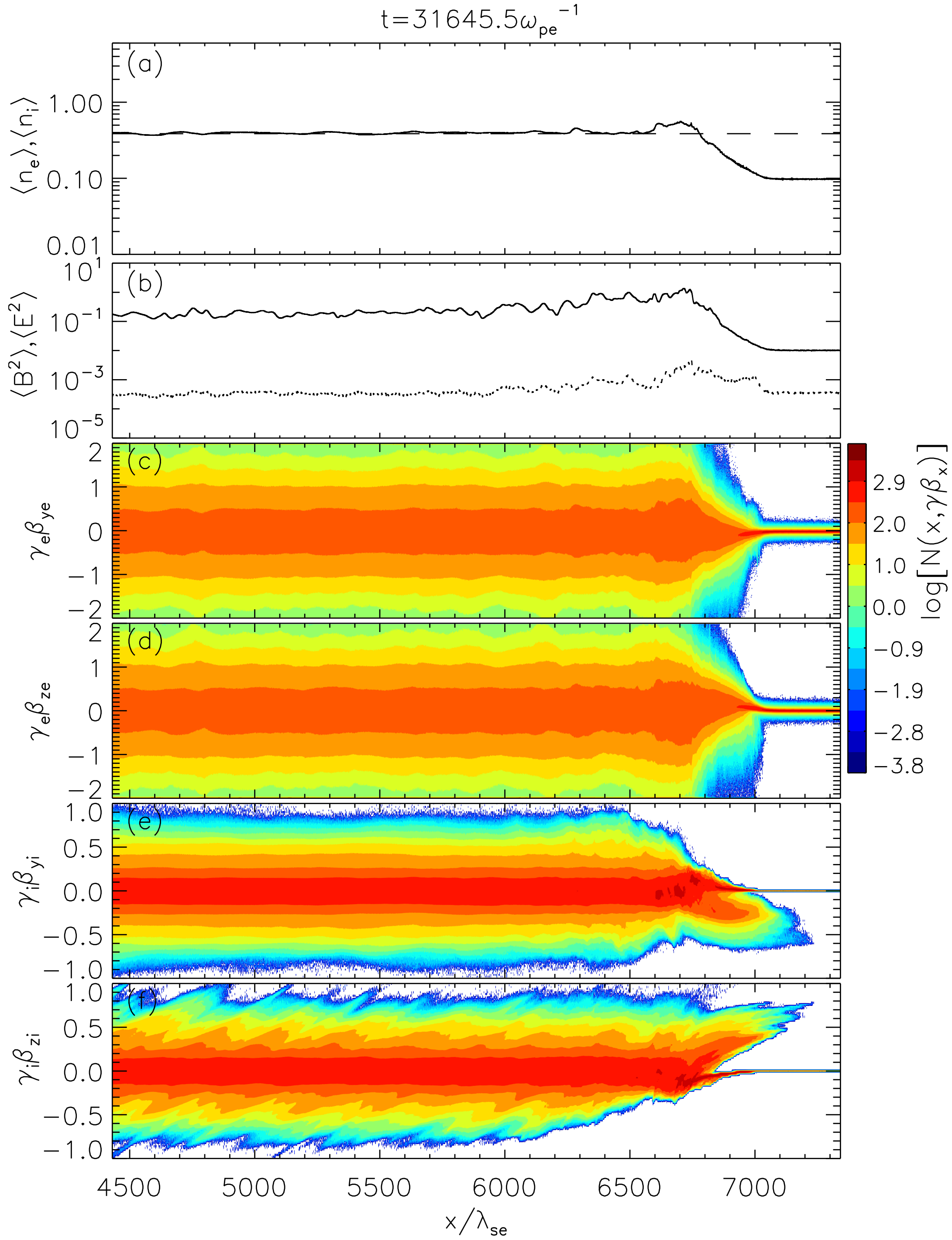

Figure 4.13: Structure of the forward-shock transition at the end of the simulation at time $t = 31645.5\,\omega_{pe}^{-1}$. Shown are the profiles of (a) the average particle-number density (a logarithmic scale is used), (b) the average magnetic and electric energy density (see Figures 4.8(a) and (b)), and the transversal phase-space distributions separately for the tenuous-plasma particles: p^y (c) and p^z (d) for tenuous-plasma electrons and p^y (e) and p^z (f) for tenuous-plasma ions. In panel (a), the horizontal dashed line marks the magnetohydrodynamic compression level of $n_{R,d}/n_{R,u} = 3.86$ for the forward shock.

The transition from large-scale to small-scale turbulence on the approach to the shock front from far downstream discussed above can also be seen in Figure 4.14, which shows Fourier spectra of the magnetic field component B^z in slices of width $400\,\lambda_{se}$ at three different locations, namely in the downstream region at $x = 5700\,\lambda_{se}$, at the shock at $x = 6600\,\lambda_{se}$ and in the upstream region at $x = 7300\,\lambda_{se}$. Between the downstream spectrum in Figure 4.14(a) and the shock spectrum in Figure 4.14(b) we can see a clear shift from low wave number to higher wave number, i.e. from large wavelength to smaller wavelength. In the downstream region and at the shock, we observe isotropic wave modes with wave numbers at the resolution maximum. The upstream spectrum in Figure 4.14(c) shows that the upstream region is indeed free of large-scale turbulence and we can observe only oblique filamentation modes of moderate amplitude.

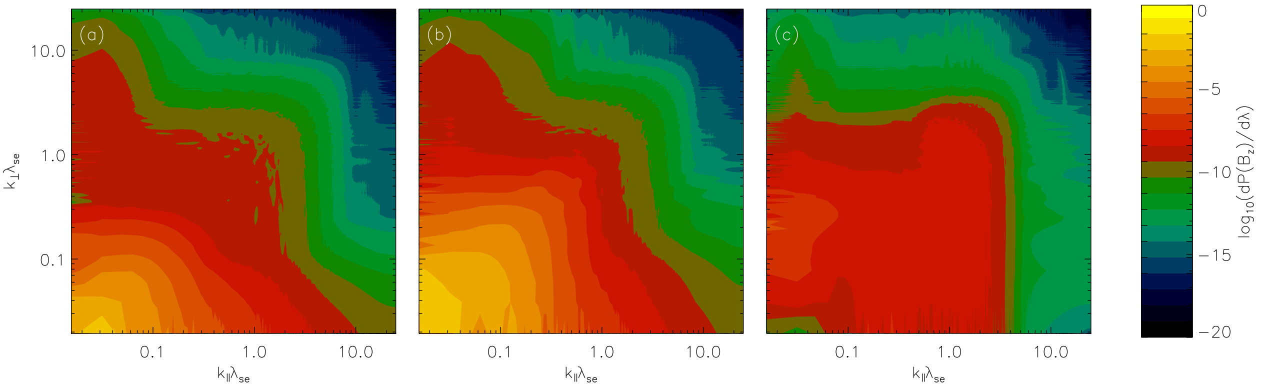

Figure 4.14: Fourier power spectra $[\log_{10}(\mathrm{d}P/\mathrm{d}\lambda)]$ of the perpendicular magnetic-field component B^z at time $t = 31645.5\,\omega_{pe}^{-1}$ at $x = 5500 - 5900\,\lambda_{se}$ (a), $x = 6400 - 6800\,\lambda_{se}$ (b) and $x = 7100 - 7500\,\lambda_{se}$ (c) in two-dimensional reduced wavevector space $\left(Z_{\parallel}, Z_{\perp}\right) = \left(k_{\parallel}\lambda_{se}, k_{\perp}\lambda_{se}\right)$.

Similar shock structures and a transition in the magnetic turbulence scales in shock downstream were also observed by, e.g., Burgess/Scholer (2007), Amano/Hoshino (2009), Kato/Takabe (2010), Caprioli/Spitkovsky (2014) and Guo/Sironi/Narayan (2014). They also note the absence of strong turbulence in the upstream region.

The density enhancements at the shock front are accompanied by a bipolar electrostatic field that is visible in Figure 4.12(b), which captures ions and electrons inside the shock front and forces them to gyrate around the upstream magnetic field and to drift parallel to the motional electric field. This is most prominently visible in the phase-space distribution of the tenuous-plasma ions in Figures 4.13(e) and (f). The phase-space distributions of the tenuous-plasma electrons show a noticeable broadening between $x = 6600\,\lambda_{se}$ and $x = 6800\,\lambda_{se}$, i.e., exactly at the position of the forward shock. These effects are typical indicators for the shock surfing acceleration (SSA) mechanism, as studied in detail by, e.g., Leroy et al. (1981), Wu et al. (1984), Hoshino (2001) Amano/Hoshino (2007) and Amano/Hoshino (2009).

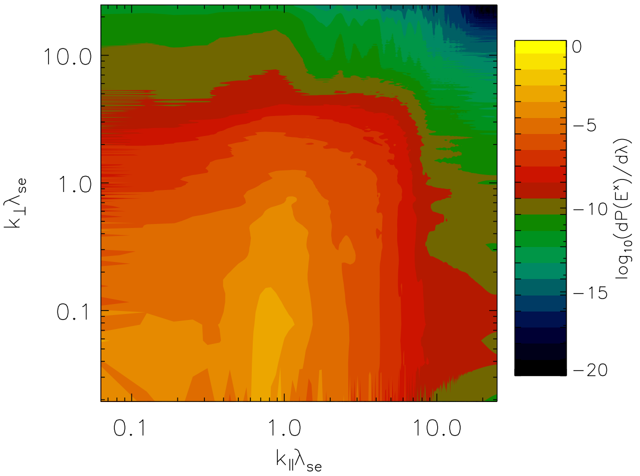

Figure 4.15: Fourier power spectra $[\log_{10}(\mathrm{d}P/\mathrm{d}\lambda)]$ of the electric-field component E^x at time $t = 31645.5\,\omega_{pe}^{-1}$ at $x = 6950 - 7050\,\lambda_{se}$ in two-dimensional reduced wavevector space $\left(Z_\parallel, Z_\perp\right) = \left(k_\parallel \lambda_{se}, k_\perp \lambda_{se}\right)$.

In Figures 4.12(b) and 4.13(b), a small amplification of the electric field in the shock foot at $x \approx 7000\,\lambda_{se}$ reveals another effect. The magnetic field gradient at the shock front operates as a magnetic mirror that reflects ions in $+x$-direction into the upstream plasma (see Figure 4.11(f)). The ions drift along the shock front in $-y$- and $+z$-direction parallel to the motional electric field, as can be seen in Figures 4.13(e) and (f), and thereby gain energy. The reflected ions excite the Buneman instability and thereby cause the structures visible in the electric field in the shock foot[91]. We can observe the Buneman instability in the upstream Fourier spectrum in Figure 4.15 at $k_\parallel \lambda_{se} \approx 0.8$, which corresponds to $k_\parallel \lambda_{se,\mathrm{loc}} \approx 2.4$, where $\lambda_{se,\mathrm{loc}}$ is the local electron skin length. Due to their smaller gyro radius, the electrons are re-thermalised and pre-heated once they encounter the shock precursor as can be seen in Figures 4.13(c) and (d). These effects are typical indicators for the shock drift acceleration (SDA). A detailed theoretical description of this process can be found in, e.g., Amano/Hoshino (2007), Amano/Hoshino (2010) and Guo/Sironi/Narayan (2014).

Another feature of the ion phase-space distribution is the somewhat oblique alignment of the component p^z visible in Figure 4.13. This effect, which was also observed by Guo/Sironi/Narayan (2014), might be due to the 2D3V nature of our simulation.

---

[91] Amano/Hoshino, The Astrophysical Journal 690 [2009].

Structure of the Reverse Shock Transition

Figures 4.16 and 4.17 present the structure of the reverse shock transition at the end of the simulation at time $t = 31645.5\,\omega_{pe}^{-1}$. Displayed in Figure 4.16 are the density distribution of the dense-plasma ions, the amplitude of the electric field component E^x and the amplitude of the magnetic field component B^z with correct aspect ratio. The distribution of the dense-plasma electrons (not shown) closely follows that of the dense-plasma ions. The distribution of B^y (not shown) also closely follows that of B^z. The downstream structures visible in E^x can also be found in similar form in E^y and E^z (not shown). Figure 4.17 presents a magnified version of Figure 4.11 showing the density and field profiles of the reverse-shock transition and the phase-space distribution of only dense-plasma electrons and ions in y- and z-direction.

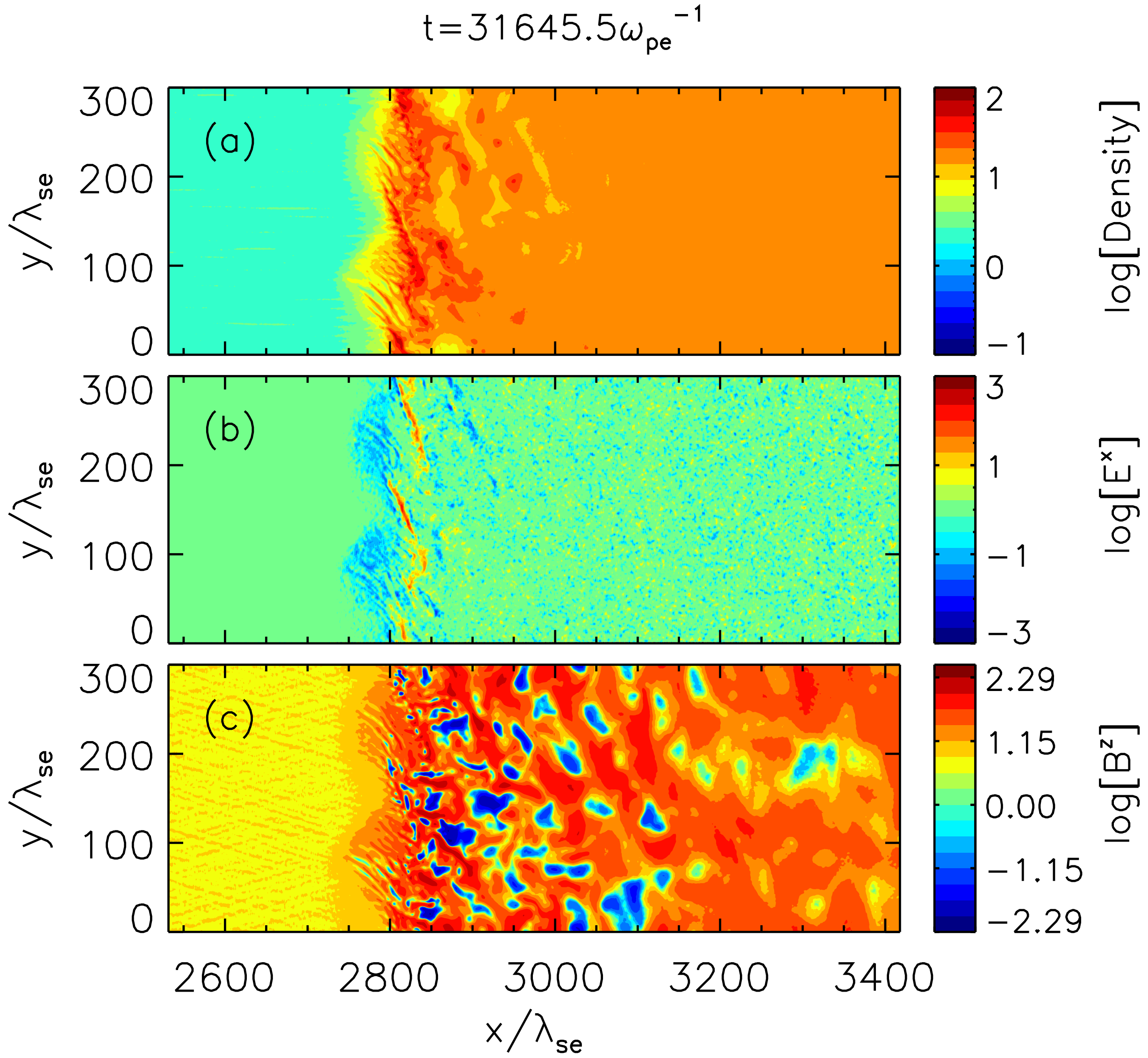

Figure 4.16: Structure of the reverse-shock transition at the end of the simulation at time $t = 31645.5\,\omega_{pe}^{-1}$. Shown is (a) the density distribution of the dense-plasma ions normalised to the far-upstream density of the dense plasma, (b) the amplitude of the electric field E^x (in sign-preserving logarithmic scale as $\mathrm{sgn}(E^x)\,\left(2.5 + \log\left[\max(10^{-2.5}, |E^x|)\right]\right)$) and (c) the amplitude of the magnetic field B^z (in sign-preserving logarithmic scale as $\mathrm{sgn}(B^z)\,(2 + \log\left[\max(10^{-2}, |B^z|)\right])$).

The picture here is somewhat similar to the one we have at the forward shock, with the difference that the extension of almost all features is three times smaller due to the three times smaller particle skin length as already mentioned above. We can also see a transition from weak large-scale turbulence to strong small-scale turbulence going from downstream towards the shock front, a very sharp shock ramp with an extent of ≈ 60 local electron skin lengths and practically no shock precursor. The shock front makes its appearance as a density amplification between $x = 2800\,\lambda_{se}$ and $x = 2900\,\lambda_{se}$, which, like at the forward shock, is peaking at a compression ratio of ≈ 5.8, i.e., it shows a density enhancement of about 45 %.

Another effect we can investigate is the dependence of the development of filamentary structures in the shock ramp on the different Mach numbers and the shock speed. It was proposed that for quasi-perpendicular collisionless shocks above a critical Mach number, a significant fraction of the incoming ions are reflected at the shock front and thereby cause instabilities[92,93].

Table 4.1: Mach numbers and shock speed of forward and reverse shock in our simulation with and without filamentary structures (FS) in the shock ramp.

Shock	M_A	M_s	v_{sh}	FS
Forward shock	27.8	755.2	$0.39\,c$	yes
Reverse shock	28.4	251.7	$0.13\,c$	no

Table 4.1 summarises the Mach numbers and the shock speed for the forward and reverse shock in our simulation. On the one hand, the forward shock in our simulation, which is a high sonic Mach number shock, shows filamentary structures with an extent of ≈ 60 local electron skin lengths. On the other hand, the reverse shock in our simulation, which has a much lower sonic Mach number, exhibits no noticeable filamentary structures. Since the Alfvénic Mach number of both shocks is nearly the same, this observation might indicate that the sonic Mach number is this critical number.

Table 4.2: Mach numbers and shock speed of other publications with or without filamentary structures (FS) in the shock ramp.

Publication	M_A	M_s	v_{sh}	FS
Amano/Hoshino (2009)	14	≈ 30	$0.33\,c$	yes
Kato/Takabe	130	≈ 30	$0.33\,c$	yes
Guo/Sironi/Narayan (2014)	8	3	$0.15\,c$	no
Riquelme/Spitkovsky (2011)	7	≈ 40	$0.14\,c$	no
Caprioli/Spitkovsky (2014)	50	50	$0.001\,c$	no

Table 4.2 summarises the Mach numbers and the shock speed for other publications which present results for quasi-perpendicular collisionless shocks. The sonic Mach number in all presented publications are much lower than even the sonic Mach number of our reverse shock. Nevertheless, in two cases[94,95] filamentary structures in the shock ramp are observed. The shock speed used in these two publications is comparable to the speed of our forward shock. On the other hand, the shock speed in the publications where no filamentary structures are observed in the shock ramp[96,97,98] is comparable to or lower than the speed of our reverse shock. Therefore, our results suggest that the development of filamentary structures in the shock ramp of quasi-perpendicular collisionless shocks

---

[92] Bale et al., Quasi-perpendicular Shock Structure and Processes

[93] Kennel/Edmiston/Hada, A Quarter Century of Collisionless Shock Research.

[94] Amano/Hoshino, The Astrophysical Journal 690 [2009].

[95] Kato/Takabe, The Astrophysical Journal 721 [2010].

[96] Guo/Sironi/Narayan, ArXiv e-prints 2014.

[97] Riquelme/Spitkovsky, The Astrophysical Journal 733 [2011].

[98] Caprioli/Spitkovsky, The Astrophysical Journal 783 [2014].

might not necessarily be determined by the existence of a critical sonic Mach number but by a critical shock speed.

The same indicators for SSA and SDA we observe at the forward shock are also present at the reverse shock, with smaller extent in x-direction, though. Electrons and ions are captured by the bipolar electrostatic field and electrostatic waves at the shock front visible in Figure 4.16(b). They are gyrating at the shock front and drifting along the motional electric field, as can be seen in the phase-space distributions (see Figures 4.17(c) to (f)) at the position of the shock between $x = 2800\,\lambda_{se}$ and $x = 2900\,\lambda_{se}$. Again, these are typical indicators for particle pre-acceleration via SSA. As for the forward shock, we can observe a small electric field amplification in the shock foot at $x \approx 2750\,\lambda_{se}$ (see Figure 4.17(b)) which is a Buneman instability caused by a population of ions that is reflected at the shock front. They are reflected in $-x$-direction (see Figure 4.11(g)) at the magnetic field gradient of the reverse shock and are drifting along the shock front in $+y$- and $-z$-direction parallel to the motional electric field as can be seen in Figures 4.17(e) and (f). This is the typical indicator for SDA. Like for the forward shock, the electrons are re-thermalised and pre-heated via the same process[99].

We can also observe the same oblique alignment in the phase-space distribution of the momentum component p^z in Figure 4.17(f) as we observe for the forward shock, but on smaller scales. Again this effect might be due to the 2D3V nature of our simulation.

---

[99] Guo/Sironi/Narayan, ArXiv e-prints 2014.

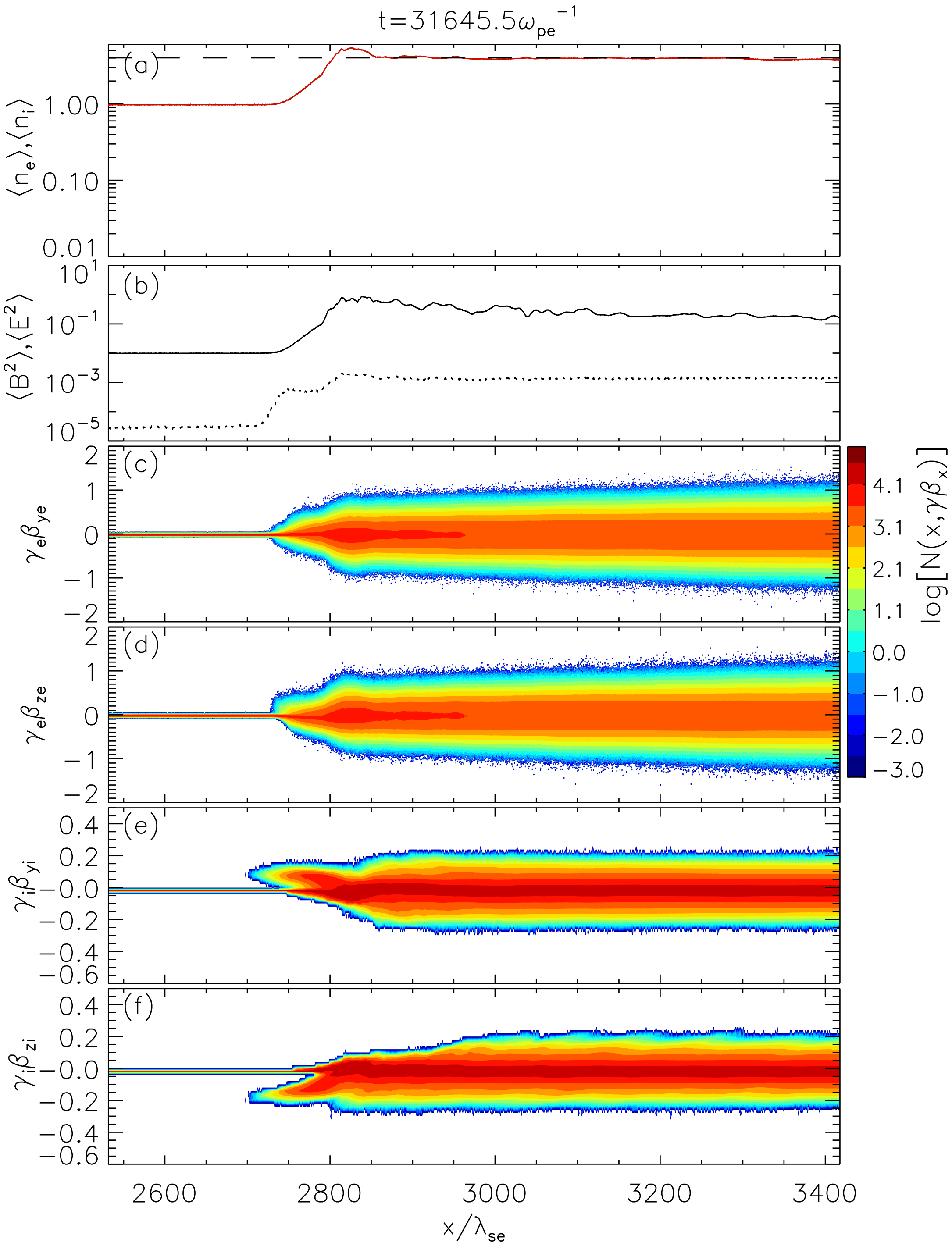

Figure 4.17: Structure of the reverse-shock transition at the end of the simulation at time $t = 31645.5\,\omega_{pe}^{-1}$. Shown are the profiles of (a) the average particle-number density (a logarithmic scale is used), (b) the average magnetic and electric energy density (see Figures 4.8(a) and (b)), and the transversal phase-space distributions separately for the dense-plasma particles: p^y (c) and p^z (d) for dense-plasma electrons and p^y (e) and p^z (f) for dense-plasma ions. In panel (a), the horizontal dashed line marks the magnetohydrodynamic compression level of $n_{R,d}/n_{R,u} = 4.02$ for the reverse shock.

Structure of the Contact Discontinuity Vicinity

Using the collision of two counter-streaming plasmas for the creation of a shock gives us the benefit to be able to also study the vicinity of the contact discontinuity (CD) with our simulation. Figures 4.18 and 4.19 present the structure near the contact discontinuity at the end of the simulation at time $t = 31645.5\,\omega_{pe}^{-1}$. The left column in Figure 4.18 displays the amplitudes of the electric field components E^x, E^y, E^z and the right column displays the amplitudes of the magnetic field components B^x, B^y, B^z. Figure 4.19 presents a version of Figure 4.11 that magnifies the CD vicinity whereby we choose to display the phase-space distribution in p^z instead of p^x. The CD is clearly visible at $x \approx 3850\,\lambda_{se}$ in all plots. It is characterised by a very sharp and very strong amplification of both the electric and magnetic field that is most prominently visible in E^x, E^z and B^y.

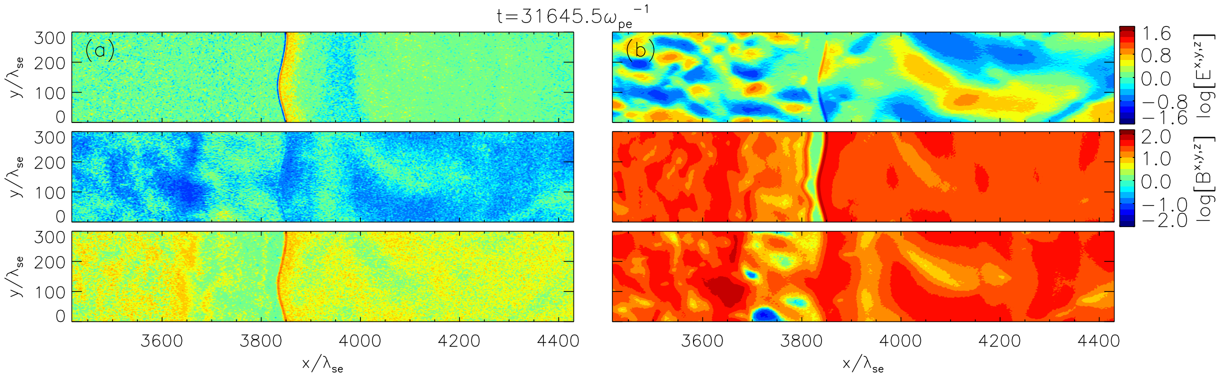

Figure 4.18: Structure of the contact discontinuity vicinity at the end of the simulation at time $t = 31645.5\,\omega_{pe}^{-1}$. Shown are (a) the amplitude of the electric field components E^x, E^y, E^z (in sign-preserving logarithmic scale as $\mathrm{sgn}(E^i)\,\left(2.5 + \log\left[\max(10^{-2.5}, |E^i|)\right]\right)$) and (b) the amplitude of the magnetic field components B^x, B^y, B^z (in sign-preserving logarithmic scale as $\mathrm{sgn}(B^i)\,\left(2 + \log\left[\max(10^{-2}, |B^i|)\right]\right)$).

The position of this field amplification coincides exactly with the position of a density excess of tenuous-plasma electrons visible in Figure 4.19(a) and (d), which peaks at a compression ratio of ≈ 6, i.e., it shows a density enhancement of about 50 %. These particular electrons are trapped on the far side of the CD at a very early stage of the simulation by first crossing the position of the to be formed CD getting reflected by the incoming dense plasma and finally encountering the freshly formed CD. They are already visible as a slight density amplification in Figure 4.10(f) at $x \approx 5450\,\lambda_{se}$. The trapped electrons are gyrating around the downstream magnetic field of the reverse shock and are drifting along the motional electric field in $-y$- and $+z$-direction, thereby creating the electric structures visible in E^y and E^z. On the other hand, they also get pushed by the CD that is moving to the left in our simulation frame. This is the cause of the bipolar structure visible in E^x. This continuous current of streaming electrons also creates bipolar structures in the magnetic field which is most prominently visible in B^x. However, the large scale turbulence in the amplified ambient magnetic field obscures this structure in B^y and B^z. Only B^y shows a stripe of slightly more amplified magnetic field at the location of the CD. This whole structure might be a hint towards particle acceleration at the CD.

To the immediate left of the CD we can observe a dent of $\approx 200\,\lambda_{se} = 28\,\lambda_{si}$ width in the magnetic field profile that is not visible in the electric field profile. We observed a similar dent in our parallel shock simulation (see Figure 9 in N2012). In the current simulation, it becomes apparent that this dent coincides with a population of heated dense-plasma ions near the CD visible in Figure 4.11 (e). However, we can also find a significant portion of heated dense-plasma ions in this region that are trapped on the far side of the CD which we already mentioned in Section 4.4.1.

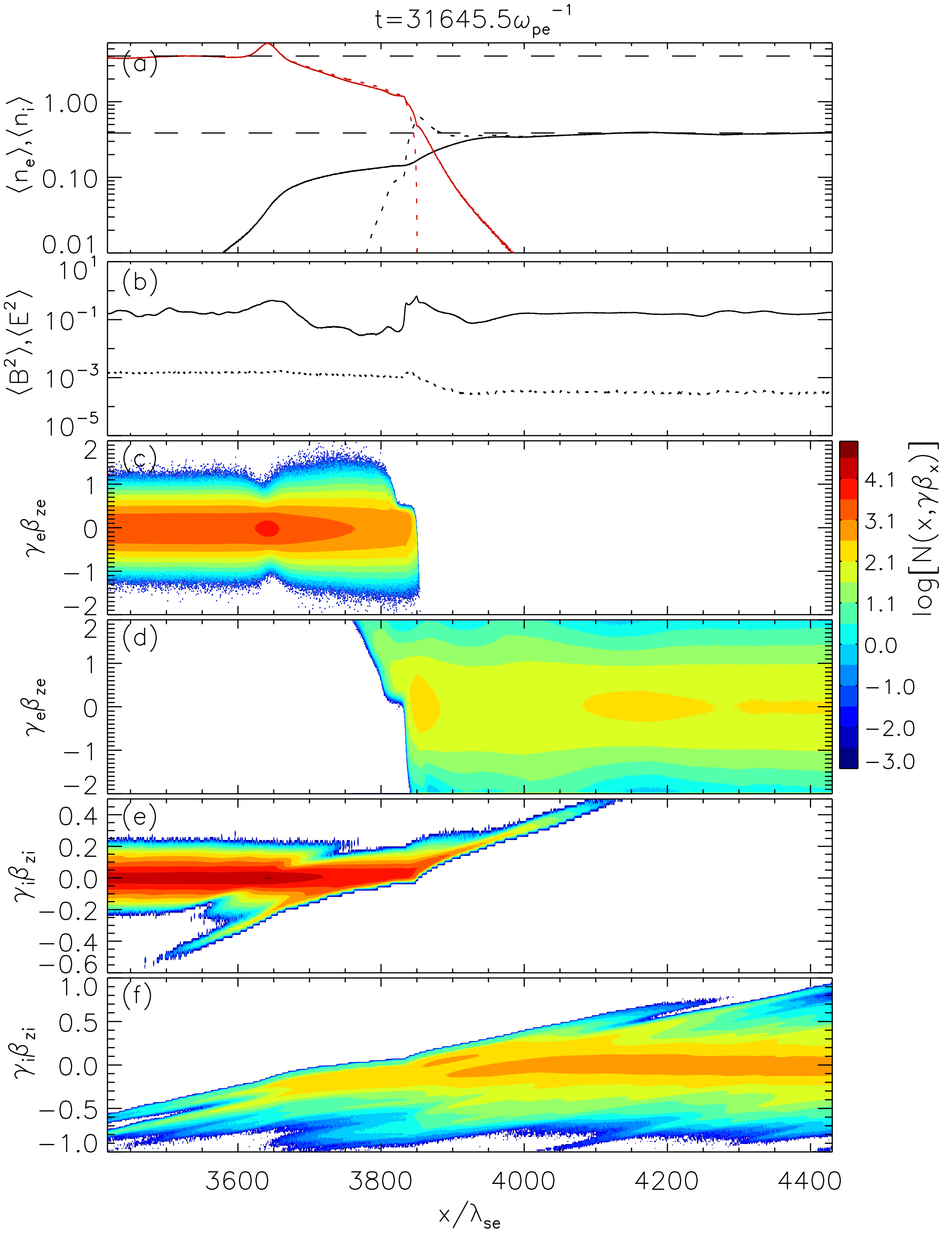

Figure 4.19: Structure of the contact discontinuity vicinity at the end of the simulation at time $t = 31645.5\,\omega_{pe}^{-1}$. Shown are the profiles of (a) the average particle-number density (a logarithmic scale is used), (b) the average magnetic and electric energy density (see Figures 4.8(a) and (b)), and the transversal phase-space distributions separately for all particle species: electrons of the dense (c) and tenuous (d) plasma and ions of the dense (e) and tenuous (f) component. In panel (a), the horizontal dashed lines mark the magnetohydrodynamic compression level of $n_{R,d}/n_{R,u} = 3.86$ for the forward shock (lower line) and $n_{L,d}/n_{L,u} = 4.02$ for the reverse shock (upper line).

Another significant feature of the CD vicinity is a stripe of very small field amplitude visible in E^z, B^x and B^z to the immediate left of the CD. This stripe is very stable over a long time, in fact, from the time of its creation at $t \approx 8000\,\omega_{pe}^{-1}$ until the end of our simulation at $t = 31645.5\,\omega_{pe}^{-1}$. A look at the phase-space distribution of tenuous-plasma and dense-plasma electrons in Figures 4.19(c) and (d) reveals that this particular structure is caused by two counter-streaming electron beams that are drifting in opposite z-directions exactly in this region and thereby cancelling the electric and magnetic fields as we are observing it. The drift in opposite directions of equally charged particles suggests that this effect must be dominated by the Lorentz force.

The final remarkable structure we want to point the reader at is the strongly pronounced bipolar structure in B^z between $x \approx 3600\,\lambda_{se}$ and $x \approx 3770\,\lambda_{se}$. It is constituted by a large region of positive B^z at coordinates $(x, y) \approx (3650, 100)\,\lambda_{se}$ accompanied by an equally large region of negative E^y at the same coordinates and a somewhat smaller region of negative B^z at coordinates $(x, y) \approx (3730, 20)\,\lambda_{se}$ accompanied by an equally large region of positive E^y at the same coordinates. A smaller twin of this structure can be found at coordinates $(x, y) \approx (3660, 240)\,\lambda_{se}$ and $(x, y) \approx (3700, 160)\,\lambda_{se}$. Both structures emerged around the same time as the stripe of collapsed fields mentioned above. Looking at the time evolution of the magnetic field reveals that they are very stable over time and are only slightly altering their shape. The dent in the magnetic field profile mentioned earlier also coincides with the structures of negative magnetic field.

Similar structures were also observed by Murphy/Dieckmann/Drury (2010) and Murphy et al. (2010) and identified as flux tubes. Due to the 2D3V nature of our simulation it is not possible to see the extent of the magnetic field lines into the z-direction. However, we can assume that in real 3D space they should eventually close. Therefore, we can conclude that we are indeed observing a long-time stable structure in a magnetised plasma, known as a magnetic island[100]. Moreover, we can observe that dense-plasma electrons and ions are effectively captured by this phenomenon as is visible by a density enhancement of about 50 % in the density profile in Figure 4.19(a), and also in the phase-space plots in Figures 4.19(c) and (e). Yet another characteristic of magnetic islands is visible in Figure 4.19(c). The electrons that are trapped inside this phenomenon are slightly colder than the surrounding plasma.

---

[100] Waelbroeck, Nuclear Fusion 49 [2009].

4.4.3 Particle Distributions

Like for our parallel shock simulation, particle distributions are calculated in the rest frame of the downstream plasma, defined by the CD speed $\beta_{CD} = -0.06$ in the simulation frame. Although the downstream plasma is turbulent on large scales in the CD rest frame, these turbulent motions are slow and do not significantly distort the spectra. We verified this assumption by transforming the spectra into the local rest frame which yields the same results.

Particle Distributions in the Forward Shock Transition

As mentioned above, we define the forward-shock downstream region as the area of compressed plasma with compression ratio ≈ 4 that is dominated by particles of the tenuous plasma which have a bulk velocity similar to that of the CD. At $t = 31645.5\,\omega_{pe}^{-1}$, the downstream region extends over the range $x \approx 4500 - 6000\,\lambda_{se}$ (see Figure 4.11). Left of this location is the CD region in which we can find both dense and tenuous plasma and where additional processes may occur that alter the particle spectra. Therefore, to calculate the particle distributions we choose slices of width $\approx 300\lambda_{se} = 42\lambda_{si}$, centred at five different locations in the downstream region of the forward shock. The slices are stationary with respect to the CD, and thus the shock front moves steadily away from the location at which spectra are measured.

Figure 4.20 presents the spectra of tenuous-plasma electrons and ions at time $t = 31645.5\,\omega_{pe}^{-1}$. The distribution of the electrons appears to be quasi-thermalised, while the distribution of the ions clearly exhibits a non-thermal tail. The validity of this conclusion can be deduced from the isotropy of the phase-space distributions which we tested and which is also visible in Figures 4.11(d), (f) and Figure 4.13(c) to (f). This is in contrast to the distribution functions we found in the forward-shock downstream region in our parallel shock simulation (see Figure 13 in N2012), where the distribution function of the tenuous-plasma ions exhibits a plateau when integrated over any two momentum coordinates, e.g., $f(p^x) = \int \mathrm{d}p^y\,\mathrm{d}p^z\,f(\boldsymbol{p})$. For the perpendicular case we do not observe such a plateau. Moreover, the energy of the most energetic ions visible in the distribution is about a factor two higher than in the parallel case.

The evolution of the spectra going from young particle populations near the shock towards old populations in the far downstream region coincides with the temporal evolution of the particle spectra at a fixed position in the downstream region of the shock. Our results are consistent with the electron distributions by Amano/Hoshino (2009) and the ion distributions by Caprioli/Spitkovsky, which they get from their simulations of a high sonic Mach number shock ($M_s \approx 30 \ldots 50$). Like them, we can only observe a marginal increase in the thermal energy in the electron distributions and the evolution of a non-thermal tail in the ion distributions.

The electron distribution and the thermal part of the ion distribution are well-fitted by a kappa distribution of the following form:

$$f(E_{\mathrm{kin}}) = \alpha(\kappa) E_{\mathrm{kin}}^{\eta} \left(1 + \frac{E_{\mathrm{kin}}}{\beta(\kappa)}\right)^{-\kappa}, \tag{4.7}$$

with $\eta \approx 2.2$ and $\kappa \approx 43.7$ for the electron distribution and with $\eta \approx 2.4$ and $\kappa \approx 5.3$ for the ion distribution. We choose to fit a kappa distribution instead of a Maxwellian distribution, which would be the limit for $\kappa \to \infty$, since it is the relaxational equilibrium state one would expect in a collisionless space plasma[101,102].

---

[101] Pierrard/Lazar, Solar Physics 267 [2010].

[102] Livadiotis/McComas, Space Science Reviews 175 [2013].

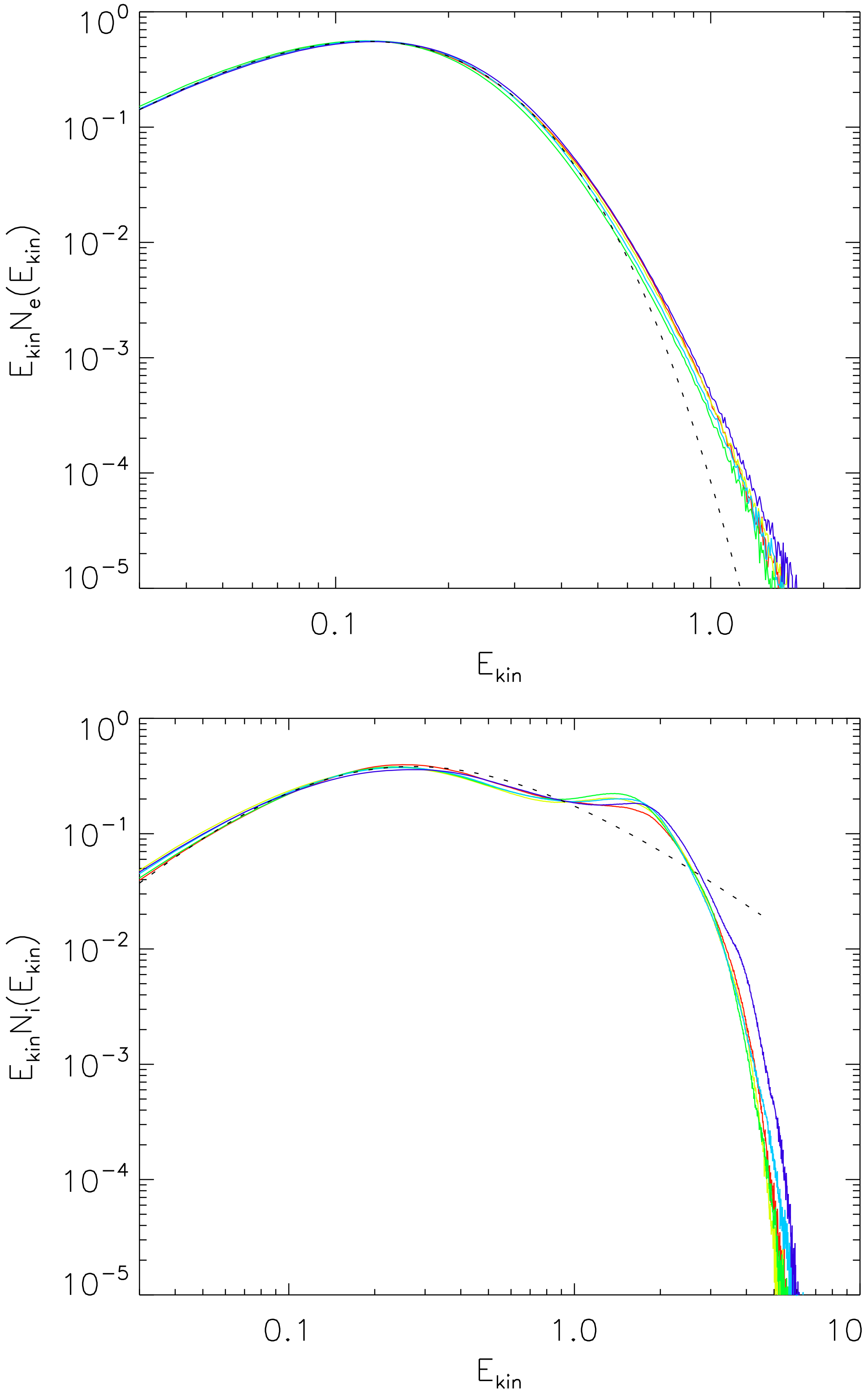

Figure 4.20: Kinetic-energy spectra of tenuous-plasma electrons (*upper panel*) and tenuous-plasma ions (*lower panel*) in the forward-shock downstream region at $x \approx 5700 - 6000\,\lambda_{se}$ (red), $x \approx 5400 - 5700\,\lambda_{se}$ (yellow), $x \approx 5100{-}5400\,\lambda_{se}$ (green), $x \approx 4800{-}5100\,\lambda_{se}$ (blue), $x \approx 4500{-}4800\,\lambda_{se}$ (dark-blue) and time $t = 31645.5\,\omega_{pe}^{-1}$ in the local rest frame. The spectra are normalised and expressed in simulation units, in which $m_ec^2 = 0.25$. The dotted line indicates a kappa-distribution fit to the spectra.

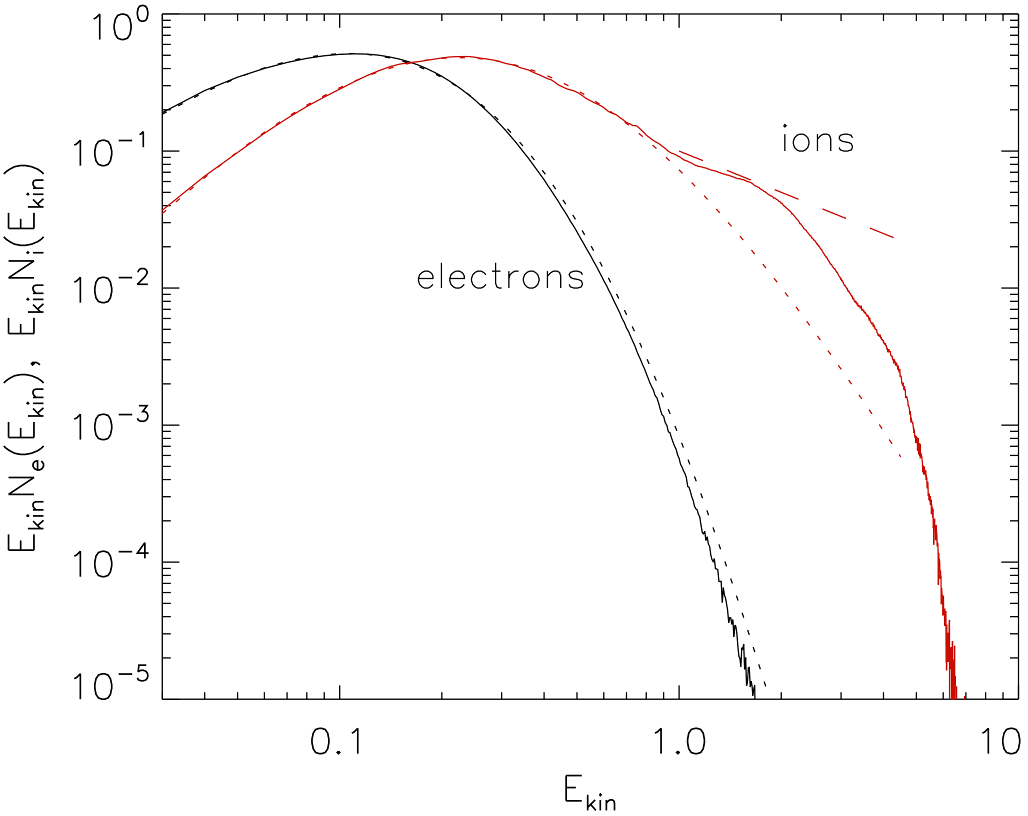

Figure 4.21: Kinetic-energy spectra of tenuous-plasma electrons (black line) and tenuous-plasma ions (red line) in the forward-shock region at $x \approx 6550 - 6850\,\lambda_{se}$ and time $t = 31645.5\,\omega_{pe}^{-1}$ in the local rest frame. The spectra are normalised and expressed in simulation units, in which $m_e c^2 = 0.25$. The dotted lines indicate a kappa-distribution fit to the spectra and the dashed line indicates a power-law fit to the ion spectrum with $\gamma = 2$.

The particle distributions at the forward shock are presented in Figure 4.21. The differences compared to the distributions in the downstream region are minimal. However, in the ion distribution we can see a shift of the kappa distribution to $\eta \approx 2.7$ and $\kappa \approx 8.0$ and a slight decrease in the non-thermal tail with the development of a power-law with spectral index close to $\gamma = 2$. We observe a small shift of the electron distribution towards smaller energies whereby the kappa distribution fit is shifted to $\eta \approx 2.0$ and $\kappa \approx 14.2$. These shifts are consistent with our observation of the broadening of the phase-space distributions at the shock (see Figures 4.11(d) and (f) and Figures 4.13(c) to (f)). Due to the strong confinement to the shock region, we can find much more particles in the shock than in the downstream region, with most of them at lower energies. The particles are undergoing shock surfing acceleration (SSA) and once they reached an energy that is high enough to allow their escape from the electrostatic potential inside the shock they are able to propagate either to the downstream or upstream region.

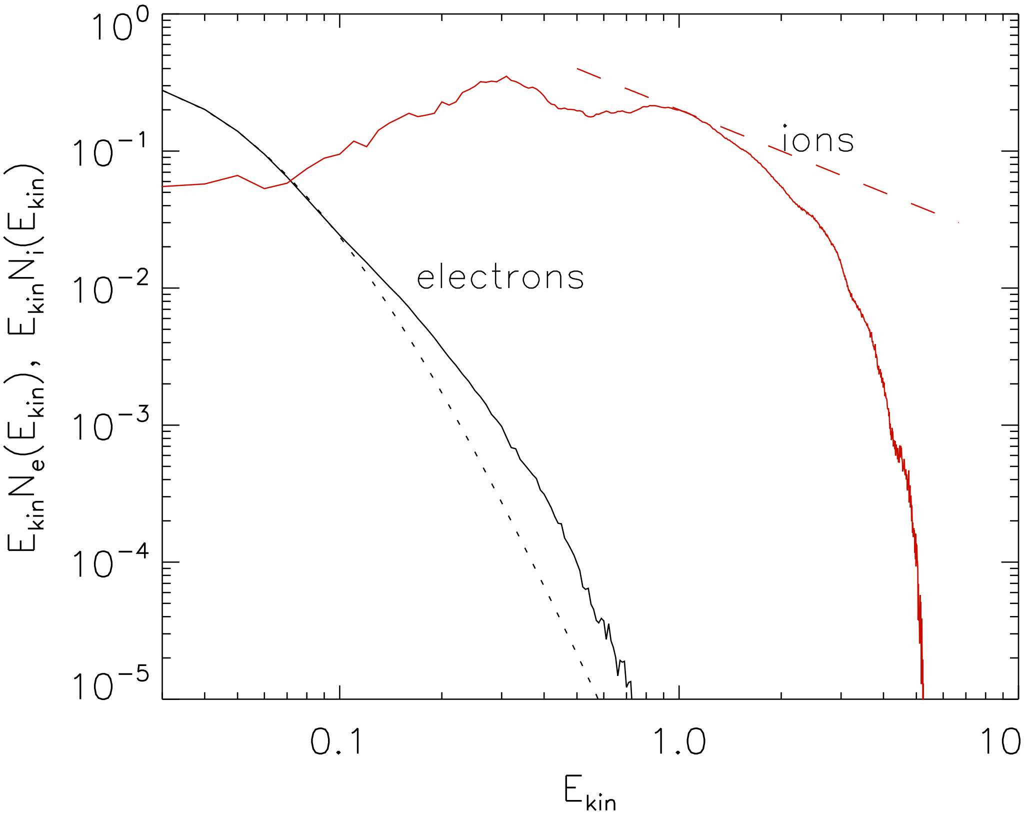

Figure 4.22: Kinetic-energy spectra of tenuous-plasma electrons (black line) and tenuous-plasma ions (red line) in the forward-shock foot region at $x \approx 6850 - 7150\,\lambda_{se}$ and time $t = 31645.5\,\omega_{pe}^{-1}$ in the local rest frame. The spectra are normalised and expressed in simulation units, in which $m_e c^2 = 0.25$. The dotted line indicates a kappa-distribution fit to the electron spectrum and the dashed line indicates a power-law fit to the ion spectrum with $\gamma = 2$.

Figure 4.22 presents the particle distributions in the forward-shock foot region in a slice of the same width as before, but now centred at $x \approx 7000\lambda_{se}$. At this time step, this is the position of the particles we considered to be undergoing SDA (see Figure 4.12). A typical indication for this process is the anisotropy we observe in the electron and ion distributions and which is also visible in Figures 4.13(c) to (f). The distribution of tenuous-plasma electrons is well fitted by a kappa distribution with $\eta \approx 1.2$ and $\kappa \approx 8.1$ and shows a small non-thermal tail, whereas the distribution of tenuous-plasma ions exhibits a large non-thermal population. The shape of the electron distribution is consistent with the predicted distribution for SDA as calculated in Guo/Sironi/Narayan (2014) (compare Figure 7 therein).

Particle Distributions in the Reverse Shock Transition

As for the forward shock, we define the reverse-shock downstream region also as the area of compressed plasma with compression ratio ≈ 4 dominated by particles of the dense plasma with bulk velocity similar to that of the CD. At $t = 31645.5\,\omega_{pe}^{-1}$, this region extends over the range $x \approx 3000 - 3400\,\lambda_{se}$ (see Figure 4.11). Again we exclude the CD region. The distributions in Figure 4.23 are taken in slices of width $\approx 100\lambda_{se} = 14\lambda_{si}$ centred at four different locations in the downstream region of the reverse shock.

Again we tested that the phase-space distributions of the dense-plasma particles are isotropic (see also Figures 4.11(c), (e) and Figures 4.17(c) to (f)). In Figure 4.23, the distribution of the electrons seems to be approximately thermalised as is indicated by the dotted line representing a Maxwellian distribution. On the other hand, the ion distribution exhibits a small non-thermal tail. For the parallel shock we could only see anisotropy in the spectrum caused by returning particles. This is not the case here, since the downstream region of the reverse shock is very well isotropised as we have tested.

The evolution of the spectra going from young particle populations near the shock towards old populations in the far downstream region are similarly found in the results of the low sonic Mach number shock ($M_s \approx 3$) simulated by Guo/Sironi/Narayan (2014). As in their results, the thermal energy of the electrons increases, while the energy in the non-thermal tail of the ions shows a slight decrease and tends towards a re-thermalised equilibrium state.

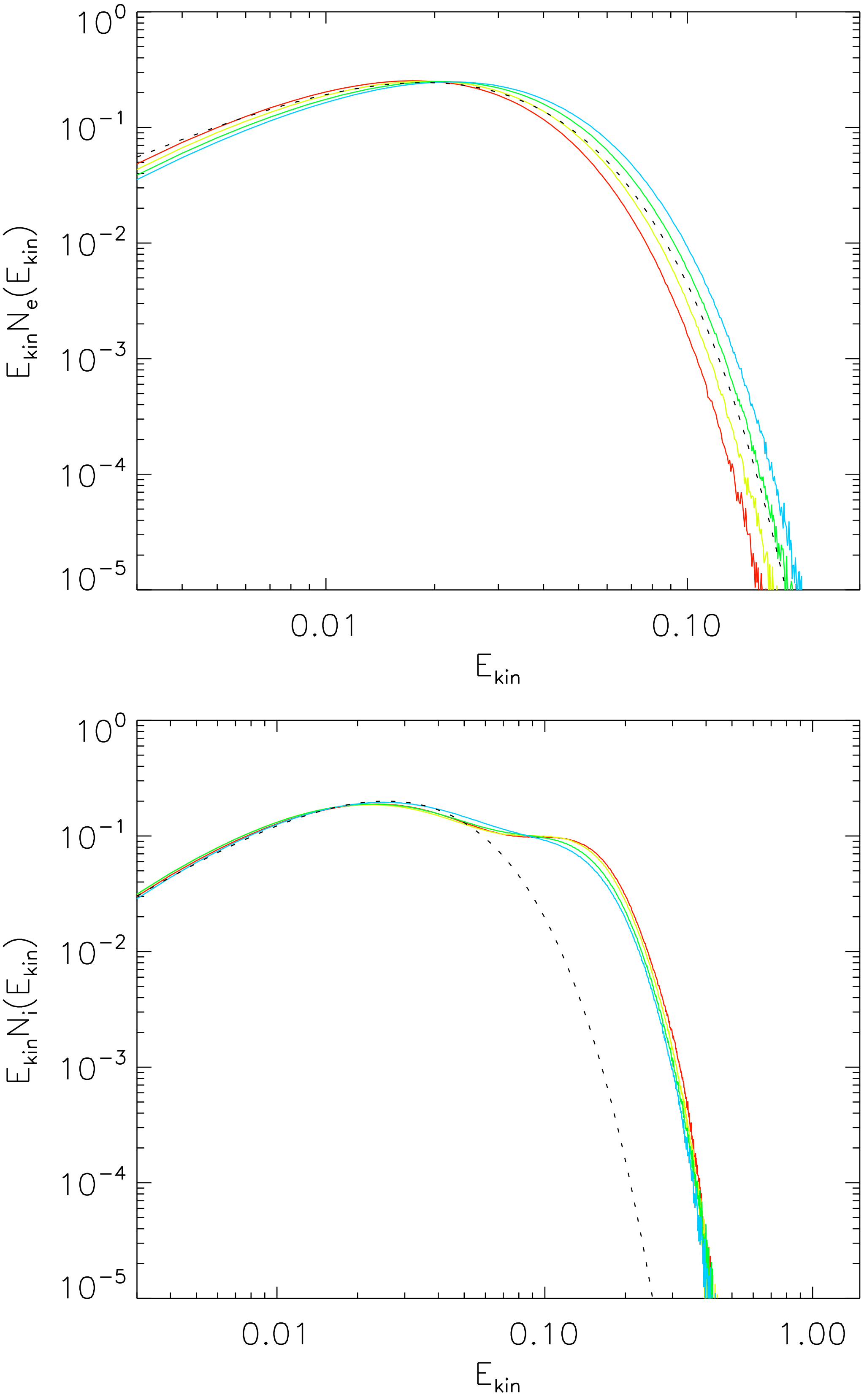

Figure 4.23: Kinetic-energy spectra of dense-plasma electrons (*upper panel*) and dense-plasma ions (*lower panel*) in the reverse-shock downstream region at $x \approx 3000 - 3100\,\lambda_{se}$ (red), $x \approx 3100 - 3200\,\lambda_{se}$ (yellow), $x \approx 3200 - 3300\,\lambda_{se}$ (green), $x \approx 3300 - 3400\,\lambda_{se}$ (blue) and time $t = 31645.5\,\omega_{pe}^{-1}$ in the local rest frame. The spectra are normalised and expressed in simulation units, in which $m_ec^2 = 0.25$. The dotted line indicates a Maxwellian fit to the spectra.

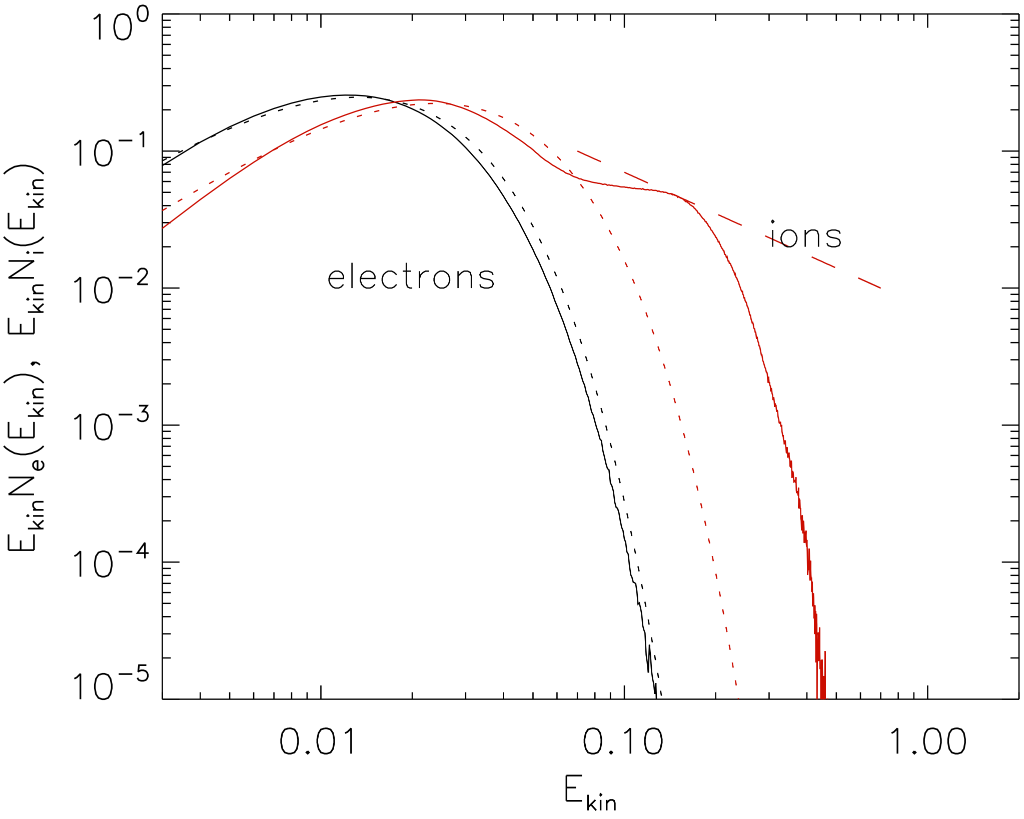

Figure 4.24: Kinetic-energy spectra of dense-plasma electrons (black line) and dense-plasma ions (red line) in the reverse-shock region at $x \approx 2800 - 2900\,\lambda_{se}$ and time $t = 31645.5\,\omega_{pe}^{-1}$ in the local rest frame. The spectra are normalised and expressed in simulation units, in which $m_e c^2 = 0.25$. The dotted lines indicate a Maxwellian fit to the spectra and the dashed line indicates a power-law fit to the ion spectrum with $\gamma = 2$.

Figure 4.24 presents particle distributions at the reverse shock. Like for the distributions at the forward shock, we can observe a shift of the thermal component of the ion distribution towards higher energies and also a slight decrease in the non-thermal tail. We can also observe a power-law with a spectral index slightly smaller than $\gamma = 2$, which might be due to the distribution not having reached its equilibrium state. The electron distribution is again shifted towards lower energies. The explanation is the same as for the forward shock: Low-energy particles are confined in the shock, accelerated via SSA and eventually escape as pre-accelerated particles into the downstream or upstream region.

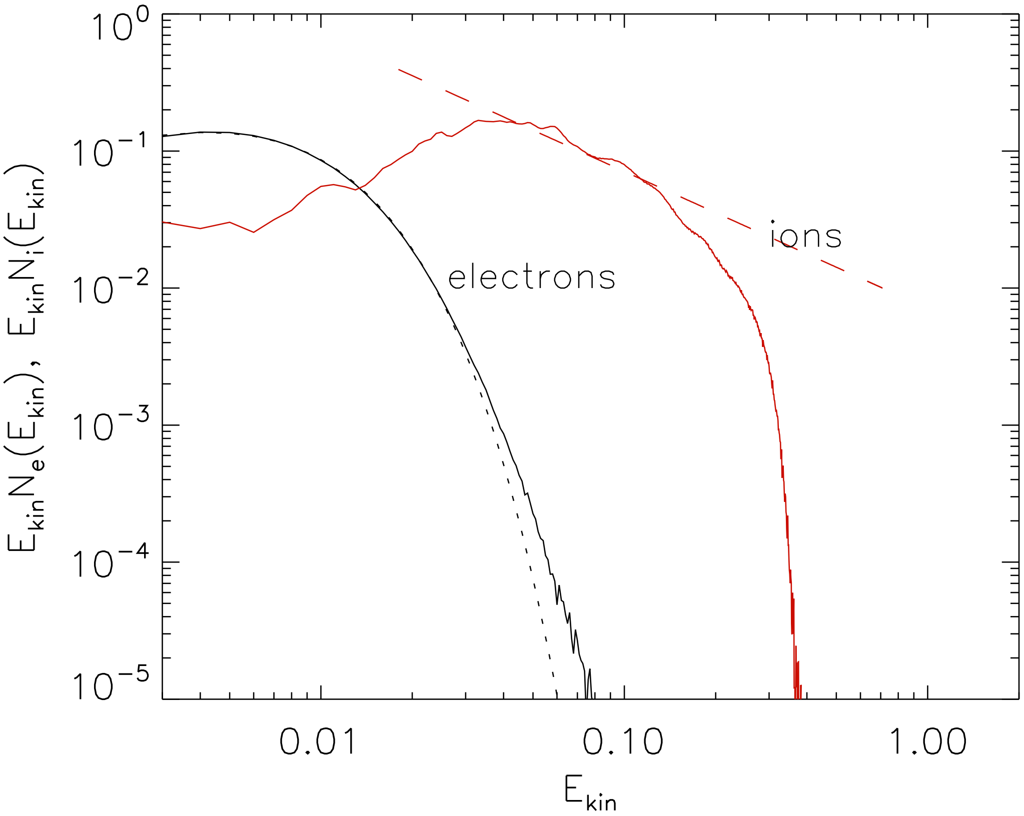

Figure 4.25: Kinetic-energy spectra of dense-plasma electrons (black line) and dense-plasma ions (red line) in the reverse-shock foot region at $x \approx 2700 - 2800\,\lambda_{se}$ and time $t = 31645.5\,\omega_{pe}^{-1}$ in the local rest frame. The spectra are normalised and expressed in simulation units, in which $m_e c^2 = 0.25$. The dotted line indicates a kappa-distribution fit to the electron spectrum and the dashed line indicates a power-law fit to the ion spectrum with $\gamma = 2$.

As for the forward shock, the distributions in the reverse-shock foot region, which are shown in Figure 4.25, show clear indications of SDA. The slice we choose has the same width as before and is centred at $x \approx 2725\lambda_{se}$. The electron distribution is very well fitted by a kappa distribution with $\eta \approx 0.9$ and $\kappa \approx 2.9 \times 10^7$ and shows a small non-thermal tail. Like for the forward shock, the ion distribution exhibits a large non-thermal population. We can also observe anisotropy in the distributions, which are also visible in Figures 4.17(c) to (f), and which is a typical indication for SDA.

Particle Distributions in the Contact Discontinuity Vicinity

In addition to the particle distributions in the downstream region and the shock foot region, we also show particle distributions that are taken in the contact discontinuity (CD) vicinity. We choose a slice of width $\approx 500\lambda_{se} = 70\lambda_{si}$ centred at the position of the CD at $x \approx 3850\lambda_{se}$. Figure 4.26 shows the distribution of tenuous-plasma electrons and ions, whereas Figure 4.27 shows the distribution of dense-plasma electrons and ions.

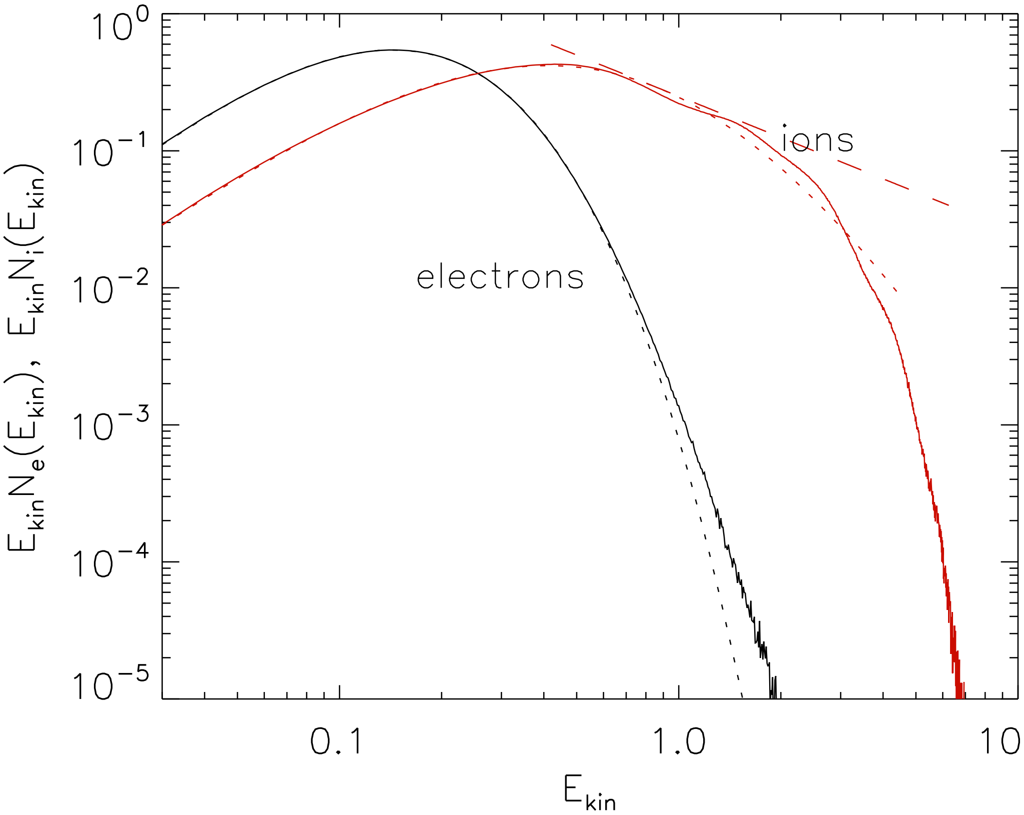

Figure 4.26: Kinetic-energy spectra of tenuous-plasma electrons (black line) and tenuous-plasma ions (red line) in the contact discontinuity vicinity region at $x \approx 3600 - 4100\,\lambda_{se}$ and time $t = 31645.5\,\omega_{pe}^{-1}$ in the local rest frame. The spectra are normalised and expressed in simulation units, in which $m_e c^2 = 0.25$. The dotted lines indicate a kappa-distribution fit to the spectra and the dashed lines indicates a power-law fit to the ion spectrum with $\gamma = 2$.

The distribution of the tenuous-plasma particles show clear evidence of particle acceleration in this region. The electron distribution is well-fitted by a kappa distribution with $\eta \approx 2.1$ and $\kappa \approx 32.9$ and exhibits a small non-thermal tail. On the other hand, the ion distribution resembles the spectrum we obtained in the downstream region of the forward shock (see Figure 4.20). The low-energy part is well-fitted by a kappa distribution with $\eta \approx 1.8$ and $\kappa \approx 6.8$ and we can observe the development of a power-law with a spectral index close to $\gamma = 2$.

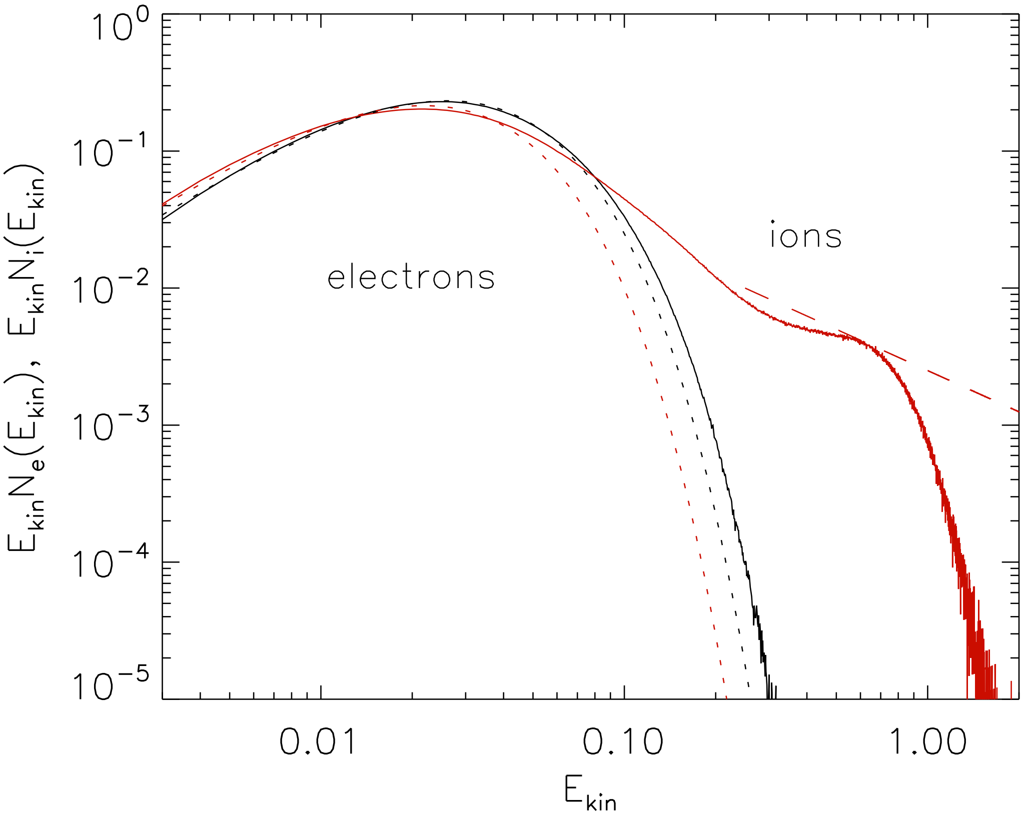

Figure 4.27: Kinetic-energy spectra of dense-plasma electrons (black line) and dense-plasma ions (red line) in the contact discontinuity vicinity region at $x \approx 3600 - 4100\,\lambda_{se}$ and time $t = 31645.5\,\omega_{pe}^{-1}$ in the local rest frame. The spectra are normalised and expressed in simulation units, in which $m_e c^2 = 0.25$. The dotted lines indicate a Maxwellian fit to the spectra and the dashed line indicates a power-law fit to the ion spectrum with $\gamma = 2$.

We find a completely different picture for the distributions of the dense-plasma particles. The electron distribution resembles the one we obtained in the downstream region of the reverse shock (see Figure 4.23) but with a shift towards higher energies. Its Maxwellian shape indicates that the dense-plasma electrons are efficiently re-thermalised. On the other hand, the ion distribution clearly shows a non-thermal population and a power-law with a spectral index slightly smaller than $\gamma = 2$, which again might be due to the distribution not having reached its equilibrium state. This population can also be seen in Figure 4.11(e) as a very distinctive bulge in the ion phase-space distribution. These particles are accelerated in the magnetic island structures discussed in Section 4.4.2.

4.5 Summary and Discussion

We have performed 2D3V PIC simulations of non-relativistic plasma collisions with perpendicular large-scale magnetic field. With the current study, we continue our investigations of the shocks that started with the parallel shock simulations published in Niemiec et al. (2012). Here, the main question we addressed was how changing the magnetic field from the parallel to perpendicular configuration influences the resulting shock structure and the efficiency of particle pre-acceleration.

To address this question, we devised a new setup using asymmetric plasma flows, i.e., utilizing the collision of plasma slabs of different density, leading to two different shocks and a CD that is self-consistently modeled. In contrast to the setup used by Murphy et al. (2010) and Murphy/Dieckmann/Drury (2010), we avoid the creation of an artificial dipole at the contact discontinuity (CD) by using a transition zone between full motional electric fields inside the plasmas and zero electric field in a small plasma-free area between the plasma flows at the beginning of the simulation. Thereby, we ensure that our simulation is as clean as possible.

The simulation parameters are chosen such that they are close to those of a young supernova remnant (SNR), except that we use a reduced ion-to-electron mass ratio of $m_i/m_e = 50$ to capture both electron and ion dynamics within the bounds of our simulation. The density ratio between the dense plasma representing the supernova ejecta (SNE) and the tenuous plasma representing the interstellar medium (ISM) is 10, which is about the same ratio we would expect to find at a young supernova remnant at the beginning of its free expansion phase in a typical ISM environment. However, shock velocities we normally find in such an environment are about a factor of a few lower than in our simulations. The sonic and Alfvénic Mach numbers of the forward shock are $M_{s,R} = v'_{S,R}/c_s = 755.2$ and $M_{A,R} = v'_{S,R}/v_A = 27.8$, respectively, and that of the reverse shock are $M_{s,L} = v'_{S,L}/c_s = 251.7$ and $M_{A,L} = v'_{S,L}/v_A = 28.4$, respectively. Here, as forward and reverse shock we denote the shocks propagating into the tenuous plasma and into the dense plasma, respectively.

Our results can be summarised as follows:

1. Our newly developed setup leads to the creation of a very clean perpendicular shock without artificial transients that may limit the veracity of the simulation. Eventually, a double-shock structure evolves within a few thousand electron plasma times, ω_{pe}^{-1}, or a few ion cyclotron times, ω_{ci}^{-1}. Compared to our parallel shock simulation, the perpendicular shock develops thrice as fast and the region of compressed plasma reaches twice the size in the same amount of time. The structure of the shock is very stable over time. This seems to be in contradiction with the results of Umeda/Yamao/Yamazaki (2008); Umeda/Yamao/Yamazaki (2009) who observe a cyclic reformation of the shock front over time. However, in our simulation we do not observe the disappearance and reappearance of the shock front but only small variations in the steepness of the shock ramp of both forward and reverse shock, which were also observed by Shimada/Hoshino (2005). The time-scale on which these variations occur is about $1 \dots 2\,\omega_{ci}^{-1}$, which is consistent with the low-beta 1D results by Scholer/Matsukiyo (2004).

2. Particles are strongly confined to the collision region of the perpendicular shock, resulting in a nearly non-existent shock precursor and much less turbulent magnetic fields downstream of the shock compared to the parallel shock. The latter result is consistent with the findings of Caprioli/Spitkovsky (2014) in their hybrid simulations. A low amplitude of turbulence would yield a high degree of polarization in radio synchrotron emission, which would be dominated by the homogeneous perpendicular field. Conversely, the strong turbulence in parallel-shock simulations would argue for a low degree of polarisation with varying local polarisation angle[103]. Reynoso/Hughes/Moffett (2013) note that the regions in SN 1006 that are dim in X-rays and the TeV-band indeed show very high degrees of polarization with tangential fields, whereas the magnetic polarization in the lobes is radial, suggesting that parallel shocks at the bright lobes are far more efficient in accelerating electrons to the highest energies. This interpretation requires, however, that the turbulence produced at the shock dominates the polarization signal, and that cosmic-ray induced turbulent magnetic-field amplification upstream of the shock is weak,

---

[103] Stroman/Pohl, The Astrophysical Journal 696 [2009].

otherwise the shock-compressed turbulent field would provide tangential magnetic-field vectors in the polarization data[104]. It is not immediately obvious how weak scattering turbulence upstream would fit to a high acceleration efficiency.

3. Using a setup with two colliding asymmetric plasma flows gives us the benefit of being able to study the quite different forward and reverse shock at the same time. The downstream region of the forward shock has an extension in the direction of the shock normal that is nearly three times the extent of the downstream region of the reverse shock. The compression ratio for both shocks agrees well with the magnetohydrodynamic compression level of ≈ 4. However, we see a density overshoot at the shock front of both forward and reverse shock that exceeds this value by 50 %. This effect is due to shock surfing acceleration (SSA) and agrees well with the findings of Amano/Hoshino (2007), Amano/Hoshino (2009) and Riquelme/Spitkovsky (2011).

4. We can also see clear indications for shock drift acceleration (SDA) operating in the shock foot region of both forward and reverse shock, which is also very well in agreement with the results of Amano/Hoshino (2007), Amano/Hoshino (2009), Riquelme/Spitkovsky (2011) and Guo/Sironi/Narayan (2014). However, the energy distributions they get exhibit a somewhat larger non-thermal electron population than the ones we end up with. This might be due to the very small size of the region in which SDA is occurring in our simulation, which in turn is due to the high sonic Mach numbers of our two shocks[105].

5. Another benefit of having two shocks is that we can study the influence of the different Mach numbers and the shock speed on the development of filamentary structures in the shock ramp in one simulation. The forward shock with it's very high sonic Mach number and high shock speed exhibits filamentary structures in the entire shock ramp. Similar results were obtained by Amano/Hoshino (2009) and Kato/Takabe (2010) at shocks with much lower sonic Mach number but with a shock speed comparable to our forward shock. The reverse shock has a much lower sonic Mach number and exhibits a very sharp shock front with practically no structures in the shock ramp. Similar results were obtained by Guo/Sironi/Narayan (2014), Riquelme/Spitkovsky (2011) and Caprioli/Spitkovsky (2014) at shocks with even lower sonic Mach number but with a shock speed comparable to or lower than our reverse shock. Therefore, our results suggest that the development of filamentary structures in the shock ramp of quasi-perpendicular collisionless shocks might not necessarily be determined by the existence of a critical sonic Mach number[106,107] but by a critical shock speed.

6. In contrast to the widely used injection and relaxation methods which assume the existence of an infinitely sharp contact discontinuity (CD), our setup has the advantage of being able to also study the CD vicinity. This region exhibits some interesting features, as we show in this study. Most remarkable is the existence of a population of tenuous-plasma electrons that is trapped at the location of the CD and gets accelerated. Furthermore, we observe a stripe of very small electric and magnetic field amplitude right next to the CD on the side of the reverse shock. This feature is different from the bipolar structure found by Murphy et al. (2010). However, we can also see a structure that resembles one of their findings that is a magnetic island in the CD vicinity of the downstream region of the reverse shock.

7. The distributions of the dense-plasma electrons in the downstream region and the CD vicinity of the reverse shock mostly show a thermal distribution, which indicates that the electrons are efficiently re-thermalised in these regions. On the other hand, we can see clear evidence of pre-acceleration for the ions in these regions and for both electrons and ions in the other parts of the shock. We observe the development of non-thermal tails in the distributions of tenuous-plasma and dense-plasma electrons in the shock foot regions of both forward and reverse shock and in the tenuous-plasma electron distribution in the CD vicinity. The ion distributions exhibit a tail

---

[104] Stroman/Pohl, The Astrophysical Journal 696 [2009].

[105] Guo/Sironi/Narayan, ArXiv e-prints 2014.

[106] Bale et al., Quasi-perpendicular Shock Structure and Processes

[107] Kennel/Edmiston/Hada, A Quarter Century of Collisionless Shock Research.

of non-thermal particles in all regions of the shock. This result is in agreement with the results of the hybrid simulation of Gargaté/Spitkovsky (2012) and Caprioli/Spitkovsky (2014) and of the PIC simulation of Guo/Sironi/Narayan (2014).

Due to limitations in the utilization of computing resources, we are not able to study the development of the perpendicular shock and the evolution of particle distributions for realistic ion-to-electron mass ratios. However, the results of Riquelme/Spitkovsky (2011) indicate that the qualitative picture does not change significantly as the mass ratio increases towards the realistic value. What changes on the quantitative side is the importance of SSA. According to Riquelme/Spitkovsky (2011), with increasing mass ratio the peak of the thermal part of the electron distribution is shifted to higher values, thereby reducing the fraction of the non-thermal part.

On the other hand, the theoretical derivations of Guo/Sironi/Narayan (2014) indicate that the processes of SSA and SDA are complementary with respect to the sonic Mach number of the shock. While SSA only works in high sonic Mach number shocks, SDA is most efficient in low sonic Mach number shocks. Since our simulated shocks can both be considered as high sonic Mach number shocks, we can assume that SSA should become a significant process. Moreover, both shocks satisfy the trapping condition for electrons as introduced by Matsumoto/Amano/Hoshino (2012) and at least the forward shock shows clearly visible indications for the Buneman instability in the shock foot, which is the main cause of SSA. However, the electron distributions we observe at our two shocks do not exhibit non-thermal populations. This might be an indication for another exception at very low values for the plasma beta β_e in addition to the exception found by Matsumoto/Amano/Hoshino (2012) at high values for β_e which needs to be investigated in more detail in future studies. For our two shocks we have $\beta_{e,R} \approx 10^{-3}$ for the forward shock and $\beta_{e,L} \approx 10^{-2}$ for the reverse shock. On the other hand, we also see clear evidence for SDA, but since this process only happens in a very small region in the shock foot of both forward and reverse shock, this is not in contradiction to the derivations of Guo/Sironi/Narayan (2014). That particles can be injected into SDA for a shock with Alfvénic Mach number like the one we study, is predicted by Amano/Hoshino (2010). The particles that have been pre-accelerated via SSA and SDA so far might be also suitable as a seed population to be injected into further diffusive shock acceleration (DSA) to even higher energies.

Chapter 5

Conclusions

The origin of cosmic rays was the subject of several studies for over a century. The investigations done within this dissertation are one small step to shed some more light on this mystery. Now that we have come to the end, let us review where our investigation led us to.

We started out with nothing more than a fingerprint that is left behind by the cosmic rays here on Earth. This fingerprint is the cosmic ray spectrum which spans a vast range in energy and in flux density. Pinpointing a source of cosmic rays was difficult, since the interstellar magnetic field covers all traces due to the deflection of the particles. However, the fact that a particle's energy is not changed by the Lorentz force allowed us to find possible sources. A celestial object is only capable of accelerating charged particles until their gyro radius becomes larger than the size of the object. This so-called Hillas criterion led us to the observation that particles with energies above 10^{18} eV (the so-called "ankle" of the cosmic-ray spectrum) must have originated outside of our galaxy. For lower energies we can find probable sources within the Milky Way. Eventually, we arrived at the conclusion that the remnants of supernova explosions are our main suspect for the origin of galactic cosmic rays.

In order to eventually pin down supernova remnants (SNRs) as the culprit, we had to investigate the means by which they are capable of accelerating particles. The answer to this most likely lies within the field of shock physics. We found that SNRs are housing two shocks - an outward-moving forward shock and an inward-moving reverse shock - with strong and turbulent magnetic fields which are capable of accelerating particles by a mechanism known as diffusive shock acceleration (DSA). However, shock physics places a limit on which particles are able to enter the game of DSA. Only particles with more then thermal energy are able to do so, which is the so-called injection problem. A mechanism to pre-accelerate particles is needed and, indeed, two processes were identified that are capable of filling this role, namely shock surfing acceleration (SSA)[108] and shock drift acceleration (SDA)[109].

The physical processes happening at SNRs involve scales ranging from micro physics deep inside the shock fronts up to macro physics on scales of the whole remnant. Whereas a conclusive picture of our main suspect always has to include both, the current investigation focused on the former one. Since studying SNR shock fronts on site is currently impossible, we had to devise a simplified model that can be simulated with earthbound computers. The method of choice were Particle-in-Cell (PIC) simulations that are capable of efficiently capturing the physics of astrophysical plasmas using just a handful of elementary equations. We developed a new and clean setup to simulate the formation of a double shock, i.e., consisting of a forward and a reverse shock and a contact discontinuity (CD), by the collision of two counter-streaming plasmas, in which a magnetic field can be woven into. In a previous work[110], we investigated the processes at unmagnetised and at magnetised parallel shocks, whereas in the current investigation, we moved our investigation on to magnetised perpendicular shocks.

---

[108] Sagdeev/Shapiro, Letters to Jounal of Experimental and Theoretical Physics 17 [1973].

[109] Krauss-Varban/Wu, Journal of Geophysical Research 94 [1989].

[110] Niemiec et al., The Astrophysical Journal 759 [2012].

In the main part of this work (Wieland et al. (2014) / Chapter 4) we demonstrated that our newly developed setup has many advantages compared to other approaches that are most commonly used, like the injection method[111] and the relaxation method[112,113]. Most of all we were able to study two shocks like we observe in SNRs. Furthermore, our setup provided a cleaner approach to form a double shock via the collision method from first principles than what we can find in other works. We avoided the assumption of an infinitely sharp CD and the creation of an artificial dipole due to the opposing sign of the motional electric field at the CD that could eventually disturb the physical veracity of our simulation.

We observed the formation of a CD and the two shocks at a very early stage of the simulation. In fact, the perpendicular shock developed thrice as fast as the parallel shock. This is due to the much stronger particle confinement to the collision region by the perpendicular magnetic field. The perpendicular shock provided regions of compressed plasma that are characterised by strong magnetic field compression and subsequent amplification up to two orders of magnitude compared to the ambient magnetic field. The compressed magnetic field showed a clear transition from weak large-scale to strong small-scale turbulence as we moved from the downstream region towards the shock. Similar shock structures were also observed by, e.g., Burgess/Scholer (2007), Amano/Hoshino (2009), Kato/Takabe (2010), Caprioli/Spitkovsky (2014) and Guo/Sironi/Narayan (2014).

At the same time, the strong particle confinement led to the nearly total disappearance of turbulence upstream of the shocks, such that we could observe filamentary structures only in the ramp of the forward shock, which were also observed by Kato/Takabe (2010) and Murphy/Dieckmann/Drury (2010). In contrast, the parallel shock exhibited strong turbulence over the whole shock and a very extended precursor. In that way, the perpendicular shock is much more compact than the parallel shock.

Another characteristic of the compressed regions was the nearly constant particle density with a compression ratio of ≈ 4, i.e., the perpendicular shock shows magnetohydrodynamic characteristics at a very early stage of its development. We found a density overshoot at the two shock fronts and at the CD. These features were caused by particles that are trapped in those regions by a bipolar electric field and we found non-thermal particle populations that indicate pre-acceleration via SSA, which was studied in detail by, e.g. Leroy et al. (1981), Wu et al. (1984), Hoshino (2001), Amano/Hoshino (2007) and Amano/Hoshino (2009). In the shock foot, we also found non-thermal particles that are reflected at the shock front and pre-accelerated via SDA, which was already studied by, e.g., Amano/Hoshino (2007), Amano/Hoshino (2009) and Guo/Sironi/Narayan (2014). The presence of these two processes provides us with enough evidence to pin down perpendicular shocks with physical parameters like the ones we find in SNRs as eligible sources for pre-accelerated particles that are suitable as a population to be injected into further DSA to be accelerated to even higher energies.

We noted that the effect of SSA is not as efficient as one would expect from shocks with high sonic Mach numbers such as our two shocks. Most significantly, we did not observe non-thermal electron populations at the shock fronts. Both shocks satisfy the trapping condition for electrons as introduced by Matsumoto/Amano/Hoshino (2012) and at least at the forward-shock foot we observed clear indications for the Buneman instability[114], which is the main cause for SSA. That we nevertheless do not observe efficient SSA indicates that there is more to understand here. Matsumoto/Amano/Hoshino (2012) pointed out that a high value for the plasma beta, β_e, which is the ratio between thermal pressure and magnetic pressure, might destabilise the Buneman instability and introduce an exception to the simple mathematical trapping condition. On the other hand, the values for the plasma beta of our two shocks, which are $\beta_{e,R} = 10^{-3}$ for the forward shock and $\beta = 10^{-2}$ for the reverse shock, are much lower than the range that was investigated by Matsumoto/Amano/Hoshino (2012). This might be an indication for another exception to the trapping condition at very low values for the plasma beta, which would be worthwhile to be investigated in more detail.

---

[111] Burgess/Wilkinson/Schwartz, Journal of Geophysical Research: Space Physics 94 [1989].

[112] Leroy et al., Geophysical Research Letters 8 [1981].

[113] Leroy et al., Journal of Geophysical Research: Space Physics 87 [1982].

[114] Buneman, Physical Review 115 [1959].

Using a setup with two colliding asymmetric plasma flows allowed us to study two quite different shocks. Most significantly, we observed the development of filamentary structures in the shock ramp of the high sonic Mach number forward shock, while the reverse shock with much lower sonic Mach number exhibited no noticeable filamentary structures. This result would be in agreement with the existence of a critical Mach number for quasi-perpendicular collisionless shocks that determines the development of filamentary structures in the shock ramp[115,116]. Above this Mach number, a significant fraction of the incoming ions are reflected at the shock front and thereby cause instabilities, which is what we can observe at our forward shock. However, by comparing with the results from other publications[117,118,119,120,121] we arrived at the conclusion that our results suggest that the development of filamentary structures in the shock ramp of quasi-perpendicular collisionless shocks might not necessarily be determined by the existence of a critical sonic Mach number but by a critical shock speed. More detailed investigations with a variation in shock speed and sonic Mach number could help to find a definitive answer to this effect.

Combining our results from Niemiec et al. (2012) and the current investigation, we have only studied the most extreme cases for a SNR shock, namely the unmagnetised shock, the magnetised strictly parallel shock and the magnetised strictly perpendicular shock. Future studies using the same setup could shed more light on the case of oblique shocks. Equipped with even more sophisticated computational power, it would be also possible to study collisionless shocks for more realistic physical parameters, especially the ion-to-electron mass ratio.

Nevertheless, we can say that with the current investigation we were able to make some important observations regarding our understanding of the physics at SNR shock fronts which provide us with useful evidence to eventually pin down the culprit. Although we are not able to close the case at this point, our studies might be used as an input to further investigations using more detailed PIC simulations, or also for hybrid or MHD simulations and, together with more sophisticated observational methods, will help to bring us closer to an answer as to how particles can be accelerated in SNRs and eventually become cosmic rays that can be detected on Earth.

---

[115] Bale et al., Quasi-perpendicular Shock Structure and Processes

[116] Kennel/Edmiston/Hada, A Quarter Century of Collisionless Shock Research.

[117] Amano/Hoshino, The Astrophysical Journal 690 [2009].

[118] Kato/Takabe, The Astrophysical Journal 721 [2010].

[119] Guo/Sironi/Narayan, ArXiv e-prints 2014.

[120] Riquelme/Spitkovsky, The Astrophysical Journal 733 [2011].

[121] Caprioli/Spitkovsky, The Astrophysical Journal 783 [2014].

List of Figures

Bibliography

M. G. Aartsen et al.: First Observation of PeV-Energy Neutrinos with IceCube. Physical Review Letters, 111 2013, 021103 (1–7) ⟨URL: `http://link.aps.org/doi/10.1103/PhysRevLett.111.021103`⟩

M. Ackermann et al.: Detection of the Characteristic Pion-Decay Signature in Supernova Remnants. Science, 339 2013, Nr. 6121, 807–811 ⟨URL: `http://www.sciencemag.org/content/339/6121/807.abstract`⟩

M. Ajello et al.: Fermi Large Area Telescope Observations of the Supernova Remnant G8.7-0.1. The Astrophysical Journal, 744 2012, Nr. 1, 80–91 ⟨URL: `http://stacks.iop.org/0004-637X/744/i=1/a=80`⟩

T. Amano/M. Hoshino: Electron Injection at High Mach Number Quasi-perpendicular Shocks: Surfing and Drift Acceleration. The Astrophysical Journal, 661 2007, Nr. 1, 190 ⟨URL: `http://stacks.iop.org/0004-637X/661/i=1/a=190`⟩

Takanobu Amano/Masahiro Hoshino: Electron Shock Surfing Acceleration in Multidimensions: Two-Dimensional Particle-in-Cell Simulation of Collisionless Perpendicular Shock. The Astrophysical Journal, 690 2009, Nr. 1, 244–251 ⟨URL: `http://stacks.iop.org/0004-637X/690/i=1/a=244`⟩

Takanobu Amano/Masahiro Hoshino: A Critical Mach Number for Electron Injection in Collisionless Shocks. Phys. Rev. Lett. 104 May 2010, 181102 (1–4 ⟨URL: `http://link.aps.org/doi/10.1103/PhysRevLett.104.181102`⟩

Gene Amdahl: Validity of the Single Processor Approach to Achieving Large-Scale Computing Capabilities. In AFIPS Conference Proceedings. Band 30, New York, NY, USA, 1967

W. D. Apel et al.: Kneelike Structure in the Spectrum of the Heavy Component of Cosmic Rays Observed with KASCADE-Grande. Physical Review Letters, 107 2011, 171104 (1–5) ⟨URL: `http://link.aps.org/doi/10.1103/PhysRevLett.107.171104`⟩

W. D. Apel et al.: Ankle-like feature in the energy spectrum of light elements of cosmic rays observed with KASCADE-Grande. Physical Review D, 87 2013, 081101 (1–6) ⟨URL: `http://link.aps.org/doi/10.1103/PhysRevD.87.081101`⟩

Pierre Auger et al.: Extensive Cosmic-Ray Showers. Reviews of Modern Physics, 11 1939, 288–291 ⟨URL: `http://link.aps.org/doi/10.1103/RevModPhys.11.288`⟩

W. I. Axford/E. Leer/G. Skadron: The acceleration of cosmic rays by shock waves. In International Cosmic Ray Conference. Band 11, 1977, 132–137

S.D. Bale et al.: Quasi-perpendicular Shock Structure and Processes. In **G. Paschmann et al. (Hrsg.):** Outer Magnetospheric Boundaries: Cluster Results. Band 20, Springer Netherlands, 2005 ⟨URL: `http://dx.doi.org/10.1007/1-4020-4582-4_6`⟩, ISBN 978–1–4020–3488–6, 161–203

Pablo M. Bauleo/Julio Rodriguez Martino: The dawn of the particle astronomy era in ultra-high-energy cosmic rays. Nature, 458 2009, 847–851 ⟨URL: `http://www.nature.com/nature/journal/v458/n7240/full/nature07948.html`⟩

A. R. Bell: The acceleration of cosmic rays in shock fronts – I. Monthly Notices of the Royal Astronomical Society, 182 1978a, Nr. 2, 147–156 ⟨URL: `http://mnras.oxfordjournals.org/content/182/2/147.abstract`⟩

A. R. Bell: The acceleration of cosmic rays in shock fronts – II. Monthly Notices of the Royal Astronomical Society, 182 1978b, Nr. 3, 443–455 ⟨URL: `http://mnras.oxfordjournals.org/content/182/3/443.abstract`⟩

J. Beringer et al.: Review of Particle Physics. Physical Review D, 86 2012, 010001 (1–1528) ⟨URL: `http://link.aps.org/doi/10.1103/PhysRevD.86.010001`⟩

Charles K. Birdsall/A. Bruce Langdon: Plasma physics via computer simulation. Institute of Physics Publishing, 1991

Antoine Bret/Mark E. Dieckmann: How large can the electron to proton mass ratio be in particle-in-cell simulations of unstable systems? Physics of Plasmas, 17 2010, Nr. 3, 032109 (1–8) ⟨URL: `http://link.aip.org/link/?PHP/17/032109/1`⟩

Oscar Buneman: Dissipation of Currents in Ionized Media. Physical Review, 115 1959, 503–517 ⟨URL: `http://journals.aps.org/pr/abstract/10.1103/PhysRev.115.503`⟩

Oscar Buneman; H. Matsumoto/Y. Omura (Hrsg.): Kap. TRISTAN: The 3-D Electromagnetic Particle Code In Computer Space Plasma Physics. Terra Scientific Publishing Company, 1993, 67–84

D. Burgess/M. Scholer: Shock front instability associated with reflected ions at the perpendicular shock. Physics of Plasmas, 14 2007, Nr. 1 ⟨URL: `http://scitation.aip.org/content/aip/journal/pop/14/1/10.1063/1.2435317`⟩

David Burgess/William P. Wilkinson/Steve J. Schwartz: Ion distributions and thermalization at perpendicular and quasi-perpendicular supercritical collisionless shocks. Journal of Geophysical Research: Space Physics, 94 1989, Nr. A7, 8783–8792 ⟨URL: `http://dx.doi.org/10.1029/JA094iA07p08783`⟩

D. Caprioli/A. Spitkovsky: Simulations of Ion Acceleration at Non-relativistic Shocks: I) Acceleration Efficiency. The Astrophysical Journal, 783 2014, Nr. 2, 91 ⟨URL: `http://stacks.iop.org/0004-637X/783/i=2/a=91`⟩

Richard Courant/Kurt Friedrichs/Hans Lewy: Über die partiellen Differenzengleichungen der mathematischen Physik. Mathematische Annalen, 100 1928, Nr. 1, 32–74 ⟨URL: `http://dx.doi.org/10.1007/BF01448839`⟩

Peter Alan Davidson: An Introduction to Magnetohydrodynamics. Cambridge University Press, 2001

John M. Dawson: Particle simulation of plasmas. Reviews of Modern Physics, 55 1983, 403–447 ⟨URL: `http://link.aps.org/doi/10.1103/RevModPhys.55.403`⟩

John F. Douglas et al.: Fluid Mechanics. Pearson Education, 2005

L.O. Drury/T.P. Downes: Turbulent magnetic field amplification driven by cosmic ray pressure gradients. Monthly Notices of the Royal Astronomical Society, 427 2012, 2308–2313

Enrico Fermi: On the Origin of the Cosmic Radiation. Physical Review, 75 1949, 1169–1174 ⟨URL: `http://link.aps.org/doi/10.1103/PhysRev.75.1169`⟩

Katia M. Ferrière: The interstellar environment of our galaxy. Reviews of Modern Physics, 73 2001, 1031–1066 ⟨URL: `http://link.aps.org/doi/10.1103/RevModPhys.73.1031`⟩

Phyllis Freier et al.: Evidence for Heavy Nuclei in the Primary Cosmic Radiation. Physical Review, 74 1948, 213–217 ⟨URL: `http://link.aps.org/doi/10.1103/PhysRev.74.213`⟩

A. Friedman et al.: Damped time advance methods for particles and EM fields. In US-Japan Workshop on Advances in Simulation Techniques Applied to Plasmas and Fusion. Livermore, California, USA, 1990

L. Gargaté/A. Spitkovsky: Ion Acceleration in Non-relativistic Astrophysical Shocks. The Astrophysical Journal, 744 2012, Nr. 1, 67 (1–15) ⟨URL: `http://stacks.iop.org/0004-637X/744/i=1/a=67`⟩

V. L. Ginzburg/S. I. Syrovatsky: Origin of Cosmic Rays. Progress of Theoretical Physics Supplement, 20 1961, 1–83 ⟨URL: `http://ptp.ipap.jp/link?PTPS/20/1/`⟩

F. Giordano et al.: Fermi Large Area Telescope Detection of the Young Supernova Remnant Tycho. The Astrophysical Journal Letters, 744 2012, Nr. 1, L2 (1–5) ⟨URL: `http://stacks.iop.org/2041-8205/744/i=1/a=L2`⟩

A. Giuliani et al.: Neutral Pion Emission from Accelerated Protons in the Supernova Remnant W44. The Astrophysical Journal Letters, 742 2011, Nr. 2, L30 (1–5) ⟨URL: `http://stacks.iop.org/2041-8205/742/i=2/a=L30`⟩

Andrew D. Greenwood et al.: On the elimination of numerical Cerenkov radiation in PIC simulations. Journal of Computational Physics, 201 2004, 665–684 ⟨URL: `http://dx.doi.org/10.1016/j.jcp.2004.06.021`⟩

Kenneth Greisen: End to the Cosmic-Ray Spectrum? Physical Review Letters, 16 1966, 748–750 ⟨URL: `http://link.aps.org/doi/10.1103/PhysRevLett.16.748`⟩

Yu. N. Grigoryev/V. A. Vshivkov/M. P. Fedoruk: Numerical ”Particle-in-Cell”Methods. de Gruyter, 2002

William Gropp/Ewing Lusk/Anthony Skjellum: Using MPI. Massachusetts Institute of Technology, 1999

William Gropp/Ewing Lusk/Rajeev Thakur: Using MPI-2. Massachusetts Institute of Technology, 1999

X. Guo/L. Sironi/R. Narayan: Non-Thermal Electron Acceleration in Low Mach Number Collisionless Shocks. I. Particle Energy Spectra and Acceleration Mechanism. ArXiv e-prints Juni 2014

D. A. Gurnett et al.: In Situ Observations of Interstellar Plasma with Voyager 1. Science, 341 2013, Nr. 6153, 1489–1492 ⟨URL: `http://www.sciencemag.org/content/341/6153/1489.abstract`⟩

Victor Francis Hess: Über Beobachtungen der durchdringenden Strahlung bei sieben Freiballonfahrten. Physikalische Zeitschrift, 13 1912, 1084–1091

A. M. Hillas: The Origin of Ultra-High-Energy Cosmic Rays. Annual Review of Astronomy and Astrophysics, 22 1984, 425–444 ⟨URL: `http://adsabs.harvard.edu/abs/1984ARA%26A..22..425H`⟩

Roger W. Hockney/James W. Eastwood: Computer simulation using particles. Institute of Physics Publishing, 1988

Masahiro Hoshino: Nonthermal Particle Acceleration in Shock Front Region: Shock Surfing Accelerations. Progress of Theoretical Physics Supplement, 143 2001, 149–181 ⟨URL: `http://ptp.ipap.jp/link?PTPS/143/149/`⟩

Pierre Henri Hugoniot: Mémoire sur la propagation des mouvements dans les corps et spécialement dans les gaz parfaits (première partie). Journal de l'École Polytechnique, 57 1887, 3–97

Pierre Henri Hugoniot: Mémoire sur la propagation des mouvements dans les corps et spécialement dans les gaz parfaits (deuxième partie). Journal de l'École Polytechnique, 58 1889, 1–125

Jörg R. Hörandel: Cosmic rays at the highest energies. Progress in Particle and Nuclear Physics, 64 2010, Nr. 2, 351–359 ⟨URL: `http://www.sciencedirect.com/science/article/pii/S0146641009001252`⟩

Tsunehiko N. Kato/Hideaki Takabe: Nonrelativistic Collisionless Shocks in Weakly Magnetized Electron-Ion Plasmas: Two-dimensional Particle-in-cell Simulation of Perpendicular Shock. The Astrophysical Journal, 721 2010, Nr. 1, 828 ⟨URL: `http://stacks.iop.org/0004-637X/721/i=1/a=828`⟩

C. F. Kennel/J. P. Edmiston/T. Hada: A Quarter Century of Collisionless Shock Research. American Geophysical Union, 2013 ⟨URL: `http://dx.doi.org/10.1029/GM034p0001`⟩, 1–36, ISBN 9781118664032

D. Krauss-Varban/C.S. Wu: Fast Fermi and gradient drift acceleration of electrons at nearly perpendicular collisionless shocks. Journal of Geophysical Research, 94 1989, 15367–15372

S. M. Krimigis et al.: Imaging the Interaction of the Heliosphere with the Interstellar Medium from Saturn with Cassini. Science, 326 2009, Nr. 5955, 971–973 ⟨URL: `http://www.sciencemag.org/content/326/5955/971.abstract`⟩

Marc M. Leroy et al.: Simulation of a perpendicular bow shock. Geophysical Research Letters, 8 1981, Nr. 12, 1269–1272 ⟨URL: `http://dx.doi.org/10.1029/GL008i012p01269`⟩

Marc M. Leroy et al.: The structure of perpendicular bow shocks. Journal of Geophysical Research: Space Physics, 87 1982, Nr. A7, 5081–5094 ⟨URL: `http://dx.doi.org/10.1029/JA087iA07p05081`⟩

G. Livadiotis/D.J. McComas: Understanding Kappa Distributions: A Toolbox for Space Science and Astrophysics. Space Science Reviews, 175 2013, Nr. 1-4, 183–214 ⟨URL: `http://dx.doi.org/10.1007/s11214-013-9982-9`⟩, ISSN 0038–6308

Ernst Mach/Joachim Thiele: Arbeiten über Erscheinungen an fliegenden Projektilen. Joachim Thiele, 1887

Yosuke Matsumoto/Takanobu Amano/Masahiro Hoshino: Electron Accelerations at High Mach Number Shocks: Two-dimensional Particle-in-cell Simulations in Various Parameter Regimes. The Astrophysical Journal, 755 2012, Nr. 2, 109 ⟨URL: `http://stacks.iop.org/0004-637X/755/i=2/a=109`⟩

G. C. Murphy et al.: Magnetic field amplification and electron acceleration to near-energy equipartition with ions by a mildly relativistic quasi-parallel plasma protoshock. Astronomy & Astrophysics, 524 2010, A84 (1–12) ⟨URL: `http://dx.doi.org/10.1051/0004-6361/201015294`⟩

G. C. Murphy/M. E. Dieckmann/L. O´ C. Drury: Magnetic vortex growth in the transition layer of a mildly relativistic plasma shock. Physics of Plasmas, 17 2010, Nr. 11 ⟨URL: `http://scitation.aip.org/content/aip/journal/pop/17/11/10.1063/1.3493627`⟩

Jacek Niemiec et al.: Aperiodic Magnetic Turbulence Produced by Relativistic Ion Beams. The Astrophysical Journal, 709 2010, Nr. 2, 1148–1156 ⟨URL: `http://stacks.iop.org/0004-637X/709/i=2/a=1148`⟩

Jacek Niemiec et al.: Nonrelativistic Parallel Shocks in Unmagnetized and Weakly Magnetized Plasmas. The Astrophysical Journal, 759 2012, Nr. 1, 73–93 ⟨URL: `http://stacks.iop.org/0004-637X/759/i=1/a=73`⟩

Jacek Niemiec et al.: Production of Magnetic Turbulence by Cosmic Rays Drifting Upstream of Supernova Remnant Shocks. The Astrophysical Journal, 684 2008, Nr. 2, 1174–1189 ⟨URL: `http://stacks.iop.org/0004-637X/684/i=2/a=1174`⟩

V. Pierrard/M. Lazar: Kappa Distributions: Theory and Applications in Space Plasmas. Solar Physics, 267 2010, Nr. 1, 153–174 ⟨URL: `http://dx.doi.org/10.1007/s11207-010-9640-2`⟩, ISSN 0038–0938

W. J. Macquorn Rankine: On the Thermodynamic Theory of Waves of Finite Longitudinal Disturbance. Philosophical Transactions of the Royal Society of London, 160 1870, 277–288 ⟨URL: `http://rstl.royalsocietypublishing.org/content/160/277.short`⟩

Stephen P. Reynolds: Supernova Remnants at High Energy. Annual Review of Astronomy and Astrophysics, 46 2008, Nr. 1, 89–126 ⟨URL: `http://www.annualreviews.org/doi/abs/10.1146/annurev.astro.46.060407.145237`⟩

Stephen P. Reynolds et al.: The Youngest Galactic Supernova Remnant: G1.9+0.3. The Astrophysical Journal Letters, 680 2008, Nr. 1, L41–L44 ⟨URL: `http://stacks.iop.org/1538-4357/680/i=1/a=L41`⟩

Estela M. Reynoso/John P. Hughes/David A. Moffett: On the Radio Polarization Signature of Efficient and Inefficient Particle Acceleration in Supernova Remnant SN 1006. The Astronomical Journal, 145 2013, Nr. 4, 104 ⟨URL: `http://stacks.iop.org/1538-3881/145/i=4/a=104`⟩

Mario A. Riquelme/Anatoly Spitkovsky: Electron Injection by Whistler Waves in Non-relativistic Shocks. The Astrophysical Journal, 733 2011, Nr. 1, 63 (1–15 ⟨URL: `http://stacks.iop.org/0004-637X/733/i=1/a=63`⟩

R.Z. Sagdeev/V.D. Shapiro: Influence of Transverse Magnetic Field on Landau Damping. Letters to Jounal of Experimental and Theoretical Physics, 17 1973, Nr. 7, 279–282 ⟨URL: `http://www.jetpletters.ac.ru/ps/1541/article_23576.shtml`⟩

Kevin Schawinski et al.: Supernova Shock Breakout from a Red Supergiant. Science, 321 2008, Nr. 5886, 223–226 ⟨URL: `http://www.sciencemag.org/content/321/5886/223.abstract`⟩

M. Scholer/S. Matsukiyo: Nonstationarity of quasi-perpendicular shocks: a comparison of full particle simulations with different ion to electron mass ratio. Annales Geophysicae, 22 2004, 2345–2353

Nobue Shimada/Masahiro Hoshino: Effect of strong thermalization on shock dynamical behavior. Journal of Geophysical Research: Space Physics, 110 2005, Nr. A2, n/a–n/a ⟨URL: `http://dx.doi.org/10.1029/2004JA010596`⟩, ISSN 2156–2202

Stephen J. Smartt: Progenitors of Core-Collapse Supernovae. Annual Review of Astronomy and Astrophysics, 47 2009, Nr. 1, 63–106 ⟨URL: `http://www.annualreviews.org/doi/abs/10.1146/annurev-astro-082708-101737`⟩

Thomas Stroman/Martin Pohl/Jacek Niemiec: Kinetic Simulations of Turbulent Magnetic-Field Growth by Streaming Cosmic Rays. The Astrophysical Journal, 706 2009, Nr. 1, 38–44 ⟨URL: `http://stacks.iop.org/0004-637X/706/i=1/a=38`⟩

Thomas Stroman et al.: Could Cosmic Rays Affect Instabilities in the Transition Layer of Non-relativistic Collisionless Shocks? The Astrophysical Journal, 746 2012, Nr. 1, 24–34 ⟨URL: `http://stacks.iop.org/0004-637X/746/i=1/a=24`⟩

Thomas Alan Stroman: Particle-in-cell simulation of astrophysical plasmas: probing the origin of cosmic rays. Dissertation, Iowa State University, 2010

W. Stroman/M. Pohl: Radio Polarimetry Signatures of Strong Magnetic Turbulence in Supernova Remnants. The Astrophysical Journal, 696 2009, 1864–1870

The Pierre Auger Collaboration: Correlation of the Highest-Energy Cosmic Rays with Nearby Extragalactic Objects. Science, 318 2007, Nr. 5852, 938–943 ⟨URL: `http://www.sciencemag.org/content/318/5852/938.abstract`⟩

R. A. Treumann/C. H. Jaroschek: Fundamentals of Non-relativistic Collisionless Shock Physics: I. The Shock Problem. 2008a ⟨URL: `http://de.arxiv.org/abs/0805.2132`⟩

R. A. Treumann/C. H. Jaroschek: Fundamentals of Non-relativistic Collisionless Shock Physics: II. Basic Equations and Models. 2008b ⟨URL: `http://de.arxiv.org/abs/0805.2162`⟩

Takayuki Umeda: Study on Nonlinear Processes of Electron Beam Instabilities via Computer Simulations. Dissertation, Graduate School of Informatics Kyoto, 2004

Takayuki Umeda et al.: A new charge conservation method in electromagnetic particle-in-cell simulations. Computer Physics Communications, 156 2003, 73–85 ⟨URL: `http://www.sciencedirect.com/science/article/pii/S0010465503004375`⟩

Takayuki Umeda/Masahiro Yamao/Ryo Yamazaki: Two-dimensional Full Particle Simulation of a Perpendicular Collisionless Shock with a Shock-Rest-Frame Model. The Astrophysical Journal Letters, 681 2008, Nr. 2, L85–L88 ⟨URL: `http://stacks.iop.org/1538-4357/681/i=2/a=L85`⟩

Takayuki Umeda/Masahiro Yamao/Ryo Yamazaki: Electron Acceleration at a Low Mach Number Perpendicular Collisionless Shock. The Astrophysical Journal, 695 2009, Nr. 1, 574–579 ⟨URL: `http://stacks.iop.org/0004-637X/695/i=1/a=574`⟩

Jean-Luc Vay: Simulation of beams or plasmas crossing at relativistic velocity. Physics of Plasmas, 15 2008, 056701 (1–6) ⟨URL: `http://link.aip.org/link/doi/10.1063/1.2837054`⟩

Andrey E. Vladimirov/Andrei M. Bykov/Donald C. Ellison: Turbulence Dissipation and Particle Injection in Nonlinear Diffusive Shock Acceleration with Magnetic Field Amplification. The Astrophysical Journal, 688 2008, Nr. 2, 1084–1101 ⟨URL: `http://stacks.iop.org/0004-637X/688/i=2/a=1084`⟩

Anatoly Vlasov: The Vibrational Properties of an Electron Gas. Soviet Physics Uspekhi, 10 1968, Nr. 6, 721–733 ⟨URL: `http://stacks.iop.org/0038-5670/10/i=6/a=R01`⟩

F.L. Waelbroeck: Theory and observations of magnetic islands. Nuclear Fusion, 49 2009, Nr. 10, 104025 ⟨URL: `http://stacks.iop.org/0029-5515/49/i=10/a=104025`⟩

W. R. Webber: A New Estimate of the Local Interstellar Energy Density and Ionization Rate of Galactic Cosmic Cosmic Rays. The Astrophysical Journal, 506 1998, Nr. 1, 329–334 ⟨URL: `http://stacks.iop.org/0004-637X/506/i=1/a=329`⟩

Volkmar Wieland et al.: Non-relativistic Perpendicular Shocks in Weakly Magnetized Plasmas. 2014

C.S. Wu et al.: Microinstabilities associated with a high Mach number, perpendicular bow shock. Space Science Reviews, 37 1984, Nr. 1-2, 63–109 ⟨URL: `http://dx.doi.org/10.1007/BF00213958`⟩, ISSN 0038–6308

Kane S. Yee: Numerical solution of initial boundary value problems involving Maxwell's equations in isotropic media. IEEE Transactions on antennas and propagation, 14 1966, 302–307 ⟨URL: `http://dx.doi.org/10.1109/TAP.1966.1138693`⟩

Georgiy T. Zatsepin/Vadim A. Kuz'min: Upper Limit of the Spectrum of Cosmic Rays. Soviet Journal of Experimental and Theoretical Physics Letters, 4 1966, 78–80 ⟨URL: `http://adsabs.harvard.edu/abs/1966JETPL...4...78Z`⟩

Acknowledgements

First of all, I want to thank my supervisor Martin Pohl for giving me the opportunity to discover the very exciting field of astroparticle physics. I learned that there is much more out there in the Universe than what we can see with our eyes and that what we cannot see is as fascinating as that what we can see. I also want to thank him for all fruitful discussions and the support I received for my project and for the creation of the present work.

I also want to thank all of my colleagues and friends who accompanied me on my journey through the last years. Thanks be to Jens Ruppel who did an invaluable service in being my mentor for my first year as a PhD student and who prepared the first version of the new setup for the perpendicular shock. Thanks be to Robert Rettig and Iman Rafighi with whom I shared our modest office in the Golden Cage in Golm and with whom I became good friends. Thanks be also to Nils Håkansson and Xuhui Chen for their support and their friendship.

This work would not have been possible without the support of collaborators on site and abroad. I want to thank Jacek Niemiec for his dedicated work on the THISMPI code, all accompanying post-processing tools he was able to provide me with and for our productive dialogue to make this work as good as possible. I want to thank Ken-Ichi Nishikawa for granting me access through his project to the high-performance computer resources of the Texas Advanced Computing Center on which most of the presented simulation was accomplished. I also want to thank Achim Feldmeier for all the years we had together with interesting lectures and for evaluating yet another of my theses. The same thanks goes to Reinhard Schlickeiser for giving his time to evaluate my dissertation.

I want to thank all my friends who accompanied me through my ten years of my study of physics in Potsdam. Thanks be to Andreas Sander for long hours in exercises and for long years of friendship. Thanks be to Sebastian Kamann for providing the original layout for the present thesis. Thanks be also to Tobias Diekershoff for reading it.

I would not have arrived at this point without lots of inspiration from some very important people in my life. A big thanks be to my physics teacher in high school, Friedrich-Wilhelm Heins, who opened the path into the world of physics for me. Thanks be also to Stephen Hawking for his inspiring book "A Brief History of Time". Finally, a deep bow before the Great Bird of the Galaxy, Gene Roddenberry, who gave me my biggest inspiration to study physics by his creation "Star Trek".

Of course, I also do not want to forget to thank all the diligent people who developed the free software with which this enterprise was made possible: Linux, LaTeX, TeXmaker, GIMP, LibreOffice, gnuplot, Maxima and Google.

I want to give a big thanks to my parents, Sonja and Jörg Wießner, for their moral and financial support and who were always there for me. I also want to thank my parents-in-law, Kerstin and Ralf Wieland, and my sister-in-law, Reina Wieland, for all their advice and technical support.

Finally, I want give thanks to the most important person in my life: my wonderful wife, Nelly Wieland. I would not be the same person without her. Especially, I want to thank her for giving me counsel and strength, for believing in me and supporting me in everything. Most of all I want to thank her for what we share: our unwavering faith and our love.

Selbstständigkeitserklärung

Hiermit erkläre ich, dass ich die vorliegende Dissertation mit dem Titel

Particle-in-Cell Simulations of Perpendicular Supernova Shock Fronts

selbstständig verfasst habe.

Alle verwendeten Quellen und Hilfsmittel habe ich angegeben. Alle Stellen, die wörtlich oder sinngemäß anderen Werken entnommen sind, sind als solche gekennzeichnet.

Potsdam, den 16. März 2015

Volkmar Wieland